

On the Origin of Quenched but Gas-rich Regions at Kiloparsec Scales in Nearby Galaxies

TAO JING ¹ AND CHENG LI ¹

¹*Department of Astronomy, Tsinghua University, Beijing 100084, China*

ABSTRACT

We use resolved spectroscopy from MaNGA to investigate the significance of both local and global properties of galaxies to the cessation of star formation at kpc scales. Quenched regions are identified from a sample of isolated disk galaxies by a single-parameter criterion $D_n(4000) - \log \text{EW}(\text{H}\alpha) > 1.6 - \log 2 = 1.3$, and are divided into gas-rich quenched regions (GRQRs) and gas-poor quenched regions (GPQRs) according to the surface density of cold gas (Σ_{gas}). Both types of quenched regions tend to be hosted by non-AGN galaxies with relatively high mass ($M_* \gtrsim 10^{10} M_\odot$) and red colors ($\text{NUV} - r \gtrsim 3$), as well as low star formation rate and high central density at fixed mass. They span wide ranges in other properties including structural parameters that are similar to the parent sample, indicating that the conditions responsible for quenching in gas-rich regions are largely independent on the global properties of galaxies. We train random forest (RF) classifiers and regressors for predicting quenching in our sample with 15 local/global properties. Σ_* is the most important property for quenching, especially for GRQRs. These results strongly indicate the important roles of low-mass hot evolved stars which are numerous and long-lived in quenched regions and can provide substantial radiation pressure to support the surrounding gas against gravitational collapse. The different feature importance for quenching as found previously by Bluck et al. (2020a,b) are partly due to the different definitions of quenched regions, particularly the different requirements on $\text{EW}(\text{H}\alpha)$.

Keywords: galaxy, quenching, feedback

1. INTRODUCTION

Observations of galaxy populations at different redshifts have well established that the fraction of red quiescent galaxies has significantly increased since a redshift of unity (e.g. Bell et al. 2004; Bundy et al. 2006; Faber et al. 2007), implying that the cessation of star formation has been a driving process in galaxy evolution over the past ~ 8 Gyr. However, how galaxies quench their star formation remains an unresolved problem, despite decades of studies which have proposed a variety of quenching mechanisms. In most cases, star formation ceases in a galaxy through removal or heating of cold gas as a result of processes external or internal to the galaxy. External processes include shock heating of gas in massive dark matter halos (e.g. Rees & Ostriker 1977; Silk 1977; Blumenthal et al. 1984; Birnboim & Dekel 2003; Kereš et al. 2005; Cattaneo et al. 2006; Dekel & Birnboim 2006; Birnboim et al. 2007; Cattaneo et al. 2008;

Ocvirk et al. 2008), stripping of hot and even cold gas by ram pressure, tidal interactions, and strangulation (e.g. Gunn & Gott 1972; Toomre & Toomre 1972; Moore et al. 1996; Abadi et al. 1999; Balogh et al. 2000; Vogt et al. 2004; Chung et al. 2009; Weinmann et al. 2009; Li et al. 2012; Merluzzi et al. 2013; Zhang et al. 2013; Bekki 2014; Davis et al. 2015; Peng et al. 2015; Davies et al. 2019; Poggianti et al. 2017; Sazonova et al. 2021), and major mergers of gas-rich galaxies which induce fast conversion of cold gas to stars at galactic center as well as the so-called “quasar-mode” active galactic nucleus (AGN) feedback (e.g. Barnes & Hernquist 1991; Mihos & Hernquist 1996; Di Matteo et al. 2005; Springel et al. 2005; Hopkins et al. 2006, 2009; Fabian 2012). Internal to a galaxy, the processes proposed for quenching include stellar feedback driven by radiation pressure, stellar wind and supernova explosions (e.g. Cox & Smith 1974; McKee & Ostriker 1977; McCray & Snow 1979; Whitworth 1979; Dekel & Silk 1986; Binette et al. 1994; Ceverino & Klypin 2009; Conroy et al. 2015; Muratov et al. 2015; Raskutti et al. 2016; Herpich et al. 2018; Hopkins et al. 2018a,b; Li et al. 2020a; Ostriker & Kim 2022), the “radio-mode” AGN feedback from accretion of hot halo gas onto the central supermassive black hole in massive central galaxies (e.g. Bower et al. 2006; Cro-

Corresponding author: Tao Jing
jingt20@mails.tsinghua.edu.cn

Corresponding author: Cheng Li
cli2015@tsinghua.edu.cn

ton et al. 2006; Bower et al. 2008; Fabian 2012), and “compaction quenching” which explains the formation of compact quenched red nuggets at high redshift by accretion-driven violent instability of gas-rich discs (e.g. Dekel & Burkert 2014; Zolotov et al. 2015).

Observations have also clearly established that the majority of quenched galaxies at the center of galaxy groups/clusters and at both low and high redshifts have a massive dense structure at the galactic center such as a prominent bulge (e.g. Bell 2008; Bundy et al. 2010; Masters et al. 2010; Cheung et al. 2012; Fang et al. 2013; Bluck et al. 2014; Barro et al. 2017). In addition, a significant population of red-sequence galaxies at both low and high redshifts have been observed to present disk-dominated spirals with large bulges in the center (e.g. Wolf et al. 2005, 2009; Bamford et al. 2009; Bundy et al. 2010; Masters et al. 2010; Hao et al. 2019; Guo et al. 2020; Cui et al. 2024). These findings support the scenario of “morphological quenching” as originally proposed by Martig et al. (2009). In this picture, a massive bulge, or more generally a centrally-concentrated mass distribution may effectively stabilize the gas disk, thus suppressing or even quenching the star formation by sheared perturbations within the disk. As a natural prediction of this process, the galaxy may sustain a large amount of cold gas in the disk even when the star formation is totally quenched. Indeed, high detection rates of HI emission have been reported in massive red spirals (e.g. Guo et al. 2020; Wang et al. 2022) and early-type galaxies (e.g. Serra et al. 2012). As pointed out by Zhou et al. (2021), however, many of the massive red spirals as selected by the optical color index $u - r$ in previous studies are actually green or even blue in the NUV-to-optical color NUV $- r$. In a recent study, Li et al. (2023) identified a sample of 47 quenched HI-rich galaxies that are truly red with NUV $- r > 5$ and have unusually large amounts of total HI mass. The authors found no evidence for morphological quenching, however, by comparing the structural properties of the red HI-rich galaxies with control samples of HI-normal galaxies. In addition, by comparing the red HI-rich galaxies with a complete sample selected from the Sloan Digital Sky Survey (York et al. 2000) as well as previous samples of HI-rich galaxies with low or suppressed star formation (Serra et al. 2012; Lemonias et al. 2014; Parkash et al. 2019; Sharma et al. 2023), the authors concluded that quenched HI-rich galaxies constitute only a tiny fraction of the general population of massive quiescent galaxies in the local Universe. This result is consistent with the widely-accepted fact that the cessation of star formation in a galaxy must be associated with the reduction of its cold gas reservoir (see Saintonge & Catinella 2022, for a recent review and references therein).

Motivated by the observed relationship between the local surface density of star formation rate (SFR), Σ_{SFR} and the local surface density of molecular gas Σ_{H_2} down from kpc to sub-kpc scales (e.g. Bigiel et al. 2008;

Schruba et al. 2011; Leroy et al. 2013; Lin et al. 2019a; Ellison et al. 2021a), several physical models have assumed star formation to be regulated by the molecular fraction of the ISM, which is governed by its local conditions such as hydrostatic mid-plane pressure or dynamical equilibrium pressure (e.g. Elmegreen 1989; Elmegreen & Parravano 1994; Wong & Blitz 2002; Blitz & Rosolowsky 2004, 2006; McKee & Ostriker 2007; Ostriker et al. 2010; Ostriker & Kim 2022; Ellison et al. 2024), or the combination of local gas density and metallicity (e.g. Schaye 2004; Krumholz et al. 2009; Krumholz 2012). For rotationally supported disks, large-scale gravitational instabilities on scales larger than the ISM scale height have been assumed to play a major role in regulating star formation (e.g. Safronov 1960; Toomre 1964; Goldreich & Lynden-Bell 1965; Jog & Solomon 1984; Romeo 1992; Wang & Silk 1994; Hunter et al. 1998; Tan 2000; Rafikov 2001; Elmegreen 2002; McKee & Ostriker 2007; Elmegreen 2011). In such models, the potential for gas clouds to collapse and form stars is set by processes that maintain a minimum effective velocity dispersion in the ISM, thus keeping the Toomre (1964) parameter $Q \equiv \kappa c_s / (\pi G \Sigma_{\text{gas}})$ close to unity (where κ is epicyclic frequency, c_s is sound speed, and Σ_{gas} is the large-scale surface density of gas). Whether star formation is driven by local conditions of the ISM or large-scale gravitational instabilities of the disk, its cessation process (quenching) must be somehow related to one of the two types of mechanisms, or both. In addition, environmental effects external to the host galaxy should also be taken into account, as discussed above.

Previous studies of galaxy quenching have been mostly limited to single-fiber spectroscopy or multiband photometry, thus probing either a limited region at galactic centers or the global properties of the whole galaxy. In order to have a complete picture of star formation cessation in galaxies, it is necessary to have resolved spectroscopy down to scales of molecular clouds which are believed to be the sites of star formation. Integral-field unit (IFU) surveys (Bacon et al. 2001; de Zeeuw et al. 2002; Bershady et al. 2010; Cappellari et al. 2011; Croom et al. 2012; Sánchez et al. 2012; Blanc et al. 2013; Brodie et al. 2014; Ma et al. 2014; Bryant et al. 2015; Bundy et al. 2015) have provided resolved spectroscopy for star formation and quenching to be studied in large samples of galaxies down to kpc scales, though still much larger than the scales of individual star-forming regions and gas clouds (typically a few $\times 10$ pc). Generally, quenched regions are identified as having no H α emission, thus with substantially low surface brightness ($\Sigma_{\text{H}\alpha}$) or equivalent width (EW(H α)) in the H α emission line. It is common to additionally require the quenched regions to not have experienced recent star formation over the past $\sim 10^9$ yr, thus dominated by old stellar populations. This requirement is formulated usually as $D_n(4000) \gtrsim 1.6$, where $D_n(4000)$ is the depth of the break at 4000Å in the observed spectrum as defined by Balogh

et al. (1999), known as a sensitive indicator of the average stellar age (Kauffmann et al. 2003; Brinchmann et al. 2004). Moreover, it has been increasingly suggested that quenched regions can be identified out of the low ionization (nuclear) emission line regions, or LI(N)ERs on the Baldwin et al. (1981, BPT) diagnostic diagrams, which can be regarded as regions where the star formation has already ceased, and the ionization is primarily powered by hot evolved stars (e.g. Binette et al. 1994; Stasińska et al. 2008; Sarzi et al. 2010; Yan & Blanton 2012; Papaderos et al. 2013; Singh et al. 2013; Belfiore et al. 2016; Gomes et al. 2016; Belfiore et al. 2017; Zhang et al. 2017).

In practice, previous studies have usually adopted two of the three selection criteria to define quenched regions, but with different pairwise combinations. For instance, based on the Mapping Nearby Galaxies at Apache Point Observatory (MaNGA Bundy et al. 2015) survey, Li et al. (2015) and Wang et al. (2018, hereafter Paper I) identified quenched spaxels jointly by $EW(H\alpha) < 2\text{\AA}$ and $D_n(4000) > 1.6$, while Lin et al. (2019b) selected LI(N)ERs with low $H\alpha$ emission ($EW(H\alpha) < 3\text{\AA}$). Also based on MaNGA data but differently from both of the above studies, Bluck et al. (2020a,b) firstly estimated SFR surface densities (Σ_{SFR}) for both star-forming (SF) regions and non-SF regions (AGN, composite and low-S/N SF regions) as classified on the BPT diagram, using empirical relations of Σ_{SFR} with $\Sigma_{H\alpha}$ and $D_n(4000)$ respectively, and then selected quenched regions as those spaxels falling significantly below the ridge line of the resolved SF main sequence. As shown by the authors, the quenched regions so defined are essentially the non-SF regions on the BPT diagram with $D_n(4000) > 1.45$. Scientifically, Paper I found that massive galaxies with stellar mass $M_* \gtrsim 10^{10} M_\odot$ quench their star formation from inside out. Lin et al. (2019b) further found that the fraction of galaxies showing “inside-out” quenching increases with dark matter halo mass, and their results suggested that morphological quenching may be responsible for the inside-out quenching in galaxies of all environments. Bluck et al. (2020a,b) trained a multilayered artificial neural network (ANN) and a random forest (RF) to classify spaxels into SF and quenched regions given various local/global parameters, finding central velocity dispersion is the best single parameter in predicting quenching in central galaxies. This finding was interpreted by the authors as the observational evidence for AGN feedback.

In this work, we will adopt the same quenching definition as in Paper I and examine the significance of global and resolved properties to quenching in a similar way to Bluck et al. (2020a,b). In particular, we will make comparisons for subsamples of gas-rich quenched regions (GRQRs) and gas-poor quenched regions (GPQRs) selected by the surface density of cold gas (Σ_{gas}). We will also perform this analysis but adopting the same quenching definitions as in both Lin et al. (2019b) and

Bluck et al. (2020a,b), in order to examine the possible dependence of our results on quenching definition. As we will show, quenched regions selected by different criteria indeed present different correlations with global and local properties, which lead to different implications and interpretations on the underlying quenching mechanisms. The dependence on quenching definition has been largely overlooked in previous studies, and needs to be taken into account in future studies.

This paper is organized as follows. In section 2 we describe the data and parameter measurements used in this work. We then present our results in section 3. We discuss our results in section 4 and summarize in section 5. Throughout this paper we assume a flat Λ CDM cosmology with parameters given by the WMAP nine-year results: $\Omega_m = 0.286$, $\Omega_\Lambda = 0.714$ and $H_0 = 69.3 \text{ km s}^{-1} \text{ Mpc}^{-1}$ (Hinshaw et al. 2013).

2. DATA AND MEASUREMENTS

2.1. MaNGA

MaNGA is one of the three core programs of the fourth-generation Sloan Digital Sky Survey (SDSS-IV; Blanton et al. 2017), and is the largest integral field spectroscopy (IFS) survey ever accomplished (Bundy et al. 2015). During its 6-year operation from July 2014 through August 2020, MaNGA obtained IFS data for $\sim 10,000$ galaxies in the nearby Universe. MaNGA utilized 29 integral field units (IFUs), including 17 hexagonal science IFUs with a field of view (FoV) ranging from $12''$ to $32''$ and 12 seven-fiber mini-IFUs for flux calibration (Drory et al. 2015). The IFU fibers are fed to the two dual-channel BOSS spectrographs (Smee et al. 2013) on the Sloan 2.5-m telescope at the Apache Point Observatory (Gunn et al. 2006) to produce MaNGA spectra with a spectral resolution of $R \sim 2000$ over the wavelength range from 3600\AA to 10300\AA . The spectra reach an r -band signal-to-noise ratio (SNR) of 4-8 per \AA per $2''$ fiber at 1-2 effective radius (R_e) of the target galaxies, with a typical exposure time of three hours.

The targets of MaNGA are selected from the NASA Sloan Atlas (NSA; Blanton et al. 2011), and are divided into three samples: Primary, Secondary and Color-Enhanced samples. By selection the Primary and Secondary samples have a flat distribution of K -corrected i -band absolute magnitude M_i , and the targets of the two samples are observed with IFUs covering out to $1.5R_e$ and $2.5R_e$ respectively. The Color Enhanced sample further selects galaxies on the $NUV - r$ versus M_i diagram that are not well sampled by the Primary/Secondary samples. Overall, MaNGA samples span a wide stellar mass range of $5 \times 10^8 M_\odot h^{-2} \leq M_* \leq 3 \times 10^{11} M_\odot h^{-2}$ and a redshift range of $0.01 < z < 0.15$ with a median redshift of $z \sim 0.03$ (Wake et al. 2017).

The raw data of MaNGA are reduced with the Data Reduction Pipeline (DRP; Law et al. 2016) to produce a datacube for each target, with a spaxel size of $0''.5 \times 0''.5$ and an effective spatial resolution that can be

described by a Gaussian with a full width at half maximum (FWHM) of $\sim 2''.5$. The absolute flux calibration of the spectra is better than 5% for more than 80% of the wavelength range. More details about the flux calibration, survey execution strategy and data quality tests can be found in Yan et al. (2016a) and Yan et al. (2016b). In addition, by performing full spectral fitting to the datacubes from DRP, the Data Analysis Pipeline (DAP; Westfall et al. 2019; Belfiore et al. 2019) derives measurements of stellar kinematics, emission lines and spectral indices from each spectrum. All the MaNGA data including the DRP and DAP products of the full sample of 10,010 galaxies are released as a part of the final data release of SDSS-IV (DR17; Abdurro'uf et al. 2022).

2.2. Ancillary data and spaxel measurements

In addition to MaNGA data, we use ancillary data from a number of previous studies: (1) galaxy morphology type T-type from Domínguez Sánchez et al. (2018), (2) galaxy photometric parameters such as bulge-to-total ratio B/T and bulge effective radius $R_{e,\text{bulge}}$ from Meert et al. (2016), (3) position angle (PA) and axis ratio of galaxy image from NSA, and (4) galaxy interaction/merger identification from Pan et al. (2018). The last one is available only for an earlier sample of MaNGA, the MaNGA Product Launch 6 (MPL6), which includes 4690 galaxies, a random subset of the final MaNGA sample. Therefore, we restrict ourselves to MPL6 and select our sample out of it. As the first step, we exclude 1343 galaxies that are not included, or are flagged in any of the abovementioned catalogs. Next, we remove 806 interacting/merging galaxies, which are flagged $\text{flag_pair} > 0$ or $\text{p_merger} > 0.4$ by Pan et al. (2018), as well as 850 elliptical galaxies with T-type < 0 or $B/T = 1$. Finally, four galaxies flagged in the MaNGA datacube are also discarded. These restrictions result in a sample of 1687 galaxies. We call this sample as “starting sample”.

We make use of a variety of parameters for each spaxel in our galaxies, which were measured and used in our previous studies, and are made publicly available in Li & Li (2023). Here we briefly describe how the parameters were measured and refer the reader to Li & Li (2023) for more details. First of all, for kinematics, we use the MaNGA DAP products, including stellar velocity (v_*) and velocity dispersion (σ_*), gas velocity and velocity dispersion as measured from different emission lines, and flux of the emission lines. For each spaxel, we then estimate the gas-phase color excess $E(B - V)$ from Balmer decrement, with which we correct the effect of dust extinction on the emission line fluxes. We then estimate the surface density of star formation rate (SFR) Σ_{SFR} from $\Sigma_{\text{H}\alpha}$ (the extinction-corrected $\text{H}\alpha$ surface brightness), according to the estimator from Kennicutt (1998a) with projection effect corrected. The method is principally valid for regions predominantly ionized by

newly formed OB stars, which represent the majority of our sample. However, in regions where other ionization sources cannot be ignored, especially the quenched regions we will select in the next section, the Σ_{SFR} derived using this method can only be considered as an upper limit.

Next, for a given spaxel, we apply the technique of Li et al. (2020b) to the observed MaNGA spectrum to estimate a model-independent attenuation curve, and we correct the effect of stellar motions and dust attenuation for the spectrum using v_* , σ_* and the attenuation curve. We then measure stellar population parameters, e.g. stellar surface mass density Σ_* , as well as spectral indices, e.g. $\text{H}\alpha$ equivalent width $\text{EW}(\text{H}\alpha)$ and the 4000Å break $D_n(4000)$, by performing full spectral fitting to the dust-free spectrum with zero velocity broadening. Details of the technique of measuring dust attenuation curves and full spectral fitting can be found in Li et al. (2020b, 2021).

In addition, we have estimated the surface density of both molecular gas Σ_{H_2} and Hydrogen atomic gas Σ_{HI} for each spaxel. We briefly describe the two parameters and refer the reader to Appendix B for details. For Σ_{H_2} , due to the lack of spatially resolved CO observations with resolution comparable to MaNGA, we have developed an empirical estimator which uses a combination of four parameters from MaNGA to predict the fraction of molecular gas mass density $f_{\text{H}_2} \equiv \Sigma_{\text{H}_2}/(\Sigma_* + \Sigma_{\text{H}_2})$ for each spaxel. We calibrate and test the estimator using the EDGE-CALIFA survey which provides both IFS and CO mapping for a sample of nearby galaxies. We show that the estimator provides unbiased estimation of Σ_{H_2} with a reasonably small scatter of 0.26 dex (Appendix B). Similarly, Σ_{HI} is also estimated empirically for the lack of spatially resolved HI observations. We have considered three different methods, finding similar Σ_{HI} measurements. More importantly, no matter what method is adopted, Σ_{HI} contributes only a small fraction to the total gas mass density which is dominated by Σ_{H_2} in most cases. Therefore, for simplicity we assume a constant HI surface mass density for all the spaxels, $\Sigma_{\text{HI}} = 6 \times 10^6 \text{M}_\odot \text{kpc}^{-2}$, following Barrera-Ballesteros et al. (2020) (Appendix B).

2.3. Selection of spaxels

Based on the spaxel measurements, we select a sample of spaxels for the following analysis. First, we require the selected spaxels to have $\text{SNR} > 3$ in all the following parameters: σ_* , $v_{\text{H}\alpha}$ ($\text{H}\alpha$ gas velocity), $\sigma_{\text{H}\alpha}$ ($\text{H}\alpha$ gas velocity dispersion), $\text{H}\alpha$ flux, $\text{H}\beta$ flux, $[\text{NII}]\lambda 6585$ flux, $D_n(4000)$ and $\text{EW}(\text{H}\alpha)$. By implementing a stringent SNR cut, we aim to minimize any potential bias and ensure that the comparison between local and global properties is done on a more equal and reliable basis. The global properties of MaNGA galaxies are typically measured with high SNR. If local parameters have lower SNR, it could lead to an underestimation of the correla-

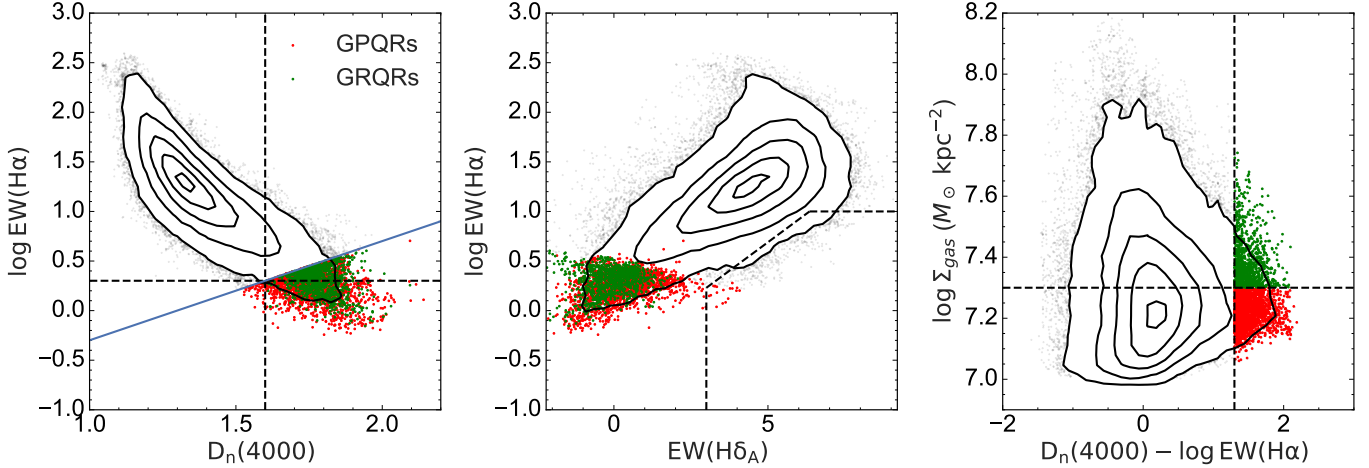


Figure 1. Left panel: The $\log \text{EW}(\text{H}\alpha)$ versus $D_n(4000)$ diagram of our sample. Contour lines represent data percentages (10%, 40%, 70%, 90%, and 99%), while black dots indicate data outside the 99% contour line. GRQRs and GPQRs are denoted by green and red dots, respectively (same for other two panels). The horizontal and vertical dash line represent $\text{EW}(\text{H}\alpha) = 2\text{\AA}$ and $D_n(4000) = 1.6$ separately. Center panel: The $\text{EW}(\text{H}\alpha)$ versus absorption $\text{EW}(\text{H}\delta_A)$ diagram of our sample. The right-bottom corner are post-starburst region according to [Chen et al. \(2019\)](#). Right panel: The $\log \Sigma_{\text{gas}}$ versus $D_n(4000) - \log \text{EW}(\text{H}\alpha)$ diagram of our sample. The horizontal dash line represents the boundary between gas-rich and gas-poor regions at $\log \Sigma_{\text{gas}}(M_{\odot} \text{ kpc}^{-2}) = 7.3$. Spaxels on the right side of the vertical dash line ($D_n(4000) - \log \text{EW}(\text{H}\alpha) > 1.6 - \log 2 \approx 1.3$) are considered as quenched spaxels, which would be found in the lower right side of blue solid line in left panel.

tion between these low SNR parameters and the properties of interest when compared to the global properties. In addition, to ensure reliable measurements of the gas mass surface density (see Appendix B for details), each spaxel has to also meet the following requirements in order to be included: gas-phase color excess $0 < E(B - V) < 1$, molecular gas mass surface density $6.6 < \log(\Sigma_{\text{H}_2}/M_{\odot} \text{ kpc}^{-2}) < 8$, the $[\text{NII}]$ -to- $\text{H}\alpha$ line ratio $-3 < \log([\text{NII}]/\text{H}\alpha) < 1$, the galactic-centric radius within twice the effect radius ($R < 2R_e$) and beyond three times the bulge radius ($R \geq 3R_{e,\text{bulge}}$). With the last criterion we consider only the spaxels in galactic discs. Spaxels within 30° of the minor axis are excluded due to potential measurement inaccuracies in rotation velocity and increased risk of contamination by extraplanar emission. Galaxies that lack spaxels meeting these requirements are automatically excluded from our sample. We have further excluded 21 galaxies whose $\text{H}\alpha$ orientation differs significantly from their stellar orientation. For this purpose, we have compared the isophotes of $\Sigma_{\text{H}\alpha}$ with the ellipse of the r -band light distribution as determined from NSA. The star-forming regions in such “misaligned” galaxies may be dynamically unstable.

Our final sample includes a total of 265,304 spaxels, distributed in 1205 galaxies. This sample will be referred to as our “parent sample” in what follows.

3. RESULTS

3.1. Identification of quenched but gas-rich regions

We firstly identify quenched regions in our galaxies by selecting spaxels with no/weak ongoing star formation and dominated by old stellar populations. In practice, we jointly use $D_n(4000)$ and $\text{EW}(\text{H}\alpha)$ following [Paper I](#), where a spaxel was classified to be a quenched region if $D_n(4000) \geq 1.6$ (dominated by old populations) and $\text{EW}(\text{H}\alpha) \leq 2\text{\AA}$ (consistent with the typical $\text{EW}(\text{H}\alpha)$ ionized by old population; e.g. [Binette et al. 1994](#); [Stasińska et al. 2008](#); [Sarzi et al. 2010](#); [Yan & Blanton 2012](#); [Papaderos et al. 2013](#); [Singh et al. 2013](#); [Sánchez et al. 2014](#); [Belfiore et al. 2016](#); [Gomes et al. 2016](#); [Belfiore et al. 2017](#); [Morisset et al. 2016](#); [Rembold et al. 2017](#); [Zhang et al. 2017](#)). Here, for simplicity, we combine the two criteria into a single one: $D_n(4000) - \log \text{EW}(\text{H}\alpha) \geq 1.6 - \log 2 = 1.3$. The left panel in [Figure 1](#) displays the distribution of all the spaxels from our parent sample in the diagram of $\log \text{EW}(\text{H}\alpha)$ versus $D_n(4000)$, with the new divider indicated by the blue line. The spaxels identified as quenched fall below this line. The horizontal and vertical dashed lines indicate the two single-parameter cuts. As can be seen, the new criterion selects some extra spaxels with $\text{EW}(\text{H}\alpha)$ slightly larger than 2\AA or $D_n(4000)$ slightly smaller than 1.6. In the center panel of the same figure we show the distribution of our sample and the quenched spaxels in the diagram of $\text{EW}(\text{H}\alpha)$ versus $\text{EW}(\text{H}\delta_A)$, equivalent width of the $\text{H}\delta_A$ absorption line. This diagram is commonly used to select post-starburst galaxies/regions, which are expected to fall in the area enclosed by the black dashed lines. The quenched spaxels are located in the lower-left tail of the whole sample, with low values in both parameters indicative of

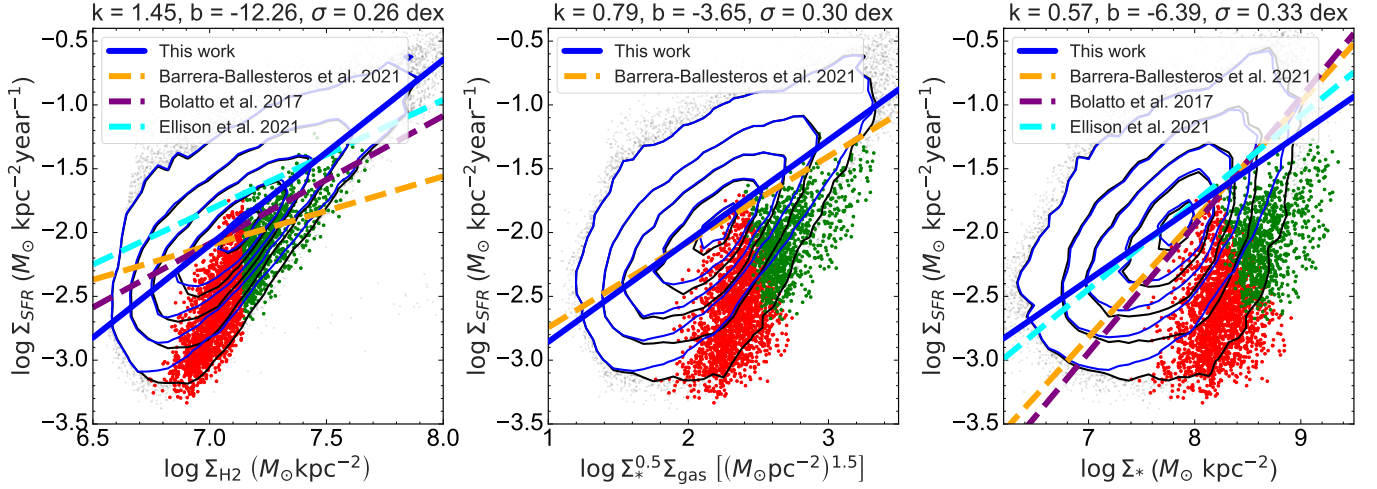


Figure 2. The star formation scaling laws in our sample. From left to right, the three panels show rSK law, extend rSK law and rSFMS, separately. The meanings of green dots and red dots are same as Figure 1. The blue and black contours display the distribution of star-forming regions and all regions in our sample, with each line indicating specific data percentages (10%, 40%, 70%, 90%, and 99%). Additionally, blue and black dots mark data points outside the corresponding 99% contour line. The blue solid lines represent the best-fitted scaling law on the star-forming regions in our sample, while colorful dash lines are scaling laws reported in literatures. Each relation have been converted to the Chabrier (2003) initial mass function case.

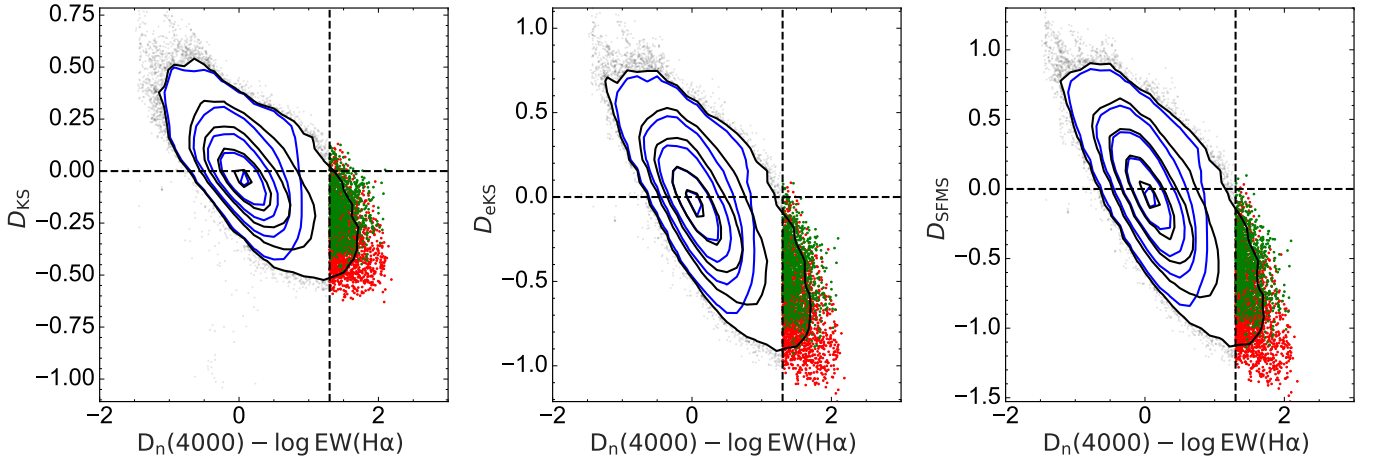


Figure 3. The distance to scaling law versus $D_n(4000) - \log EW(H\alpha)$ diagram for all spaxels in our sample. From left to right, the three panels show the distance to rSK law, extend rSK law and rSFMS, separately. The meanings of contours and dots are same as Figure 2.

weak star formation and old populations. With only a few exceptions, all the spaxels are far away from the post-starburst regime. This implies that these regions have long been quenched, with no strong star formation in the past 1-2 Gyr. We notice that the extra spaxels with $EW(H\alpha)$ slightly higher than 2\AA also have small values in $EW(H\delta_A)$ comparable to the spaxels of $EW(H\alpha) < 2\text{\AA}$.

The rightmost panel of Figure 1 displays the diagram of $\Sigma_{\text{gas}} \equiv \Sigma_{\text{HI}} + \Sigma_{\text{H}_2}$ versus $D_n(4000) - \log EW(H\alpha)$, where we divide the quenched spaxels into two subsamples with $\log(\Sigma_{\text{gas}}/M_\odot \text{kpc}^{-2}) \geq 7.3$ and < 7.3 respectively. This dividing cut is slightly larger than the peak of the full

sample which is at $\log(\Sigma_{\text{gas}}/M_\odot \text{kpc}^{-2}) \sim 7.2$. The two subsamples consist of 1060 gas-rich quenched regions (GRQRs hereafter) and 2069 gas-poor quenched regions (GPQRs hereafter), respectively. As can be seen from the left two panels in Figure 1, the two types of quenched spaxels present similar distributions, indicating similar star formation status. The main purpose of this work is to understand the reason why the two types of regions are both quenched but with so different gas content. We note that the results of our work are robust to the dividing cut which is arbitrarily set at $\log(\Sigma_{\text{gas}}/M_\odot \text{kpc}^{-2}) = 7.3$. We have repeated our analysis by using more extreme selection criteria, with $\log(\Sigma_{\text{gas}}/M_\odot \text{kpc}^{-2}) > 7.4$

for GRQRs and $\log(\Sigma_{\text{gas}}/M_{\odot}\text{kpc}^{-2}) < 7.2$ for GPQRs, finding our main results to remain similar but become more noisy due to smaller sample sizes.

In Figure 2 we further examine the distribution of the GRQRs and GPQRs on three star-forming scaling laws (panels from left to right): Σ_{SFR} versus Σ_{H2} (resolved Schmidt-Kennicutt law, or rSK law; Schmidt 1959, 1963; Kennicutt 1998b), Σ_{SFR} versus $\Sigma_{*}^{0.5}\Sigma_{\text{gas}}$ (extended rSK law, as proposed by Shi et al. 2011, 2018), and Σ_{SFR} versus Σ_{*} (resolved star-forming main sequence, rSFMS). In each panel, the red and green dots display the GPQRs and GRQRs, while the black contours show the distribution of all the spaxels from the parent sample. These scaling laws have been obtained in previous studies at spatial resolutions comparable to or better than those of MaNGA (Bolatto et al. 2017; Lin et al. 2019a; Sánchez 2020; Barrera-Ballesteros et al. 2021; Ellison et al. 2021b; Sánchez et al. 2021b,a; Pessa et al. 2021; Baker et al. 2022; Lin et al. 2022; Sánchez et al. 2023b). For comparison, plotted as colored dashed lines in Figure 2 are the average scaling relations of spatially resolved regions in nearby galaxies, as obtained by previous studies based on MaNGA (Barrera-Ballesteros et al. 2021), EDGE-CALIFA (Bolatto et al. 2017) and ALMaQUEST (Ellison et al. 2021b). Since these relations are usually identified using star-forming relations, for a fair comparison we have specifically selected the star-forming regions from our parent sample by requiring them to have $\text{EW}(\text{H}\alpha) > 6$ (Cid Fernandes et al. 2010; Sánchez et al. 2014; Morisset et al. 2016; Sánchez et al. 2021a) and fall below the Kauffmann et al. (2003) line in the BPT diagram. The distribution of this sample is shown as blue contours in the same figure, and the best-fitted linear relation of the star-forming regions, as obtained by applying the Ordinary Least Squares (OLS) algorithm, is plotted as the blue solid line in each panel. The best-fit parameters (slope k , intercept b , scatter σ) are indicated above each panel. Overall, both the best-fit relation and the scatter from our sample are consistent with one or multiple of the previous studies. Differences between different studies may be caused by different sample selections, different ways of estimating gas mass fractions, and different fitting algorithms.

As can be seen from Figure 2, the majority of the quenched spaxels including both GRQRs and GPQRs fall below the average relations in all the panels. The fall of quenched regions below the rSFMS suggests a reduction in specific star formation rate (sSFR), while the fall below the rSK law suggests a reduction in star formation efficiency (SFE). This behaviour is more clearly seen from Figure 3, where we show the deviation of spaxels from the average relations as functions of $D_n(4000)\text{-logEW}(\text{H}\alpha)$, the single parameter adopted above for the selection of quenched regions. This parameter shows an anti-correlation with the deviation in all the panels. In particular, we find most of the quenched regions defined by this parameter have negative deviations, while those

with negative deviations span a wide range in this parameter, i.e. not all of them are quenched. In other words, to fall below the star-forming scaling relations is a necessary condition, but not a sufficient condition for a spaxel to be considered as a quenched region. This is because our selection criteria require the quenched regions to be not only weak in ongoing star formation, but also dominated by old stellar populations.

3.2. Global properties of host galaxies

In Figure 4 we examine the global properties of the host galaxies of both GRQRs and GPQRs. The properties considered include color index $NUV - r$, the total SFR, the r -band effective radius R_{50} , Sérsic index n , concentration index R_{90}/R_{50} , the surface stellar mass density within the central 1kpc $\Sigma_{1\text{kpc}}$, morphology as quantified by T-type, the bulge-to-total luminosity ratio B/T , and the minor-to-major axis ratio b/a as measured from r -band images. Here, R_{50} and R_{90} are the radii enclosing 50% and 90% of the total light in r -band. Among these properties, total SFRs and stellar mass are taken from GSWLC (Salim et al. 2016, 2018), T-types are from Domínguez Sánchez et al. (2018), B/T from Meert et al. (2016), $\Sigma_{1\text{kpc}}$ are measured by ourselves from the MaNGA data, and all the rest properties are provided in NSA.

In the figure the host galaxies of GRQRs and GPQRs are plotted as green and red dots. For comparison, we plot the distribution of all the galaxies in the parent sample (blue dots) from which the quenched regions are selected, as well as the distribution of the full sample of MaNGA galaxies from SDSS/DR17 as the background contours, for which we have corrected the incompleteness due to MaNGA sample selection using the weights provided by Wake et al. (2017). By selection, our parent sample includes only late-type galaxies (T-type ≥ 0 and $B/T < 1$) with no signatures of interaction/merger. As expected, this sample is dominated by globally blue and star-forming galaxies with relatively large size and low concentration, Sérsic index and B/T at fixed mass. The quenched regions including both GRQRs and GPQRs tend to be hosted by massive galaxies ($M_{*} \gtrsim 10^{10}M_{\odot}$) with relatively red colors ($NUV - r \gtrsim 3$), low SFR and high central density at fixed mass, but spanning wide ranges in other parameters that are similar to the parent sample. We note that our sample spans a full range of b/a , indicating that our sample selection is not biased by dust extinction effect. It is interesting to note that the GRQRs and GPQRs are similar in all the host galaxy properties considered, and that most of the host galaxies of GRQRs also host GPQRs at the same time. This strongly implies that the conditions responsible for GRQRs/GPQRs must be largely independent on the global properties of their host galaxies. Rather, local processes on scales of the MaNGA spaxels or even smaller scales are more likely to be at work.

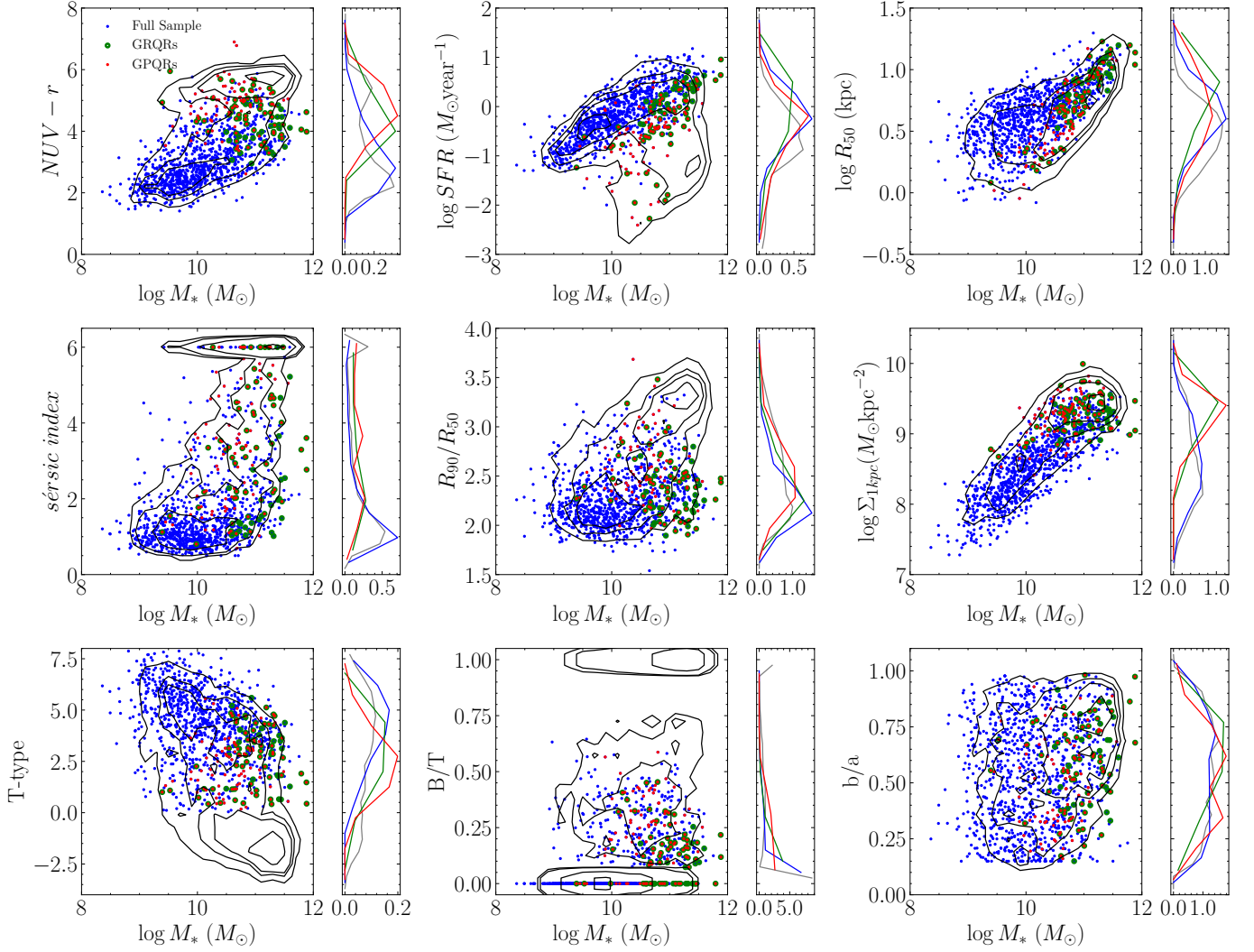


Figure 4. Comparison of global properties among all MaNGA galaxies (background contour, the contour lines include 10%, 40%, 70% and 90% data separately), galaxies in our sample (blue dots), the host galaxies of GRQRs (green ring) and the host galaxies of GPQRs (red dots). The distribution of MaNGA galaxies are corrected by galaxy weight. Each panel is a y-axis parameter versus galaxy mass diagram. The y-axis parameters of these nine panels are color ($NUV - r$), logarithmic star formation rate, galaxy size, Sérsic index, Concentration (r_{90}/r_{50}), stellar mass surface density in central 1 kpc, T-type, B/T, and axial ratio (b/a), from left to right, and top to bottom. The sub-panel in right side of each panel is the probability density profile of y-axis parameter. Note that for the host galaxies of GPQRs, the red dots cover the blue dots, which leads to these dots show as a red one.

Figure 5 displays the BPT diagram (Baldwin et al. 1981) for the host galaxies of GRQRs and GPQRs, compared to the parent sample and the full MaNGA sample. We use the emission line measurements from the central spaxels in MaNGA datacubes. We use the empirical criteria from Kewley et al. (2001) and Kauffmann et al. (2003) to divide the diagram into three regimes dominated by different ionizing sources. The left panel show the results for all the host galaxies as a whole, while the center and right panels show the results separately for the two subsets of host galaxies with central $EW(H\alpha)$ values being either $< 3\text{\AA}$ or $\geq 3\text{\AA}$. This division is suggested in the literature (e.g. Cid Fernandes et al. 2010,

2011; Sánchez et al. 2014, 2018; Sánchez 2020; Sánchez et al. 2021a) to mitigate the confusion arising from different ionization conditions based solely on the location in the BPT diagram. Although inaccurate for individual sources, this $EW(H\alpha)$ threshold statistically distinguishes the ionization dominated by AGN ($EW(H\alpha) \geq 3\text{\AA}$) from that dominated by low mass evolved stars ($EW(H\alpha) < 3\text{\AA}$). Overall, the galaxies hosting GRQRs and GPQRs exhibit similar distributions in the BPT diagram, predominantly located above the line defined by Kewley et al. (2001). These galaxies mainly have $EW(H\alpha) < 3\text{\AA}$. The fraction of the quenched region host galaxies that satisfy $EW(H\alpha) \geq 3\text{\AA}$ and locate above the

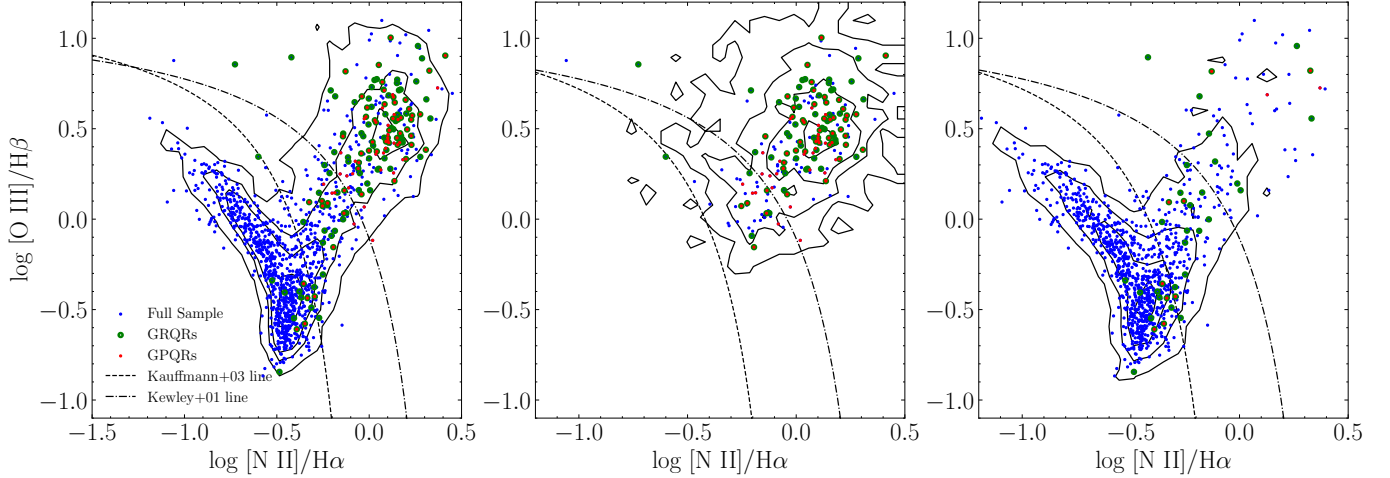


Figure 5. BPT diagnostics of our sample. We use the line ratios of central spaxels to trace the existence of AGN for MaNGA galaxies (background contour, the contour lines include 10%, 40%, 70% and 90% data separately), galaxies in our sample (blue dots), the host galaxies of GRQRs (green ring) and the host galaxies of GPQRs (red dots). The distribution of MaNGA galaxies have been corrected by the galaxy weight. The center and right panel is same as left panels but for retired galaxies (central $\text{EW}(\text{H}\alpha) < 3 \text{ \AA}$) and star forming galaxies (central $\text{EW}(\text{H}\alpha) > 3 \text{ \AA}$), separately.

line defined by Kauffmann et al. (2003) is limited. In addition to the $\text{EW}(\text{H}\alpha)$, the central $\text{H}\alpha$ velocity dispersion $\sigma_{\text{H}\alpha,c}$ can also provide complementary information for ionization condition classification. By following the criteria $\text{EW}(\text{H}\alpha) > 3 \text{ \AA}$ and $\sigma_{\text{H}\alpha,c} > 57 \text{ km s}^{-1}$ as suggested by Sánchez et al. (2024) for AGN selection, the AGN fraction in the host galaxies of quenched regions is approximately 20%. These results suggest that the majority of host galaxies of both types of quenched regions are not obviously AGN host galaxies. The similarity between the GRQRs and GPQRs again indicates weak or no dependence of quenching on the global properties of host galaxies.

3.3. Significance of resolved properties to quenching

In this section, we investigate the significance of resolved properties in relation to the quenching of the selected spaxels. We have a range of resolved properties available, and there may be potential interaction effects among these properties. Therefore, we employ the Gini importance value provided by the random forest classifier as a data-driven method to identify the important properties while considering the interaction effects. The random forest algorithm is implemented using Scikit-learn (Pedregosa et al. 2011). Although our focus is on resolved properties in this section, we also include some global properties in the input of the random forest classifier for completeness. The resolved properties include various parameters that carry local stellar population information. These include Σ_* (stellar surface mass density), Z_* (stellar metallicity), $\log t_{\text{age}}$ (logarithm of stellar age), and Σ_{SFR} (star formation rate surface density). Additionally, the analysis incorporates kinematic information such as $\sigma_{\text{H}\alpha}$ ($\text{H}\alpha$ gas velocity dispersion) and σ_* (stellar velocity dispersion). Gas phase informa-

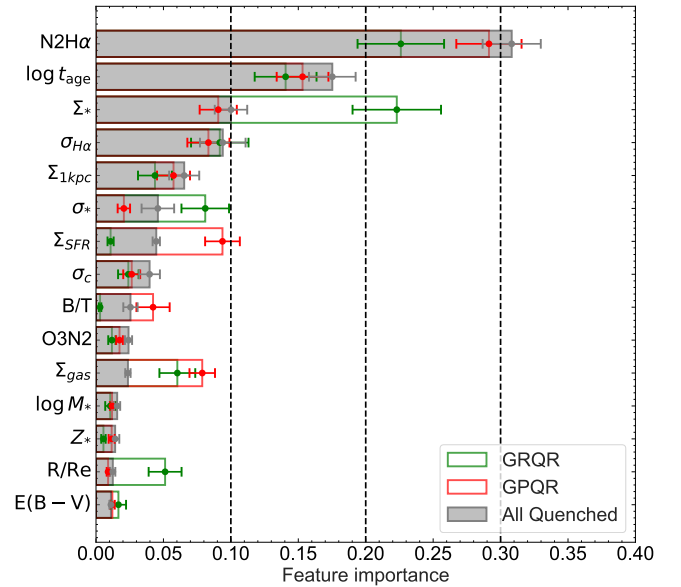


Figure 6. The Gini feature importance for selecting quenched regions (gray), GPQRs (red), and GRQRs (green) of each input property. The error bar shows 1σ uncertainty of importance, estimated by re-selecting the subsample of non-quenched spaxels and re-splitting the train/test set.

tion is also considered, including $E(B - V)$ (gas phase color excess), Σ_{gas} (gas surface mass density), $\text{N2H}\alpha \equiv [\text{NII}]/\text{H}\alpha$ (ratio of $[\text{NII}]$ to $\text{H}\alpha$ flux), and $\text{O3N2} \equiv \log([\text{OIII}]/\text{H}\beta) - \log([\text{NII}]/\text{H}\alpha)$. Finally, the location within the host galaxy is represented by R/Re , which denotes the galactic-centric radius normalized by the effective radius. The global properties include $\log M_*$ (logarithm of global stellar mass), B/T (bulge-to-total luminosity

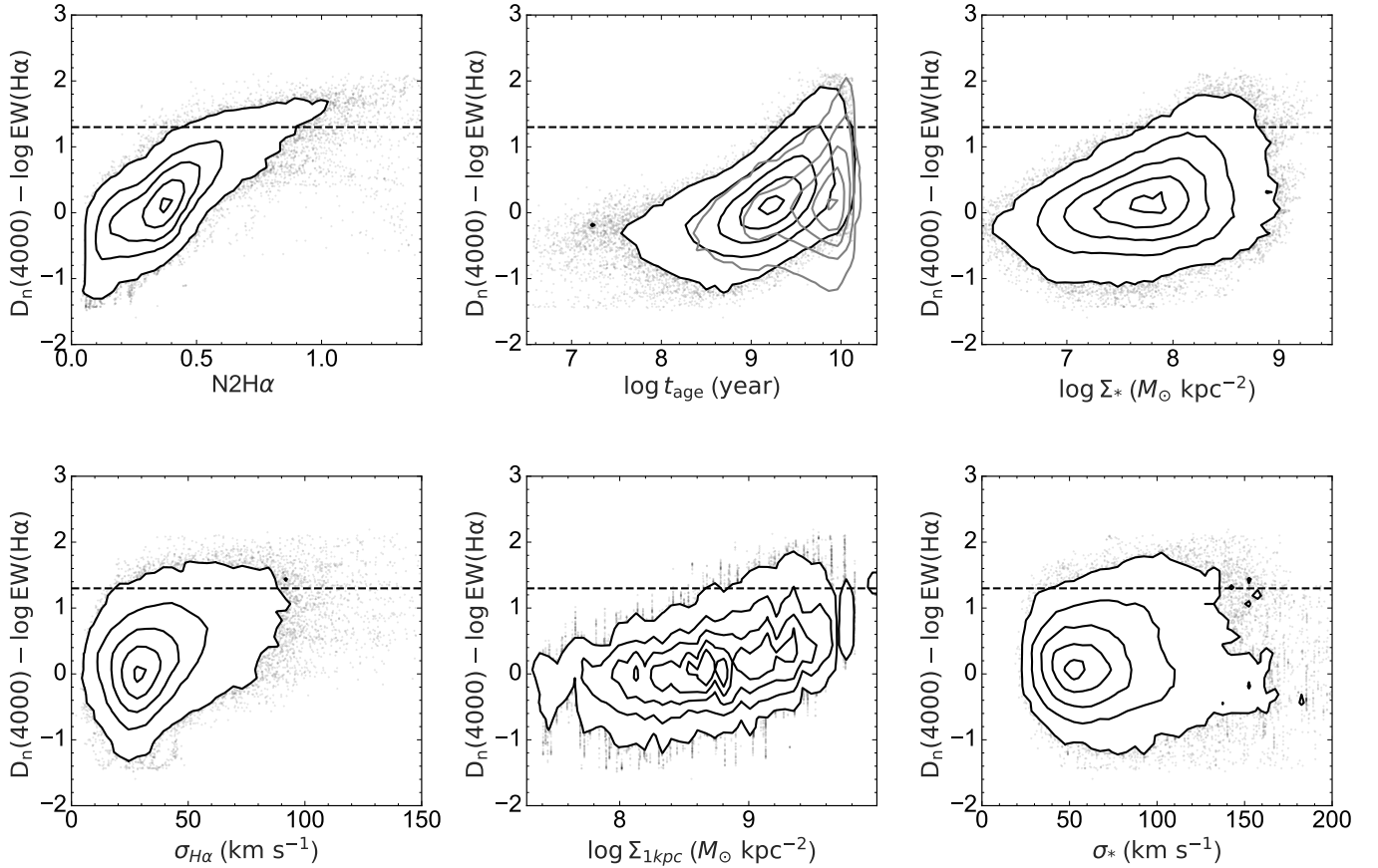


Figure 7. The correlation between $D_n(4000) - \log \text{EW}(\text{H}\alpha)$ and the properties with top 6 highest Gini importance. The dashed horizontal line shows the criterion we used to select quenched region in Figure 1. The meanings of contours and black dots are same as Figure 1. The gray contours in top center panel show the joint distribution of mass weighted age and $D_n(4000) - \log \text{EW}(\text{H}\alpha)$.

ratio), $\Sigma_{1\text{kpc}}$ (stellar surface mass density within central 1 kpc), and σ_c (central stellar velocity dispersion). For stellar age, we utilize the luminosity-weighted version as it is more strongly correlated with the quenching process compared to the mass-weighted age. This result aligns with the well-known correlation between $\text{EW}(\text{H}\alpha)$, $D_n(4000)$, and luminosity-weighted stellar age (see Sánchez 2020; Sánchez et al. 2021a, 2022, 2023a, for recent reviews). If we were to use both luminosity-weighted and mass-weighted age, these two properties would share their importance with each other, leading to an underestimation of their individual contributions. Similarly, for stellar metallicity, we employ the luminosity-weighted version for self-consistency. We note that, although SFE (defined as $\Sigma_{\text{SFR}}/\Sigma_{\text{gas}}$) and cold gas fraction f_{gas} (defined as $\Sigma_{\text{gas}}/(\Sigma_{\text{gas}} + \Sigma_*)$) are expected to play important roles in understanding star formation quenching, we have chosen not to include them in the random forest analysis for the following two considerations. First, both SFE and f_{gas} are mathematically related to SFR, Σ_{gas} and Σ_* , which are already included in our analysis. Inclusion of mathematically-related parameters would create redundancy, and thus artificially di-

minish the importance of these parameters, known as the "dilution effect". In this case, we prefer to include original observables and more-directly derived parameters, rather than less-directly derived parameters. Secondly and more importantly, it would be difficult to interpret the importance of SFE and f_{gas} individually, as each is a combination of two underlying parameters. For instance, a lower gas mass at a given stellar mass or a higher stellar mass at a given gas mass could both lead to a low f_{gas} .

To address the imbalance between non-quenched and quenched spaxels, we randomly select a subsample of non-quenched spaxels that matches the number of quenched spaxels. This subsample is used alongside the quenched spaxels for training the random forest classifier. The training/test set is randomly split in an 8:2 ratio. The classifier achieves an accuracy of approximately 98% on the test set, indicating that the considered physical properties as a whole provide complete description of the quenching status of resolved regions. We estimate the uncertainty of importance by re-selecting the subsample of non-quenched spaxels and re-splitting the training/test set. The importance of the properties

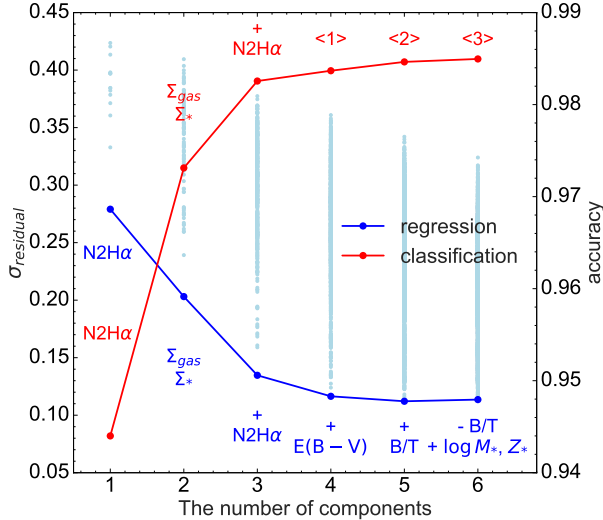


Figure 8. The figure displays the standard deviation of the residuals for the best combination with a given number of features ($N_{\text{comp.}}$) in blue, while the standard deviation of residuals for other combinations are depicted as light blue dots. The red line demonstrates the best balanced accuracy of classifying the quenching state with a given $N_{\text{comp.}}$. The label <1> denotes Σ_* , Σ_{gas} , $E(B-V)$, and R/R_e ; <2> represents Σ_* , Σ_{gas} , $\log M_*$, $\Sigma_{1\text{kpc}}$, σ_c ; and <3> corresponds to Σ_* , Σ_{gas} , $N2H\alpha$, $\log M_*$, $\Sigma_{1\text{kpc}}$, σ_c .

and the uncertainty are depicted in Figure 6, where the properties are ordered by decreasing the importance. As shown, the most important property is $N2H\alpha$, followed by $\log t_{\text{age}}$, Σ_* , $\sigma_{H\alpha}$, $\Sigma_{1\text{kpc}}$ and σ_* . The order of importance indicates that the quenching of local regions is primarily related to local physical properties rather than global properties. Importantly, it should be noted that the feature importance attributed by the random forest method only denotes correlation and not necessarily causation. In addition, to test the potential bias in the importance ranking caused by the estimated Σ_{gas} , we have repeated the analysis by excluding Σ_{gas} and found no significant changes in the importance ranking of other features.

To gain a perceptual understanding, we plot the correlation between our quenching parameter, $D_n(4000) - \log EW(H\alpha)$ and the top six important properties in Figure 7. The horizontal dashed line indicates the criterion for selecting the quenched regions. For stellar age, we additionally show the result for mass-weighted stellar age for comparison with the luminosity-weighted age. As expected, the mass-weighted age is systematically higher than the luminosity-weighted age as the former is dominated by old populations, and for the same reason the luminosity-weighted age exhibits a stronger correlation with $D_n(4000) - \log EW(H\alpha)$ when compared to the mass-weighted age. As the top-ranked property, $N2H\alpha$ indeed exhibits an obvious correlation with $D_n(4000) -$

$\log EW(H\alpha)$, but this property still spans a large dynamical range for the quenched regions. For $\log t_{\text{age}}$, Σ_* , and $\Sigma_{1\text{kpc}}$, the quenched regions have a narrow dynamical range in these properties, but not all regions with these properties falling in this range are necessarily quenched. On the other hand, quenched regions demonstrate relatively higher $\sigma_{H\alpha}$ and σ_* compared to non-quenched regions, which aligns with the overall trend identified by Law et al. (2021), who found that LI(N)ER spaxels exhibit higher $\sigma_{H\alpha}$ and σ_* . However, the dynamical range for $\sigma_{H\alpha}$ and σ_* is wide, and their correlations with $D_n(4000) - \log EW(H\alpha)$ are not strong. This could be attributed to our focus on the disk component of late-type galaxies. It is widely acknowledged that the spheroidal component is predominantly older and pressure-dominated. These findings, coupled with the high accuracy of the random forest classifier, suggest that quenching cannot be predicted by a single property but rather by a combination of multiple properties.

We further explore different combinations of the properties that can effectively predict the quenching state of the resolved regions. For this purpose we consider all possible parameter combinations, and for a given combination we train the random forest regressor for predicting $D_n(4000) - \log EW(H\alpha)$. In Figure 8, the five-fold cross-validation residual scatters σ_{residual} for all the parameter combinations are plotted as the light-blue dots against the number of parameters involved in the combinations. The combinations with the smallest value of σ_{residual} at given parameter number are highlighted as the blue dots, connected by the solid blue line. When only one parameter is utilized, $N2H\alpha$ emerges as the most effective choice, consistent with the analysis above. When combining two of the properties, we find the most effective combination is the one formed by Σ_* and Σ_{gas} , which significantly lower down the residual scatter when compared to $N2H\alpha$ alone or any other two-parameter combinations. These two parameters together with $N2H\alpha$ form the most effective combination of three parameters, with which σ_{residual} drops significantly. As we incorporate additional parameters, $E(B-V)$ is introduced for four-parameter combinations, and B/T for five-parameter combinations. However, the reduction in σ_{residual} is relatively limited.

In addition to the regression analysis, we also use the different combinations of the properties to train the random forest classifier in order to find the best combinations that can predict whether a region is quenched or not. The best five-fold cross-validation balanced accuracy as a function of the number of parameters is plotted as the red line in the Figure 8. The best combinations involving one, two, and three parameters are the same as those resulted from the regression analysis, as indicated in the figure. The classification accuracy is $> 98\%$ for the three-parameter combination of Σ_{gas} , Σ_* and $N2H\alpha$. For combinations involving a larger number of parameters, we find different parameters may be used in cases

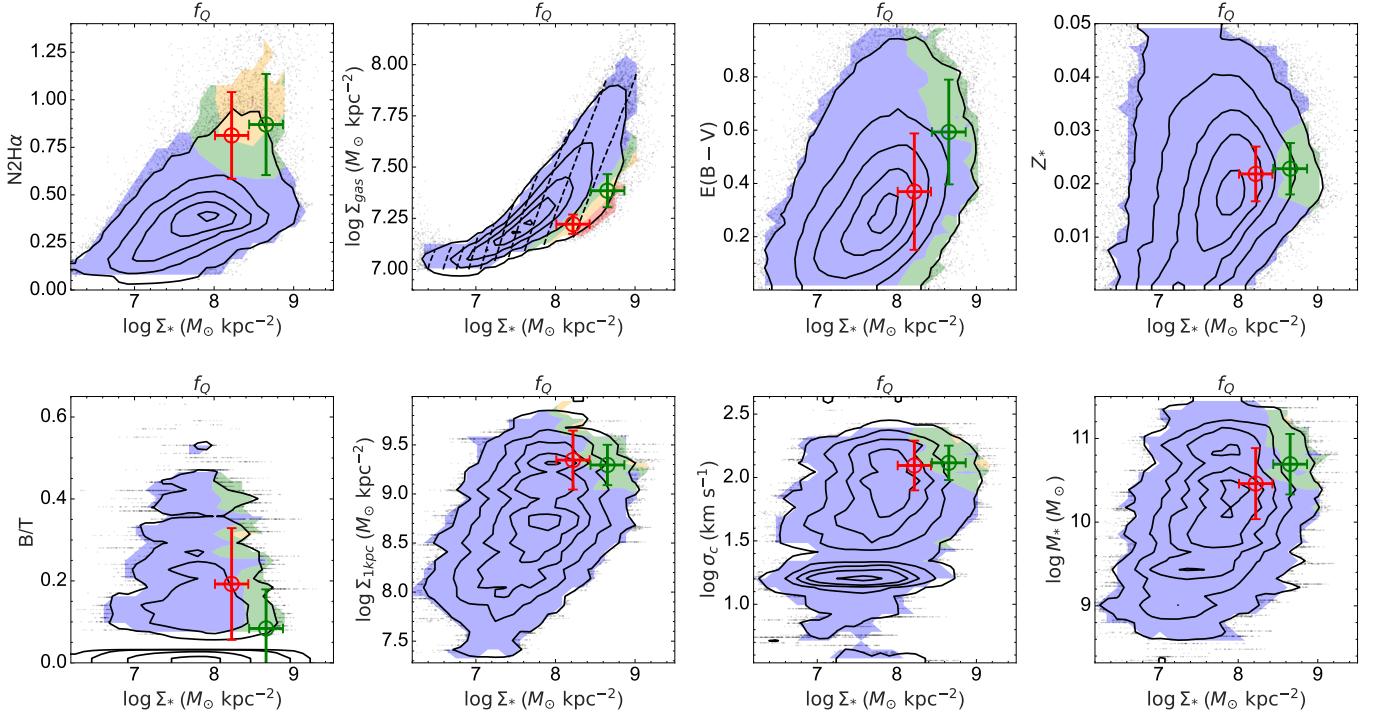


Figure 9. Each panel is a y-axis versus $\log \Sigma_*$ diagram. The colors blue, green, yellow, and red correspond to the f_Q intervals of 0.0 - 0.1, 0.1 - 0.5, 0.5 - 0.9, and 0.9 - 1.0 separately. The y-axes in the first row represent local parameters $N2H\alpha$, $\log \Sigma_{gas}$, $E(B - V)$, and Z_* , while the y-axes in the second row denote global parameters B/T , $\log \Sigma_{1kpc}$, $\log \sigma_c$, and $\log M_*$. The meanings of black contours and dots are same as Figure 1. The mean value and 1σ scatter of GRQRs and GPQRs are shown as red and green circles with error bar, separately. In the second panel of the first row, the contours of f_{gas} are shown as black dashed lines.

of different parameter numbers, but Σ_{gas} and Σ_* are always simultaneously included in the combinations. This result again implies the important roles of both Σ_{gas} and Σ_* for quenching.

It is worth noting that this combination analysis is based on the estimated Σ_{gas} , which relies on parameters used to define quenching. Although our test in Figure B18 shows no bias in the estimated Σ_{gas} with respect to $D_n(4000)$ and $EW(H\alpha)$ in the first order, one may still worry about the potential risk associated with the combination of parameters, and the results of this combination analysis should be interpreted with caution. Our result may be verified or refined in future works using real observations of Σ_{gas} or an estimator that does not explicitly rely on $EW(H\alpha)$.

We further investigate the dependency of quenching on the combination of different parameters by Figure 9. To emphasize the role of Σ_* , each panel in the figure displays the distribution of the parent sample of spaxels on the diagram of a second property versus Σ_* , plotted as solid black contour lines. The secondary properties considered are those that appear in the best combination of our random forest classifier or regressor. In each panel, the blue, green, yellow, and red colors correspond to the f_Q intervals of 0.0 - 0.1, 0.1 - 0.5, 0.5 - 0.9, and 0.9 - 1.0, respectively. Here, f_Q represents the frac-

tion of quenched regions meeting our quenching selection criterion. As can be seen, fully quenched regions with $f_Q > 0.9$ can be selected out only through a combination of Σ_{gas} and Σ_* (the second panel in the upper row). Additionally, regions with $f_Q > 0.5$ can be identifiable by combining Σ_* with $N2H\alpha$, as shown in the leftmost panel in the upper row. In other panels there is nowhere for $f_Q \geq 0.5$, indicating that none of the pairwise combinations of those properties are sufficient for predicting quenching. In each panel the mean and 1σ scatter of GRQRs and GPQRs are additionally plotted as the green and red circles with error bars. Only in the first two panels in the upper row, as expected, the locations of the quenched regions agree with the quenched regions indicated by the contours of high f_Q . This result shows that the combinations of Σ_* with either $N2H\alpha$ or Σ_{gas} provide sufficient criteria for quenching. We have repeated the above analysis for all the other pairwise combinations using the properties that appear in this plot, and found none of them can indicate quenching as efficiently as the combinations in the first two panels of Figure 9.

In the panel of Σ_* versus Σ_{gas} , we additionally show the distribution of the gas fraction f_{gas} as dashed black contours. It is evident that the overall trend of f_{gas} aligns with the contour lines of f_Q , emphasizing the sig-

nificant role of f_{gas} in quenching. As aforementioned, however, attributing the lower f_{gas} solely to a lower gas mass at a given stellar mass can only account for the drop from the rSFMS, but not the drop from the rSK law which requires a decrease in the SFE at a given gas mass. Otherwise, the quenched region would only shift along the rSK law from the upper-right to the lower-left. Therefore, our result emphasizes the importance of the combination of f_{gas} and SFE for quenching, which is broadly consistent with previous studies (Colombo et al. 2018, 2020; Ellison et al. 2020, 2021b; Sánchez et al. 2021b; Kalinova et al. 2022). This appears to conflict with the finding that the combination of Σ_{gas} and Σ_* can efficiently select quenched regions, as the SFE is not immediately known with the combination of these two parameters. A natural explanation is that the lower f_{gas} should also be considered as the presence of more stars at a given gas mass, which will have a net negative effect on star formation, leading to the decrease of SFE.

Further insight can be gained by repeating our random forest analysis for the GRQRs and GPQRs separately. The results are shown in Figure 6. For GRQRs, the importance of Σ_* and σ_* is significantly enhanced, while the importance of Σ_{SFR} is suppressed. In contrast, for GPQRs, the importance of Σ_{SFR} is enhanced to be comparable to that of Σ_* . This result suggests that, for GRQRs, the decrease of SFE at a given Σ_{gas} is highly correlated with the high Σ_* , which leads to a lower f_{gas} at the same time. For GPQRs, the decrease of SFE is much more independent of the value of Σ_* , thus the additional information of Σ_{SFR} should be included to effectively select such regions. The enhancement of the importance of Σ_{gas} is trivial, as GRQRs and GPQRs are separated by Σ_{gas} . The enhancement of the importance of R/Re is influenced by the Σ_* profile of the galaxy, as GRQRs tend to be found in the inner disk, which have a higher Σ_* .

In conclusion, we identify N2H α , Σ_{gas} , and Σ_* as the most significant properties associated with quenching. For gas-rich regions, Σ_* is a particularly significant property, which potentially drives the simultaneous decrease of f_{gas} and SFE. For GPQRs, the decrease of SFE is also necessary but is more independent of Σ_* . Additionally, GRQRs exhibit higher E(B - V) than GPQRs. These differences should be attributed to the distinct quenching mechanisms associated with the different gas content of GRQRs and GPQRs, a topic that will be discussed in section 4.

3.4. Dependence on quenching definition

The quenched regions in our sample are selected to simultaneously have $\text{EW}(\text{H}\alpha) < 2\text{\AA}$ (thus with no/weak ongoing star formation) and $D_{\text{n}}(4000) > 1.6$ (thus with no/little stellar populations younger than 1-2 Gyr). This definition has been widely adopted in previous studies (e.g. Geha et al. 2012; Wang et al. 2018). For simplicity, we have combined the two criteria and in-

troduced a single-parameter selection: $D_{\text{n}}(4000) - \log \text{EW}(\text{H}\alpha) \geq 1.3$, which is shown to result in a sample similar to the one selected jointly by the two separate criteria (see Figure 1). On the other hand, as mentioned, some other studies have used different definitions for quenching. For instance, Lin et al. (2019b) defined quenched regions as non-star-forming regions on BPT diagrams that have $\text{EW}(\text{H}\alpha) < 3\text{\AA}$, while Bluck et al. (2020a,b) also used BPT diagrams to select non-SF regions and essentially used $D_{\text{n}}(4000)$ to further select regions of low sSFR. In order to examine the dependence on quenching definition, we have selected two new samples of “quenched regions” from our parent sample, by applying the definitions in Lin et al. (2019b) and Bluck et al. (2020a,b). We note that, for the definition of Bluck et al. (2020a,b), we didn’t attempt to estimate sSFRs by $D_{\text{n}}(4000)$ for passive regions and then select quenched regions by sSFRs. Instead, we simply apply a cut of $D_{\text{n}}(4000) > 1.45$ to the non-star-forming regions, which results in closely matching samples of quenched regions as discussed in Bluck et al. (2020a,b).

In Figure 10, we show the distribution of the two samples of quenched regions in the diagrams formed by $\text{EW}(\text{H}\alpha)$, $D_{\text{n}}(4000)$, $\text{EW}(\text{H}\delta_{\text{A}})$, Σ_{gas} and $D_{\text{n}}(4000) - \log \text{EW}(\text{H}\alpha)$, in the same way as in Figure 1. When compared to the quenched regions in our sample, the quenched regions defined jointly by $\text{EW}(\text{H}\alpha)$ and BPT diagrams as in Lin et al. (2019b) cover similar ranges in $D_{\text{n}}(4000)$, $\text{EW}(\text{H}\delta_{\text{A}})$ and $D_{\text{n}}(4000) - \log \text{EW}(\text{H}\alpha)$, although they have slightly stronger H α emission due to the higher $\text{EW}(\text{H}\alpha)$ threshold. In contrast, the quenched regions defined by $D_{\text{n}}(4000)$ and BPT diagrams as in Bluck et al. (2020a,b) cover wider ranges in those parameters, extending to much higher $\text{EW}(\text{H}\alpha)$ and lower $D_{\text{n}}(4000)$. The similarity of our sample to Lin et al. (2019b) can be understood from the similar cuts in $\text{EW}(\text{H}\alpha)$ as adopted in both studies. As can be seen from the $\text{EW}(\text{H}\alpha)$ - $D_{\text{n}}(4000)$ diagram, regions with substantially low $\text{EW}(\text{H}\alpha)$ appear to mostly have the highest values of $D_{\text{n}}(4000)$, while a substantially high $D_{\text{n}}(4000)$ doesn’t necessarily lead to low $\text{EW}(\text{H}\alpha)$. This fact also explains the difference of our sample from that of Bluck et al. (2020a,b), which is selected by $D_{\text{n}}(4000)$ but not $\text{EW}(\text{H}\alpha)$. Therefore, the differences in the different samples of quenched regions are essentially caused by the different requirements on H α emission.

We then apply the random forest classifier to identify important properties related to quenching in both samples. We first consider the same set of properties as analyzed above for our sample. The results are shown in the upper panels in Figure 11. For comparison, the result of our sample is repeated here as the upper left panel. We see that N2H α is top ranked in all the samples. This result is not unexpected for the two new samples, which are both selected by BPT diagrams involving N2H α . We have repeated the analysis without N2H α , finding the ranking of the rest properties

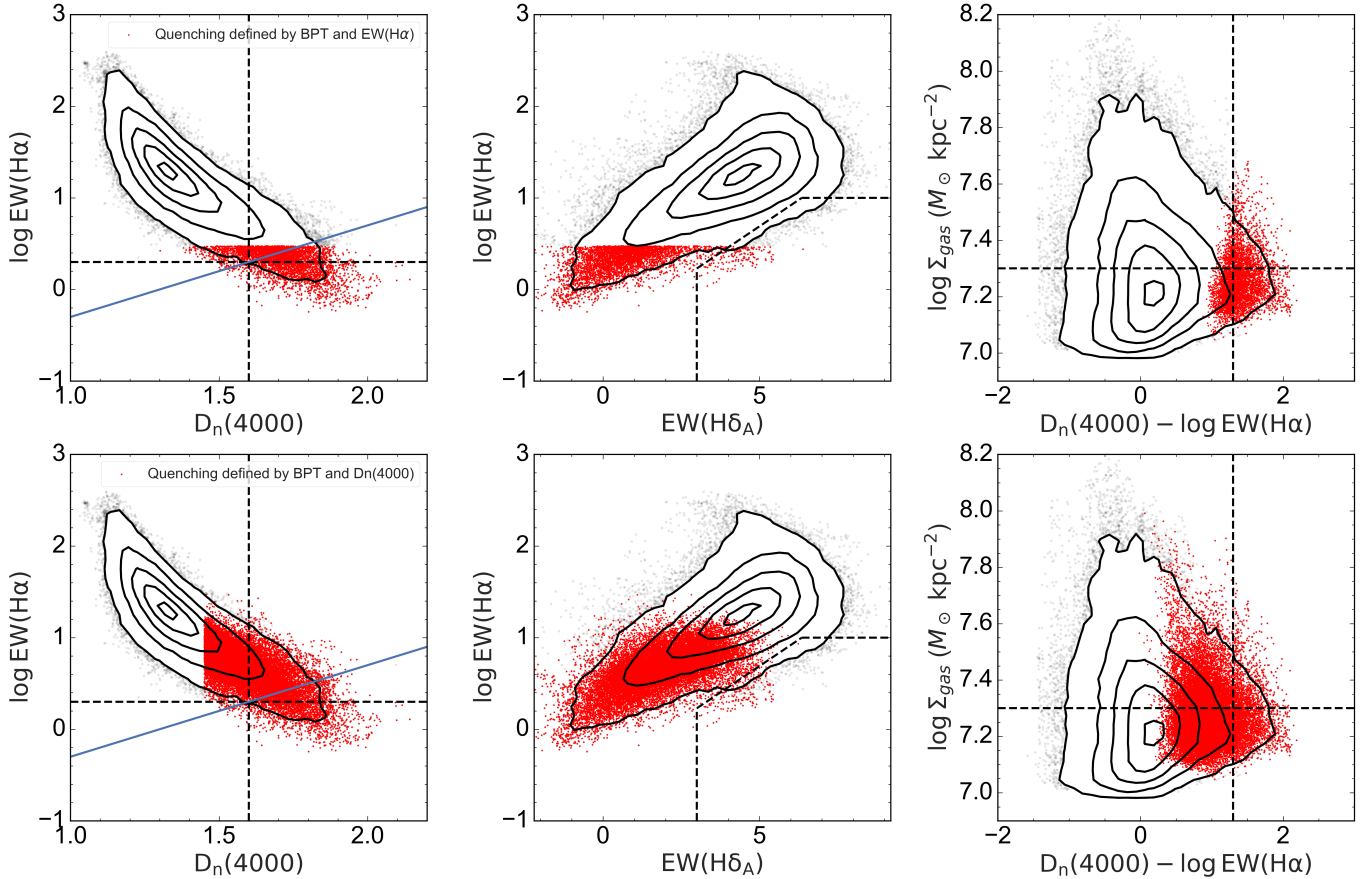


Figure 10. The distribution of resolved regions of our sample on the diagram of $\log EW(H\alpha)$ versus $D_n(4000)$ (left), $\log EW(H\alpha)$ versus $EW(H\delta_A)$ (center), and $\log \Sigma_{\text{gas}}$ versus $D_n(4000) - \log EW(H\alpha)$ (right). The red dots in each panel represent the subsample of “quenched regions”, which are defined jointly by BPT diagrams and $EW(H\alpha) < 3\text{\AA}$ following Lin et al. (2019b) (upper panels), or jointly by BPT diagrams and $D_n(4000) > 1.45$ following Bluck et al. (2020a,b) (lower panels).

remain unchanged although the absolute value of feature importance increases to varying degrees for all the properties. As expected, the sample defined following Lin et al. (2019b) behaves similarly to our sample, with $\log t_{\text{age}}$, $\sigma_{H\alpha}$, Σ_* and Σ_{SFR} being the most important properties. Differently, for the sample defined following Bluck et al. (2020a,b), the most important properties are $\log t_{\text{age}}$, σ_c , $\sigma_{H\alpha}$ and $\Sigma_{1\text{kpc}}$. One may wonder whether the difference is caused by the lower $D_n(4000)$ threshold ($D_n(4000) > 1.45$) adopted by Bluck et al. (2020a,b). To test this out, we have increased the cut to $D_n(4000) > 1.6$ to mimic our selection and repeated the analysis. Plotted as the yellow histograms in the same panel, the result becomes more similar to our sample in the sense that the feature importance increases for $\log t_{\text{age}}$ and $\sigma_{H\alpha}$, but the relatively high importance of σ_c and $\Sigma_{1\text{kpc}}$ and low importance of Σ_* remain. In the lower panel, we repeat the analysis for the three samples but considering a subset of properties similar to those considered in Bluck et al. (2020a,b). Again, our sample and the one defined following Lin et al. (2019b) present similar results as expected. For the third sample, σ_c and $\Sigma_{1\text{kpc}}$ become

most important, consistent with Bluck et al. (2020a,b). The two properties are still top ranked if $D_n(4000) > 1.6$ instead of $D_n(4000) > 1.45$ is applied in the sample selection, as shown by the yellow histograms. This result suggests that the definition of quenching can significantly impact the ranking of feature importance, leading to different conclusions. If $EW(H\alpha)$ is not considered in the quenching definition, the quenching of resolved regions could be efficiently predicted by σ_c or $\Sigma_{1\text{kpc}}$. This suggests that quenching is a global process, with a significant central bulge and possibly a central supermassive black hole playing a major role in the quenching process. However, when an $EW(H\alpha)$ cut is applied, the importance of σ_c and $\Sigma_{1\text{kpc}}$ decreases significantly, indicating that quenching is a local process.

It is important to note that the difference between our sample and Bluck et al. (2020a,b) lies not only in the definition of quenching but also in our focus on the disk component of late-type galaxies. Our sample should be considered as a subset of the sample used by Bluck et al. (2020a,b). Therefore, the disparities between our findings and those of Bluck et al. (2020a,b) can partly be

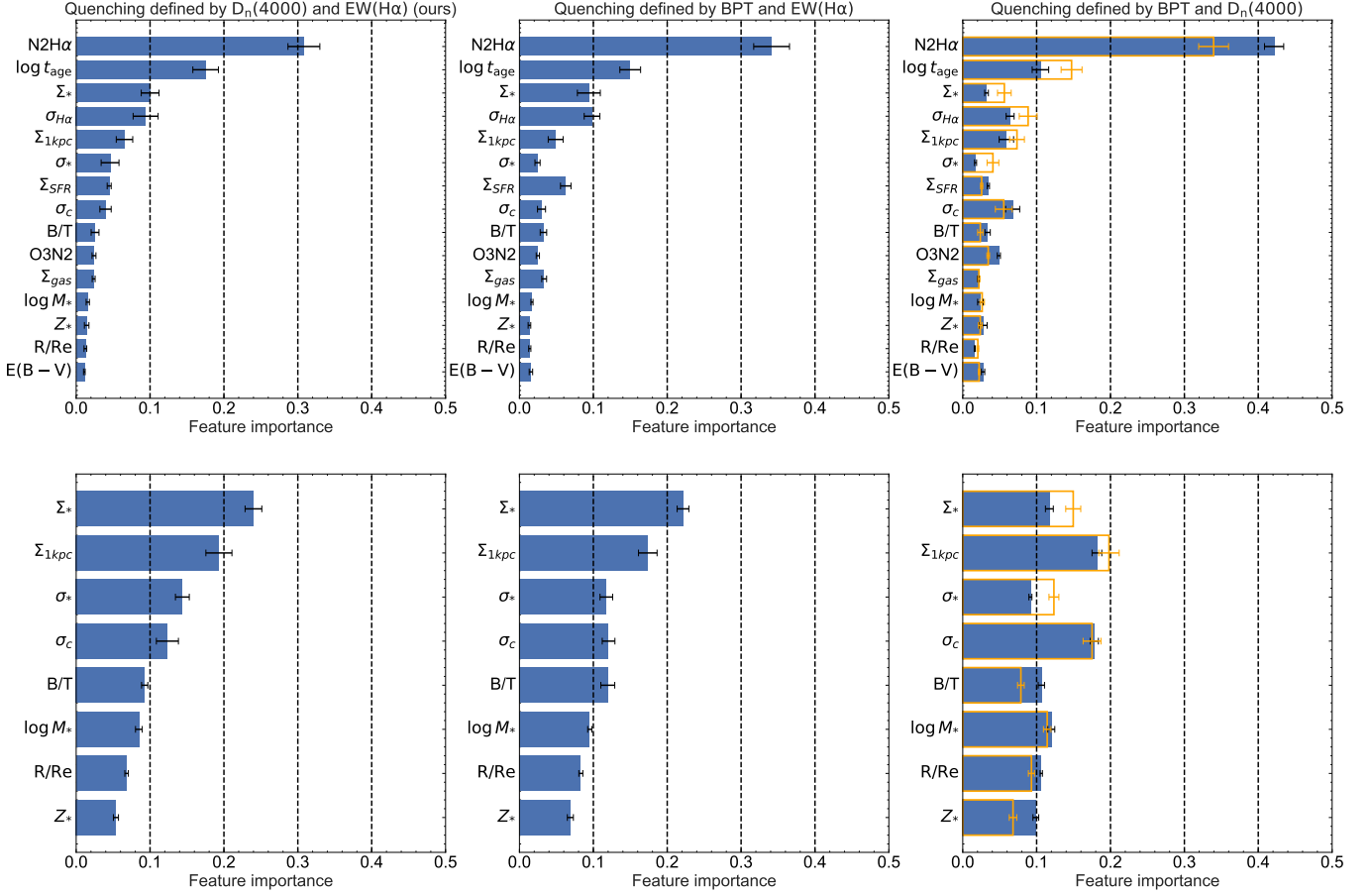


Figure 11. Gini feature importance provided by the random forest classifier for quenched regions defined in three different ways (panels from left to right): by $D_n(4000)$ and $EW(H\alpha)$ in this work, by BPT diagrams and $EW(H\alpha)$ following Lin et al. (2019b), and by BPT diagrams and $D_n(4000)$ following Bluck et al. (2020a,b). In the upper panels, the same set of properties as used in Figure 6 are included in the analysis here. For the lower panels, a subset of properties similar to those used in Bluck et al. (2020a,b) are included in the analysis. The properties are ordered by decreasing the feature importance as resulted from the samples in the leftmost panel. The orange empty histograms in the rightmost panels show the results when the criterion of $D_n(4000) > 1.6$ is adopted instead of $D_n(4000) > 1.45$.

attributed to quenching mechanisms varying in galaxies with different morphological types and in different components of late-type galaxies.

Nevertheless, within our sample, whether a $EW(H\alpha)$ cut is used in selecting quenched regions also leads to differing results, as we have previously demonstrated. As depicted in Figure 10, the sample defined following Bluck et al. (2020a,b) covers a larger parameter space than the sample defined following Lin et al. (2019b), indicating that the samples defined with $EW(H\alpha)$ are a subset of the sample defined by Bluck et al. (2020a,b). Therefore, the key to understanding the differences in quenching definitions lies in comprehending the physical origins of the regions with $EW(H\alpha) \geq 3 \text{ \AA}$ but satisfy the quenching definition based on the combination of the BPT diagram and $D_n(4000)$. We propose two possible scenarios for these regions. In one scenario, these regions are intrinsically quenched, and the high $EW(H\alpha)$ implies the presence of AGN ionization. Con-

sequently, the selection criteria with $EW(H\alpha)$ cut would exclude the AGN-related quenching regions, leading to a potentially underestimated importance of AGN indicators (e.g., σ_c and Σ_{1kpc}). In the other scenario, both AGN and OB stars contribute to the ionization of these regions. In this case, the selection criteria without the $EW(H\alpha)$ requirement essentially identify the correlation between AGN ionization tracer and other AGN tracers. Although the stellar population information is used to constrain the fraction of young stars ($D_n(4000)$ or spectral fitting-based Σ_{SFR}), if the star formation region is heavily obscured, the spectrum would be dominated by a less extinguished, older population. Neither the spectral index like $D_n(4000)$ nor the typical spectral fitting approach that uses a single attenuation curve for all star populations can efficiently capture the existence of newly formed stars. The hint is obtained by further subdividing the quenched regions selected based on $D_n(4000)$ and the BPT diagram by $EW(H\alpha)$. The sub-

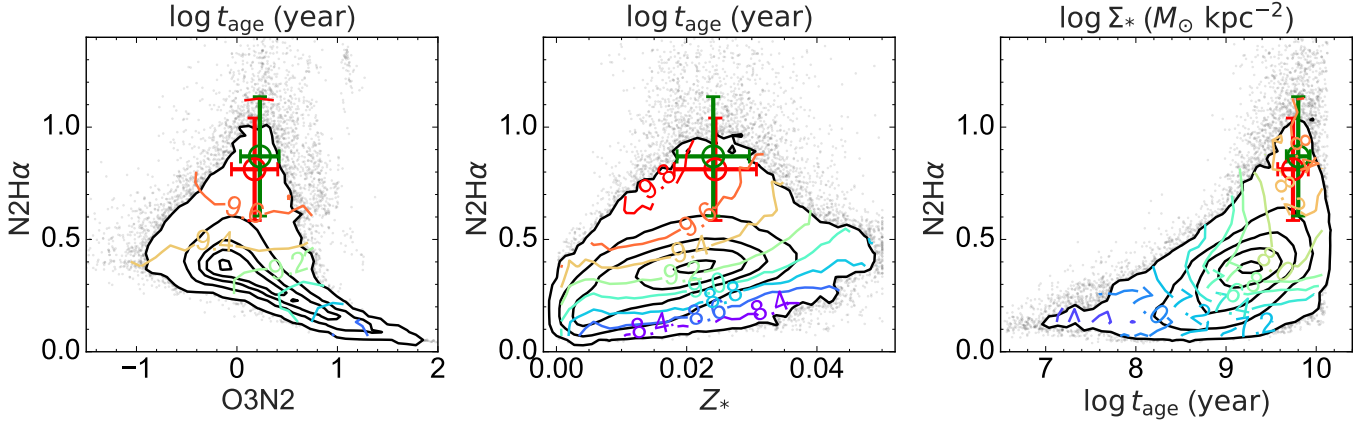


Figure 12. Each panel is a $N2H\alpha$ versus x-axis diagram. The x-axes are $O3N2$, Z_* , and $\log t_{\text{age}}$ from left to right. The meanings of black contours and dots are same as Figure 1. The mean value and 1σ scatter of GRQRs and GPQRs are shown as red and green circles with error bar, separately. In left and center panels, the colorful contours show the distribution of \log stellar age. In right panel, the colorful contours represent the $\log \Sigma_*$ distribution.

sample with $EW(H\alpha) \geq 3 \text{ \AA}$ has an overall lower $\sigma_{H\alpha}$ (33, 43, 55 km s^{-1} for the 25%, 50%, 75% quantiles) than the subsample with $EW(H\alpha) < 3 \text{ \AA}$ (43, 56, 72 km s^{-1}). This suggests that part of $H\alpha$ emission lines from these $EW(H\alpha) \geq 3 \text{ \AA}$ regions could be attributed to the gas embedded in the disk, possibly the star-forming region, as quenched regions and AGN-dominated regions tend to have higher $\sigma_{H\alpha}$ (Law et al. 2021; Sánchez et al. 2024). The actual situation may involve a combination of these two scenarios or be much more complex. It is also likely that $EW(H\alpha)$ -selected samples represent a later stage of the quenching process for a resolved region than the samples selected by the BPT diagram and $D_n(4000)$ alone. In this sense, both global quenching as traced by σ_c and $\Sigma_{1\text{kpc}}$ and local quenching as indicated by $N2H\alpha$, Σ_{gas} , and Σ_* can be at work, but at different stages, during the overall quenching process of the host galaxy. Since our sample can be considered a subset of the sample selected without the requirement of $EW(H\alpha)$, our findings suggest that AGN feedback cannot be deemed the sole quenching mechanism. We underscore the importance of carefully handling the regions with significant AGN features when selecting and studying quenching regions, as this can significantly impact the results. However, gaining a deeper understanding of this issue will require further efforts in the future.

3.5. Understanding the importance of $N2H\alpha$

The $[NII]$ -to- $H\alpha$ line ratio, $N2H\alpha$, is top ranked in the Gini feature importance analysis regardless of quenching definition (Figure 6 and Figure 11), and this parameter indeed shows a significant correlation with $D_n(4000)$ - $\log EW(H\alpha)$ as seen from Figure 7 and Figure 8. For the quenched regions defined by BPT diagrams but with no requirement on $H\alpha$ emission, the high importance of $N2H\alpha$ could be partly interpreted as a consequence of AGN-related ionization processes. However, for the

quenched regions defined by $EW(H\alpha)$ as in our work, an alternative explanation is necessary. In regions primarily ionized by OB stars, $N2H\alpha$ can serve as an indicator of gas phase metallicity (e.g. Pettini & Pagel 2004). Nevertheless, for quenched spaxels typically found in the LI(N)ER region of the BPT diagram and manifesting weak $H\alpha$ emission, the contribution of ionizing photons from low-mass evolved stars cannot be ignored (Binette et al. 1994; Stasińska et al. 2008; Sarzi et al. 2010; Yan & Blanton 2012; Papaderos et al. 2013; Singh et al. 2013; Sánchez et al. 2014; Belfiore et al. 2016; Gomes et al. 2016; Belfiore et al. 2017; Morisset et al. 2016; Rembold et al. 2017; Zhang et al. 2017). In this case, higher $N2H\alpha$ values indicate characteristics of the ionization source but not the metallicity. In the upper-left panel of Figure 12, we compare $N2H\alpha$ with other widely used gas-phase metallicity tracer $O3N2$. The majority of spaxels in the parent sample, enclosed by the 90% contour line, exhibit a narrow and tight relationship on this diagram, reflecting the predominance of star-forming regions in our sample. However, the quenched regions deviate from this relationship and extend to the highest $N2H\alpha$ region, corresponding to the spaxels with the highest average stellar age, as indicated by the colored contours. This demonstrates that, in the regions dominated by old population, $N2H\alpha$ and $O3N2$ no longer reliably represent gas-phase metallicity and lose their tight correlation. The center panel shows the correlation of $N2H\alpha$ with stellar metallicity. Similarly, the quenched regions are found to have intermediate metallicities, located outside the 90% contour line of the parent sample. The rightmost panel in the same figure displays the $N2H\alpha$ versus $\log t_{\text{age}}$ diagram, which shows again that the regions with highest $N2H\alpha$ have the oldest stellar populations. On the other hand, however, the regions of the highest stellar age span a full range of $N2H\alpha$. Thus, it is not necessary for regions with the highest

stellar age to also have the highest N2H α values, unless they have a relatively high value of Σ_* as shown by the colored contour lines. This result may be related to the fact that low mass evolved old stars are not as bright as massive main sequence stars. Given that the mass is primarily contributed by low-mass stars, a higher stellar mass density is needed to enable evolved stars to become the dominant ionizing source. The correlations between N2H α , t_{age} , $\sigma_{H\alpha}$, σ_* and the parameters we used for selecting quenching regions are well established in previous studies (Binette et al. 1994; Stasińska et al. 2008; Sarzi et al. 2010; Yan & Blanton 2012; Papaderos et al. 2013; Singh et al. 2013; Sánchez et al. 2014; Belfiore et al. 2016; Gomes et al. 2016; Belfiore et al. 2017; Zhang et al. 2017; Sánchez 2020; Sánchez et al. 2021a; Law et al. 2021; Sánchez et al. 2022, 2023a). The quenched regions tend to have higher values of N2H α , t_{age} , $\sigma_{H\alpha}$, σ_* and $D_n(4000)$, as well as lower EW(H α). The importance of N2H α , t_{age} , $\sigma_{H\alpha}$, and σ_* to quenching can be understood as a result of much more diffuse gas ionization by photons from substantially large amounts of low-mass evolved stars that typically have higher velocity dispersion. In this regard, the importance of these four parameters is correlated with each other and is a natural consequence rather than a cause of the quenching process.

4. DISCUSSION

4.1. Implications of the importance of Σ_*

The most striking result from our work is the high importance of Σ_* to quenching. This property appears to be not important at all as a single indicator. However, as illustrated in Figure 9, the combination of low Σ_{gas} and high Σ_* is not only sufficient but also necessary for indicating quenching. The regions identified by these two features are predominantly quenched, and quenched regions typically demonstrate the unique distribution of these two features. As discussed in subsection 3.3, the high Σ_* could result in lower f_{gas} and lower SFE simultaneously, making it the most important property for quenching, apart from the features that are considered as the outcome of quenching (as discussed in subsection 3.5), especially for GRQRs.

Previous studies have investigated the role of Σ_* on star formation instead of quenching, by examining the correlation of star formation rate (SFR) surface density Σ_{SFR} with the combination of Σ_{gas} and Σ_* . Both positive and negative effects have been found. For instance, Shi et al. (2011, 2018) found a power-law relation of $\Sigma_{\text{SFR}} \propto (\Sigma_*^{0.5} \Sigma_{\text{gas}})^{1.09}$, suggesting a positive role of Σ_* which may promote star formation by providing an additional local gravitational potential to help gas infall and condensation. Based on the ALMaQUEST sample with both integral field spectroscopy from MaNGA and CO intensity mapping from ALMA, Lin et al. (2019a) found Σ_* to present a negative effect on star formation, with a best-fit relation of $\Sigma_{\text{SFR}} \propto (\Sigma_*^{-0.3} \Sigma_{\text{H}_2})^{1.38}$. We have

performed the same analysis using our sample. Similar to Lin et al. (2019a), our star-forming subsample reveals a negative power exponent of -0.31 for Σ_* . The discrepancy between the MaNGA-based samples in Lin et al. (2019a) and our work and those in Shi et al. (2011, 2018) may be due to the different stellar mass ranges covered by the different samples, as pointed out by Lin et al. (2019a). It is important to note that, the relation proposed by Shi et al. (2011, 2018) outperforms the canonical Kennicutt-Schmidt relation primarily in the outer regions of dwarf galaxies characterized by low surface mass density or extremely metal-poor “gas-dominated” regions with gas fraction >0.5 (see Figure 2, 3, 4 in Shi et al. 2018). Conversely, our sample consists mainly of “star-dominated” regions with gas fraction <0.5 . These findings suggest that the net effect of existing stars for star formation may vary according to local properties, potentially being positive in low-mass, metal-poor, or gas-dominated regions, but negative in regions similar to those in this work and Lin et al. (2019a). Pessa et al. (2022) found that the power exponent of Σ_* can vary significantly across different local environments (not to be confused with the galaxy environment) and when defined at different scales. On a scale of approximately 100 pc, the power exponent is positive for regions in the disk, spiral arms, and the center of the galaxy, while it is negative for regions in the galaxy ring and bar. Using all spaxels from different environments to calibrate the correlation results in the power exponent being nearly zero and slightly negative. However, when the correlation is studied at a scale of 1000 pc, the power exponent for regions in different environments is similar. The power exponent defined by all spaxels will be close to -0.3, as found by this work and Lin et al. (2019a). This result implies that the effect of Σ_* is complex and could differ in different local environments and at different scales. It is important to note that the role of Σ_* in star-forming regions may not necessarily be the same as in quenched regions. As will be demonstrated below, the net effect of Σ_* is the result of a combination of multiple competing mechanisms. Therefore, the statistical net effect may vary with the physical properties of the region, the local environment, and the spatial scale.

4.2. Roles of existing evolved stars in quenching

As discussed above, the importance of Σ_* implies that existing low-mass stars play some positive roles for quenching, particularly for quenched regions with relatively large amounts of cold gas. In fact, existing stars can exert influence on surrounding gas in a number of different ways. The net effect on quenching is likely a combined result of different mechanisms. In this subsection we discuss on possible quenching mechanisms as driven by existing evolved stars.

4.2.1. Dynamical stabilization

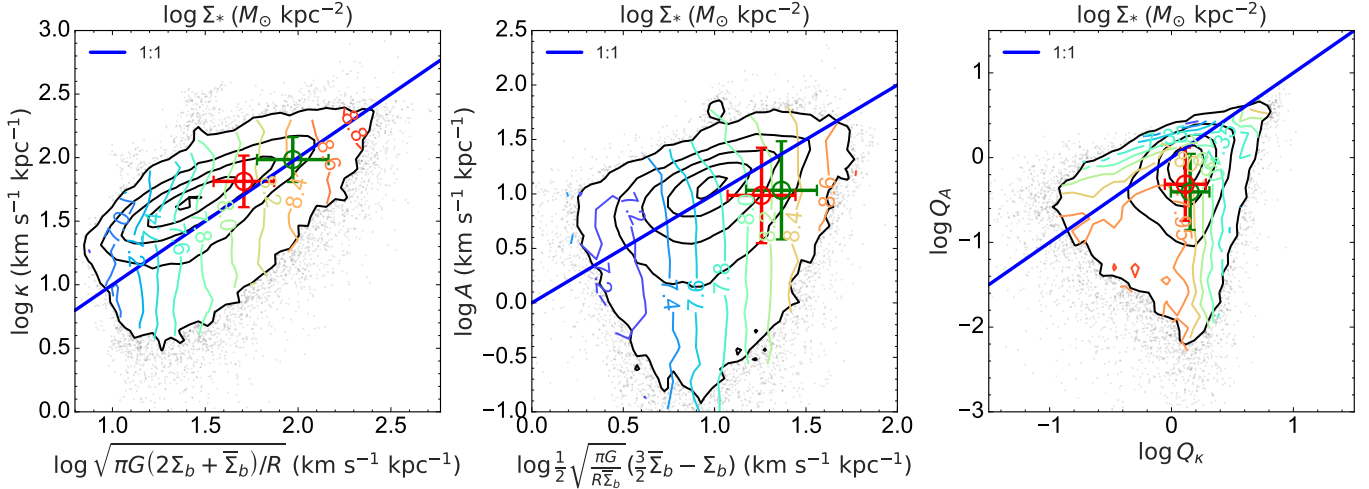


Figure 13. Left and center panels, the comparisons of estimates of κ (left panel) and A (center panel) with the values given by the relations in Equation 4 and Equation 5. For the x-axes of these two panels, we use $\Sigma_b = \Sigma_{\text{gas}} + \Sigma_*$ instead of Σ_m . The right panel illustrates the correlation between the Q value measured by κ and A . The 1:1 relationship is indicated by the blue line in each panel.

In a thin, differentially rotating disk as usually assumed in models of star formation, the potential for gas clouds to collapse is set by the competition between the self-gravity of the disc and the combined effect of thermal pressure, Coriolis forces and shear (e.g. Safronov 1960; Toomre 1964; Jog & Solomon 1984; Kennicutt 1989; Romeo 1992; Elmegreen & Parravano 1994; Wang & Silk 1994; Hunter et al. 1998; Tan 2000; Elmegreen 2011). The ability of a two-component disc with both gas and stars to stabilize itself through thermal pressure and Coriolis forces can be quantified by the modified version of the Toomre (1964) Q parameter as (Wang & Silk 1994):

$$Q = \left(\frac{1}{Q_{\text{gas}}} + \frac{1}{Q_*} \right)^{-1}. \quad (1)$$

Here, Q_{gas} and Q_* are the stability parameters for the gas and stellar components respectively, defined as

$$Q_{\text{gas}} = \frac{\kappa c_s}{\pi G \Sigma_{\text{gas}}}; \quad Q_* = \frac{\kappa \sigma_{r,*}}{\pi G \Sigma_*}, \quad (2)$$

where κ is the epicyclic frequency, c_s is the characteristic sound speed of 10^4 K gas, and $\sigma_{r,*}$ is the radial stellar velocity dispersion. In cases where the growth of gas clouds occurs with streaming motions along interstellar magnetic field lines or inner regions of galaxies with rising rotation curves, the Coriolis force can be less important and the formation of dense clouds may involve more of a competition with shear than with Coriolis forces, as proposed by Hunter et al. (1998). In this case, Hunter et al. (1998) estimated that the critical surface density for a perturbation to grow by a sufficiently large factor of ~ 100 is $\Sigma_{c,A} = (2.5A c_s)/(\pi G)$, where the Oort constant $A = 0.5(v/R - dv/dR)$ quantifies the local shear rate at galactic-centric radius R . Accordingly, the Q

parameters defined above can be rewritten by simply replacing κ by $2.5A$.

Therefore, on one hand, the existing stars can facilitate star formation through increasing Σ_* , hence decreasing Q_* . On the other hand, these stars may contribute to the competition with self-gravity to locally stabilize the disk against fragmentation, by influencing thermal pressure, Coriolis forces and shear as traced by $\sigma_{r,*}$, κ and A . For $\sigma_{r,*}$, the positive role of existing stars is evident given the positive correlation between stellar velocity dispersion and surface mass density (Stark et al. 2018, Eqn.6). However, the roles of existing stars for κ and A are not immediately clear. Given the rotation curve $v(R)$, i.e. the rotation velocity as a function of the galactic-centric radius R , one can obtain κ at given R by the definition:

$$\kappa(R) \equiv \sqrt{\frac{2v}{R} \frac{dv}{dR} + \frac{2v^2}{R^2}}. \quad (3)$$

For a simple case with circular rotation, $v(R)$ is simply scaled with the total mass within R as $v(R) \propto \sqrt{M(R)/R}$, and thus with the average surface mass density within R as $v(R) \propto \sqrt{R \bar{\Sigma}_m(R)}$, given the relation of $M(R) = \pi R^2 \bar{\Sigma}_m(R)$. One can easily find that the definition of κ is reduced to the following relation:

$$\kappa(r) = \left[\frac{\pi G}{R} (2\Sigma_m(R) + \bar{\Sigma}_m(R)) \right]^{1/2}. \quad (4)$$

This correlation indicates that the epicyclic frequency of the resolved region is positively correlated with the local mass surface density and the average surface density within the corresponding galactic-centric radius, while being negatively correlated with the radial distance from

the center of the galaxy. Similarly, one can also obtain the scaling relation for the Oort constant A from its definition as

$$A(R) = \frac{1}{2} \left[\frac{\pi G}{R \bar{\Sigma}_m(R)} \right]^{1/2} \left[\frac{3}{2} \bar{\Sigma}_m(R) - \Sigma_m(R) \right]. \quad (5)$$

Similar to κ , A also depends on both the local mass density and the average density within R , but in a more complicated way.

To better understand the role of Σ_* , we have estimated κ and A for each spaxel in our sample. Details of the estimation process can be found in Appendix A. In short, we firstly derive the rotation curve $v(R)$ for the host galaxies from the line-of-sight H α velocity maps, and then estimate both κ and A from $v(R)$ according to their definitions. In Figure 13, we compare the estimates of κ (left panel) and A (center panel) with the values given by the relations in Equation 4 and Equation 5. For the x-axes of these two panels, we use $\Sigma_b = \Sigma_{\text{gas}} + \Sigma_*$ instead of Σ_m , thus ignoring the contribution of dark matter which is not available from our data. Overall the distribution of all spaxels roughly follows the 1:1 relation in both panels, with systematic offsets and large scatters which should be attributed to the omission of dark matter and the oversimplified assumption of circular rotation in deducing the scaling relations, as well as the errors in the relevant measurements. The distribution of $\log \Sigma_*$ are shown as the colored contours. We see a trend for both κ and A to increase with Σ_* , indicating the positive correlation between existing stars and enhanced critical density. In the right panel of the same figure, we show the distribution of Q_A and Q_κ , the Q parameters defined above but calculated using κ and $2.5A$ respectively. The two stability parameters show reasonably strong correlation with each other, although with large scatter. The contours of $\log \Sigma_*$ clearly show that the spaxels with highest Σ_* are located in the “subcritical” regime defined by $Q_A < 1$ and $Q_\kappa < 1$. This result suggests that, although a high density of stars leads to increased values for both κ and A as shown in the left two panels, the net effect of these stars is to decrease the Q parameters, hence facilitating instability rather than suppressing it.

In addition, in Figure 13 the median locations of GPQRs and GRQRs are plotted as the red and green circles, with the error bars indicating the 1σ scatter of individual regions around the median. When compared to the parent sample, both types of quenched regions tend to have larger-than-average κ and A , implying again the positive role of κ and A for quenching. In the Q_A versus Q_κ diagram the quenched regions are located slightly below the peak of the parent sample, with $Q_A \lesssim 1$ (slightly smaller than average) and $Q_\kappa \gtrsim 1$ (just similar to average). This result implies that dynamical stabilization alone cannot fully drive the quenching of star formation in our galaxies, and that the high importance of Σ_* is

not pointing us to dynamical stabilization as the underlying mechanism for quenching.

Based on standard disk instability analysis and zoom-in simulation technique, Martig et al. (2009) proposed the scenario of “morphological quenching” that a prominent bulge, or more generally a centrally-concentrated mass distribution could stabilize the gas disk and quench star formation by sheared perturbations within the disk. Consequently, the galaxy could maintain weak or no star formation despite the presence of significant amounts of gas. In this case, the GRQRs studied in our work should be more commonly found in galaxies with a more concentrated morphology. However, we find the Sérsic index, concentration, Σ_{1kpc} , or B/T of the host galaxies of GRQRs are all similar to those of the host galaxies of GPQRs (see Figure 4). This is probably not unexpected because the concept of morphological quenching was initially proposed to understand the quenching in early-type galaxies, but not the spirals considered here.

4.2.2. Self-shielding of gas

In addition to forming stars by dynamical instability as discussed above, the gas should be able to shield itself from background ionizing radiation so that it can cool down, condense and form stars (Stecher & Williams 1967; Federman et al. 1979; de Jong et al. 1980; Glassgold et al. 1985; Franco & Cox 1986; Draine & Bertoldi 1996; Bertoldi & Draine 1996; Schaye 2004; Krumholz et al. 2009; Vázquez-Semadeni 2010; Krumholz 2012; Sternberg et al. 2014; Ballesteros-Paredes et al. 2020; Sternberg et al. 2021; Maillard et al. 2021). In such models, the ability for gas to self-shield is determined by the dust optical depth, τ , which can be estimated by (Stark et al. 2018)

$$\tau = \frac{\Sigma_{\text{gas}} Z_{\text{gas}}}{(\Sigma_{\text{gas}} Z_{\text{gas}})_{\text{ss}}}, \quad (6)$$

where Z_{gas} represents the gas-phase metallicity relative to solar, and $(\Sigma_{\text{gas}} Z_{\text{gas}})_{\text{ss}}$ is the dust optical depth above which the gas becomes self-shielded. We estimate τ for each spaxel in our sample, using our measurements of Σ_{gas} and $12+\log(\text{O}/\text{H})$ (the O3N2-based gas-phase metallicity calibrated by Marino et al. 2013) and following Stark et al. (2018) to calculate the metallicity-dependent $(\Sigma_{\text{gas}} Z_{\text{gas}})_{\text{ss}}$. We note that the O3N2 metallicity estimator is only reliable for regions primarily ionized by OB stars. It is appropriate for the majority of spaxels in our sample, providing a sufficient representation of the overall trend. Nevertheless, the derived metallicity of the quenched region may be unreliable. Although we present the measurements of the quenched region for comparison, it is important to understand the results with caution.

In Figure 14 (center column) we show the estimates of τ against R/R_e (first row) and Σ_* (second row) for all the spaxels in the parent sample, with the distribution

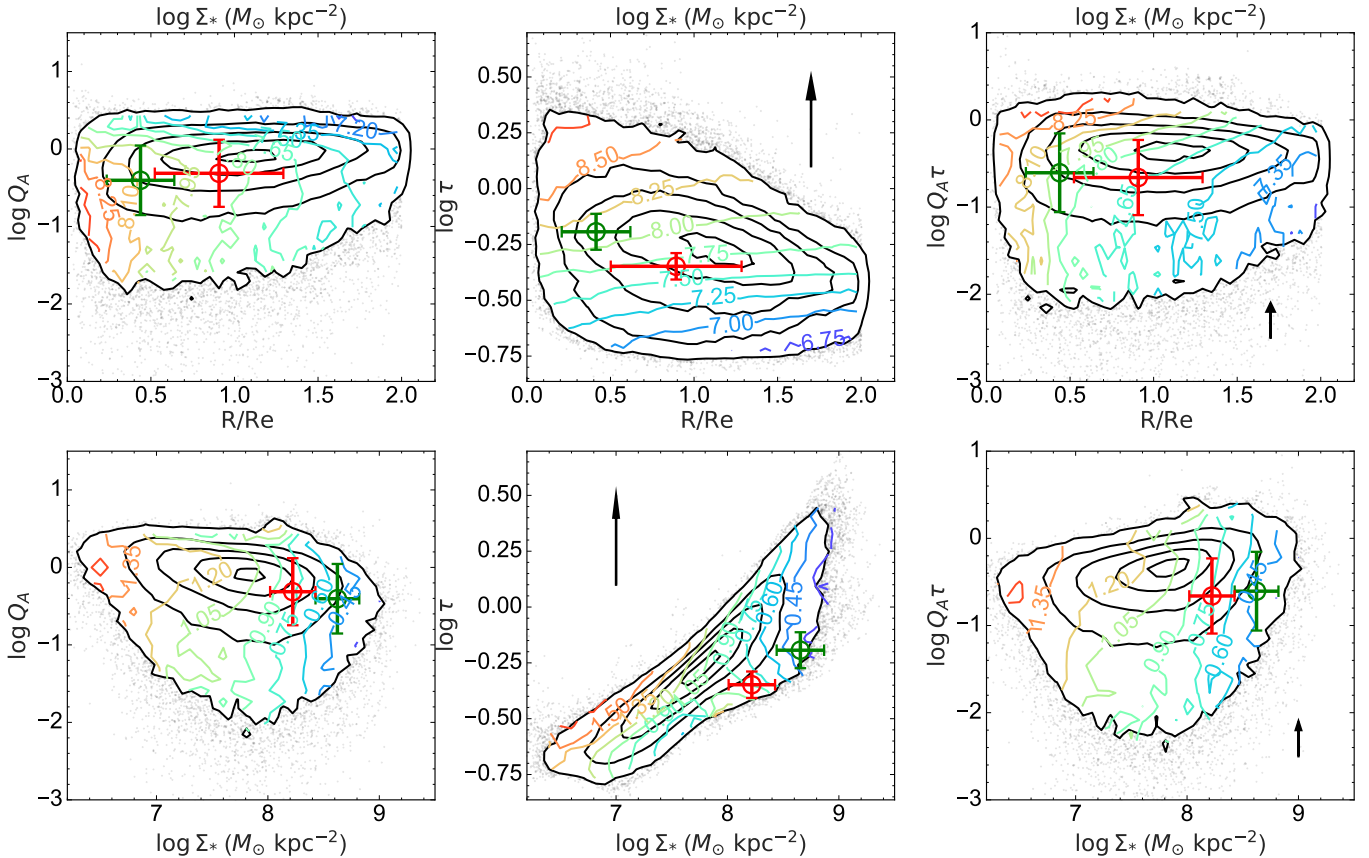


Figure 14. The upper panels (from left to right) display the radial profile of $\log Q_A$, $\log \tau$, and $\log Q_A \tau$, with the distribution of $\log \Sigma_*$ indicated by the colorful contours in each panel. The lower panels show the correlation of $\log Q_A$, $\log \tau$, and $\log Q_A \tau$ with $\log \Sigma_*$, with the distribution of R/R_e shown as colorful contours in each panel. The black arrows indicate the systematic shift of $\log \tau$ and $\log Q_A \tau$ when the N2O2 method instead of the O3N2 method is utilized to estimate Z_{gas} .

of Σ_* (first row) and R/R_e (second row) shown additionally as the colored contours. For comparison, the distribution of Q_A against R/R_e and Σ_* is shown in the left column of the same figure. We use Q_A rather than Q_κ for this figure considering that the rotation curves of our galaxies are still rising over the radial range covered by the spaxels in our sample (see Figure A16 for examples), but our conclusion would remain unchanged if Q_κ was instead used. In the right column we show the product, $Q_A \tau$ for the same samples. As suggested by Stark et al. (2018), the product of the Q parameter and τ can provide useful constraints on whether fragmentation or opacity is the underlying driver of star formation. In the center and right panels for each row, the vertical arrow indicates the average amount that τ or $Q_A \tau$ would increase if the N2O2 method was instead adopted to estimate Z_{gas} . In all the panels the median location and the scatter of the two quenched samples are indicated by the red and green circles with error bars.

The negative correlation of Q_A with Σ_* is seen again from the left column. For τ we see a positive correlation with Σ_* , which is expected from the known relation between gas-phase metallicity and stellar mass in star-

forming galaxies (Tremonti et al. 2004; Rosales-Ortega et al. 2012; Sánchez et al. 2013; Barrera-Ballesteros et al. 2016; Yao et al. 2022) and the molecular gas main sequence (Lin et al. 2019a). This relation suggests that the role of a high density of stars is mainly to indirectly enhance the opacity in the disk and thus make the gas more self-shielded. At the same time, we find that, although located at relatively small radii, the quenched regions including both GPQRs and GRQRs have similar values in Q_A , τ and $Q_A \tau$ to the average of the parent sample. This result essentially rules out both dynamical stabilization and unshielded gas as the driving mechanisms for quenching. Moreover, the high importance of Σ_* should be telling different mechanisms to what have been discussed so far.

4.2.3. Stellar feedback

Existing stars can provide energy or kinematic feedback to suppress star formation through radiation pressure, stellar wind and supernova explosion. We first consider radiation pressure which has long been proposed as an efficient feedback mechanism to suppress star formation (e.g. Elmegreen 1983; Thompson et al. 2005;

Faucher-Giguère et al. 2013; Raskutti et al. 2016). Previous studies have primarily focused on OB stars due to their high luminosity and ionizing photon production. Consequently, pressure regulation models (Ostriker & Shetty 2011; Kim et al. 2011) have linked the strength of radiation pressure to SFR rather than the local stellar mass density. Considering that the quenched regions are dominated by old stellar populations, here we consider the ability for the radiation pressure from evolved stars (such as red giants) to play some role in quenching. Following Raskutti et al. (2016), we consider a simple “gas shell” model in which the central star or star cluster is surrounded by a spherical gas shell. In this simple case, the gas shell feels both self-gravity and stellar gravity which facilitate gas collapse and star formation, as well as radiation pressure from the central star/cluster which supports the gas shell against collapse. The competition between gravitational force and radiation pressure can be quantified by the Eddington ratio ϵ_{Edd} , defined as the ratio of the pressure as caused by radiation and gravity, as follows:

$$\epsilon_{\text{Edd}} = \frac{2k_{\text{abs}}\Psi\Sigma_{*}}{\pi Gc\Sigma_{\text{gas}}(2\Sigma_{*} + \Sigma_{\text{gas}})}, \quad (7)$$

where k_{abs} is the fraction of stellar luminosity absorbed by the gas shell and Ψ is the mass-averaged luminosity-to-mass ratio. For a typical GRQR in our sample which has $\Sigma_{\text{gas}} \sim 2.5 \times 10^7 \text{ M}_{\odot}\text{kpc}^{-2}$ and $\Sigma_{*} \sim 3 \times 10^8 \text{ M}_{\odot}\text{kpc}^{-2}$, we estimate that

$$\epsilon_{\text{Edd}} \approx 0.06k_{\text{abs}}\frac{\Psi}{L_{\odot}/M_{\odot}}. \quad (8)$$

Considering a red giant with a mass of $1M_{\odot}$ and $\Psi \sim 100L_{\odot}/M_{\odot}$, we estimate that the Eddington ratio $\epsilon_{\text{edd}} \approx 6k_{\text{abs}}$. For the gas shell to be stable against gravity, we expect $\epsilon_{\text{Edd}} > 1$, which requires $k_{\text{abs}} \gtrsim 0.16$, i.e. about 1/6 or more of the luminosity radiated from the star/cluster is absorbed by the gas shell.

It is not straightforward to accurately calculate k_{abs} . On one hand, the cross-section of gas depends on a variety of factors including its ionization state, chemical composition, dynamical state, and metallicity. On the other hand, gas can indirectly feel the radiation pressure through the interaction with dust grains which gain momentum by absorbing photons. Here, we consider two extreme cases. In one case, gas feels radiation pressure only through Rayleigh scattering. Based on the interpolation formula provided by Dalgarno & Williams (1962), we estimate that $k_{\text{abs}} \approx 10^{-7}$, indicating that the gas hardly feels any radiation pressure. In the other case, all absorbed or scattered photons transmit their momentum to the gas. Under this assumption and using the observed $E(B - V)$ we estimate the k_{abs} in V band for each spaxels in our sample. For GRQRs, we find a median value of $k_{\text{abs}} \approx 0.8$, indicating that radiation feedback is highly efficient in preventing gas collapse.

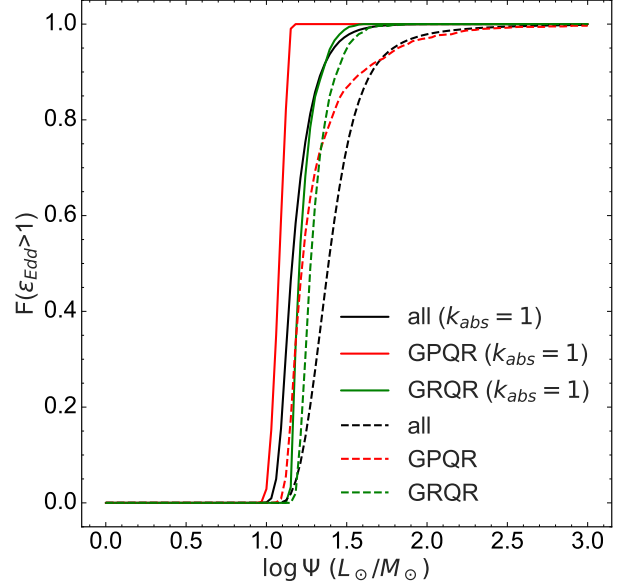


Figure 15. The $F(\epsilon_{\text{Edd}} > 1)$, the fraction of spaxels with $\epsilon_{\text{Edd}} > 1$, as a function of Ψ for the parent sample as well as the two types of quenched regions. The solid lines show the results obtained by assuming a fixed value of $k_{\text{abs}} = 1$, while the dashed lines show the results based on the estimates of k_{abs} as derived from $E(B - V)$.

The reality in GRQRs is likely closer to this case than the first case, as the interaction between gas and dust is ubiquitous, and gas can even freeze onto dust grains during the initial stages of gas collapse (Zhang et al. 2020). In fact, complete momentum transfer from dust to gas has been implemented in the FIRE simulation (Hopkins et al. 2018b).

Figure 15 shows $F(\epsilon_{\text{Edd}} > 1)$, the fraction of spaxels with $\epsilon_{\text{Edd}} > 1$, as a function of Ψ for the parent sample as well as the two types of quenched regions. The solid lines show the results obtained by assuming a fixed value of $k_{\text{abs}} = 1$. Since $k_{\text{abs}} = 1$ is the largest absorption fraction one can have, this case sets a lower limit of Ψ that is required for $F(\epsilon_{\text{Edd}} > 1)$ to reach a given value for a given sample. The dashed lines show the results based on the estimates of k_{abs} as derived above from $E(B - V)$. For all the samples and in both cases of k_{abs} , we see a sharp increase in $F(\epsilon_{\text{Edd}} > 1)$ when the luminosity-to-mass ratio of stars exceeds $\Psi \sim 10 - 20L_{\odot}/M_{\odot}$. When the estimated k_{abs} are used, the $F(\epsilon_{\text{Edd}} > 1)$ of the GRQR sample reaches $\sim 100\%$ at $\Psi \sim 50L_{\odot}/M_{\odot}$, which happens at $\Psi \gtrsim 300L_{\odot}/M_{\odot}$ for the other two samples. In other words, it seems that radiation pressure is more efficient, or more easy to take effect in GRQRs than in GPQRs. The significant enhancement of the Gini importance of σ_{*} , a characteristic of aged stars, for GRQRs (green bar in Figure 6) further supports the vital role of the old stellar population in GRQRs. This analysis confirms that radiation from the existing stars is able to

substantially support the gas against collapse, as long as their stellar luminosity-to-mass ratios are larger than a few $\times 10 L_{\odot}/M_{\odot}$. Considering that the lifetime of a solar mass red giant is approximately 1 billion years, which is comparable to or even longer than the main sequence lifetime of more massive stars, red giants represent a plausible source of radiation pressure that is needed here to compete with self-gravity of the gas shell. The presence of significant numbers of red giants naturally occurs in the quenched regions of our sample which are populated by high densities of old stars (see Figure 12). We strongly suggest the effect of radiation pressure from evolved stars, particularly red giants to be considered in future theoretical analyzes and hydrodynamical simulations of star formation.

Next, we consider stellar wind and supernova feedback. Stellar wind from massive OB stars and asymptotic giant branch (AGB) stars may eject dust and metal rich material to the ISM. This process releases energy and momentum, which can heat and expel surrounding gas. Similar to stellar wind, supernovae (SNe) can not only inject energy and momentum to heat or expel the surrounding gas, but also result in the mixing of metal rich material and gas, thereby enhancing the cooling efficiency of the gas (Su et al. 2019). Type Ia SNe exhibit a smooth distribution over time (Su et al. 2019), while type II SNe are associated with massive OB stars which should be less important in the quenched regions dominated by old populations. It is worth to note that both stellar wind and SN feedback can lead to higher N2H α and increased $\sigma_{\text{H}\alpha}$, and the effect is expected to be proportion to Σ_* . Thus, their contributions can not be simply ruled out. However, the wind from AGB stars is not highly efficient due to its low velocity, despite having a relatively high mass loss ratio. It becomes significant only when the adjacent gas exhibits a velocity dispersion greater than 300 km s^{-1} (Conroy et al. 2015). Given the relative low velocity dispersion measured in our sample, with $\sigma_{\text{H}\alpha} < 100 \text{ km s}^{-1}$ and $\sigma_* < 200 \text{ km s}^{-1}$ in most regions (see Figure 7), we can well expect the stellar wind to be inefficient in our case.

In order to estimate the effect of type Ia SN feedback in our sample, we utilize a model similar to that considered above for radiation pressure. The three forms of stellar feedback are similar in the sense that they transfer momentum and energy from the central star outwards, through photons (radiation pressure) or baryonic matter (stellar wind), or both (SN feedback). The effective Eddington ratio for type Ia SN feedback can be given by

$$\epsilon_{\text{SN}} = \frac{2P_{\text{SN}}\Sigma_*}{\pi G\Sigma_{\text{gas}}(2\Sigma_* + \Sigma_{\text{gas}})}, \quad (9)$$

where P_{SN} represents the momentum injected into the ISM per unit time per unit stellar mass. By employing the Type Ia SN feedback model as implemented in Hopkins et al. (2018b) and assuming that all momentum

released by Type Ia SNe can be coupled with the ISM, we obtain $P_{\text{SN}} \sim 6.3 \times 10^{-4} \text{ km/s/Myr}$. Considering the typical stellar and gas surface density of GRQRs, this yields $\epsilon_{\text{SN}} \approx 0.002$, suggesting a minor role of type Ia SN feedback in driving the quenching of GRQRs in our sample.

4.2.4. Other mechanisms

Previous studies have proposed some other quenching mechanisms, e.g. major mergers, violent disk instability and compaction quenching (efficient for gas-rich disk galaxies at high redshift), ram-pressure stripping and tidal stripping of gas (efficient for satellite galaxies orbiting in dark matter halos), active galactic nucleus feedback and virial shock heating (efficient for central galaxies in massive halos). As mentioned, we have removed interacting/merging galaxies from our sample, as well as those with misaligned H α distribution. In addition, the two types of quenched regions are shown to be hosted by non-AGN galaxies. Therefore, all the mechanisms listed above except gas stripping should not be important in our case. For gas stripping, previous studies have shown that this effect depends strongly on the surface mass density of galaxies, with high-density galaxies to be more capable of sustaining their gas against stripping (e.g. Li et al. 2012; Zhang et al. 2013). If gas stripping is at work for our galaxies, one would expect a negative role of Σ_* for quenching, which is opposite to our finding. In addition, Li et al. (2023) have recently identified from SDSS a unique but rare population of globally quenched HI-rich galaxies which are predominantly the central galaxies of relatively low-mass halos. The quenching of these galaxies was attributed to the low surface density of the HI disk as inferred from the extremely large HI-to-optical disk size ratios, which could be supported by high angular momentum inherited from the high spin of host dark matter halos (e.g. Lutz et al. 2018). This mechanism, advocated as ‘‘angular momentum quenching’’ by several authors (e.g. Obreschkow et al. 2016; Peng & Renzini 2020), is unlikely a plausible origin of the quenched regions in our sample which are mostly normal or even rich in terms of local gas density.

4.2.5. Summary of the subsection

To summarize, in this subsection we have discussed in depth the effect of dynamical stabilization, unshielded gas, and stellar feedback, which have been commonly considered in previous studies as plausible mechanisms for quenching. In particular, we have attempted to link the high density of stars as traced by Σ_* with these mechanisms, trying to understand the role of existing evolved stars. We conclude that both dynamical stabilization and unshielded gas are unlikely to play an important role, while radiation pressure from evolved stars (likely dominated by red giants) can be efficient in pro-

viding substantial support for the surrounding gas to be stable against gravitational collapse.

4.3. Limitations and outlook

This study is based on MaNGA data with an angular resolution of approximately $2''.5$, corresponding to ~ 2 kpc at $z = 0.04$, the redshift typical for MaNGA galaxies. This restricted resolution results in the point spread function (PSF) effect on the calculated $\Sigma_{1\text{kpc}}$. For a test on this issue, we have attempted to calculate an image-based $\Sigma_{1\text{kpc}}$ for each galaxy by applying the stellar mass-to-light ratio M_*/L versus $g - r$ color relation as calibrated in Du et al. (2019) to the SDSS images which have a typical resolution of $\sim 1''.4$. We find consistent measurements for $z \lesssim 0.02$, but at higher redshifts $\Sigma_{1\text{kpc}}$ from MaNGA is underestimated with respect to the SDSS images due to limited resolution, as expected. We have repeated the random forest analysis using the image-based $\Sigma_{1\text{kpc}}$ measurements and found our results remain unchanged. This implies that the feature importance ranking is robust to the uncertainties in $\Sigma_{1\text{kpc}}$. In addition, the limited resolution is also insufficient to resolve the star forming regions, thus the reported results should be regarded as the statistical average within approximately 2 kpc. The gas shell model assumed in our discussion is applicable for the scale of molecular clouds. The MaNGA resolution could blur the small-scale clumpiness, hence resulting in the underestimation of stellar/gas surface densities and gravitational potential. Conversely, the stellar/gas surface densities can also be overestimated, if multiple molecular clouds overlap along the same line of sight. It should be noted that not only the statistical results can vary with the resolution, as demonstrated by Pessa et al. (2022), but different mechanisms can also operate at different spatial scales. Further investigation into the origins of the quenched region and the role of existing stars in star formation requires observations with spatial resolution comparable to that of molecular cloud scales.

This work mainly focuses on the regions within the disk component of isolated late-type galaxies. It is currently unclear whether the results reported in this paper are applicable to other components of late-type galaxies and all types of galaxies. Therefore, the future study should be extended to encompass all components in all types of galaxies in order to determine if the results are dependent on the morphology of the host galaxy. Additionally, it will allow a comprehensive comparison with the findings reported in existing literature (e.g., Bluck et al. 2020a,b).

The measurement of Σ_{gas} is based on the estimator described in Appendix B. Although the test in Figure B18 shows that this estimator is unbiased on the key parameters included in the analysis, it still carries the potential risk of yielding artificial results. We have verified that the ranking of properties by random forest importance remains largely unchanged if we exclude Σ_{gas} from the

analysis. Additionally, we have attempted to reproduce the key plots (the right panel of Figure 1 and the second panel of Figure 9) of this work in the EDGE-CALIFA sample, the sample used to calibrate the estimator. We find that both the existence of two types of quenched regions and the location of these regions in the Σ_{gas} versus Σ_* diagram are consistent with those reported in this work. However, it is imperative to use a much improved gas estimator or CO-derived molecular gas in future work in order to quantitatively verify or correct the results obtained in this study.

The findings of this study suggest that the high Σ_* , as the most important property for quenching, could simultaneously contribute to the decrease of f_{gas} and SFE for quenched regions, especially for GRQRs. However, direct measurement of SFE in quenched regions is unattainable due to the contamination of ionization sources other than OB stars. Future research should employ a robust method to decompose the emission flux contributed by different sources, thus directly verifying the decrease of SFE with higher Σ_* as proposed in this study. Additionally, such a decomposition method could also benefit the further study of different quenching definitions and their effects on the obtained results, as discussed in subsection 3.4.

5. SUMMARY

In this work, we use a sample of isolated disk galaxies selected from the MaNGA survey to investigate the significance of local/global properties of galaxies to the cessation of star formation at kpc scales. We consider a total of 15 parameters, including both local properties for each of the resolved regions in MaNGA datacubes and the global properties for the host galaxies, as measured from the integral field spectroscopy data from MaNGA and multiwavelength observations from other surveys. We identify quenched regions by a single-parameter criterion $D_n(4000) - \log \text{EW}(\text{H}\alpha) > 1.6 - \log 2 = 1.3$, thus requiring the quenched regions as having no/weak star formation not only at the present day but also during the past 1-2 Gyr. We then divide the quenched regions into two subsamples according to the surface mass density of cold gas Σ_{gas} : gas-rich quenched regions (GRQRs) and gas-poor quenched regions (GPQRs). We first explore the global properties of the host galaxy of GRQRs and GPQRs. Subsequently, we utilize a random forest (RF) classifier to classify whether a resolved region is quenched or not given all the local/global properties, thus assessing the feature importance (FI) for each property. We then proceed to train RF regressors and classifiers to further evaluate the accuracy of different combinations of the properties in predicting the quenching parameter $D_n(4000) - \log \text{EW}(\text{H}\alpha)$ and quenching state. Finally, we examine the dependence of our results on quenching definition by repeating the analysis of feature importance with quenched regions defined following Lin et al. (2019b) and Bluck et al. (2020a,b).

Our conclusions can be summarized as follows.

1. The quenched regions including both GRQRs and GPQRs tend to be hosted by non-AGN galaxies with relatively high masses ($M_* \gtrsim 10^{10} M_\odot$) and red colors ($NUV - r \gtrsim 3$), as well as low SFR and high central density at fixed mass, but spanning wide ranges in other parameters that are similar to the parent sample. This implies that the conditions responsible for GRQRs are largely independent on the global properties of host galaxies.
2. N2H α is identified to be the most significant single parameter associated with quenching, regardless of how the quenched regions are defined. The importance of N2H α can be understood as a result of gas ionization by photons from substantially large amounts of old stars.
3. Σ_* is the most important property for quenching, especially for GRQRs, as long as a low EW(H α) is required for identifying quenched regions.
4. The difference in feature importance for quenching, as derived from our sample in comparison to those from the previous study by Bluck et al. (2020a,b), are partly caused by the different quenching definitions, specifically the different requirements on whether low EW(H α) is required for identifying a quenched region.

Understanding the origin of the ionization conditions of regions excluded by the EW(H α) cut is crucial for interpreting the different results obtained when requiring EW(H α) or not. It is currently unclear whether these regions are genuinely quenched or if they consist of star-forming regions contaminated by AGN. Since the quenched regions selected with the EW(H α) requirement represent a subset of those selected without this requirement, our findings suggest that AGN feedback alone cannot be regarded as the exclusive mechanism for quenching. This study underscores the importance of carefully treating regions with high EW(H α) when selecting and studying quenched regions. However, further investigation is necessary to shed more light on this issue.

We have discussed in depth the implications of our results on the origin of gas-rich quenched regions in our sample, particularly the role of existing evolved stars as indicated by the high importance of Σ_* . We consider three mechanisms: dynamical stabilization, unshielded gas, and stellar feedback, which have been commonly considered in previous studies. We conclude that both dynamical stabilization and unshielded gas are unlikely to play major roles in quenching, and radiation pressure from evolved stars (likely dominated by red giants) can

provide substantial support for the surrounding gas to be stable against gravitational collapse. Thus, the high Σ_* could contribute to the decreasing of f_{gas} and SFE at the same time, especially for GRQRs.

As indicated in subsection 4.3, this study has certain limitations. These include the limited spatial resolution of MaNGA, the exclusive focus on the disk component of isolated late-type galaxies, the measurement of Σ_{gas} by estimators, and the lack of decomposition of the emission line contributed by different ionization sources. The findings and proposed physical mechanisms in this study require further verification, revision, and development in future research.

ACKNOWLEDGEMENT

We are grateful to the anonymous referee for his/her comments which have helped us to improve this paper. This work is supported by the National Key R&D Program of China (grant NO. 2022YFA1602902), and the National Natural Science Foundation of China (grant Nos. 11821303, 11733002, 11973030, 11673015, 11733004, 11761131004, 11761141012).

Funding for the Sloan Digital Sky Survey IV has been provided by the Alfred P. Sloan Foundation, the U.S. Department of Energy Office of Science, and the Participating Institutions. SDSS-IV acknowledges support and resources from the Center for High-Performance Computing at the University of Utah. The SDSS web site is www.sdss.org.

SDSS-IV is managed by the Astrophysical Research Consortium for the Participating Institutions of the SDSS Collaboration including the Brazilian Participation Group, the Carnegie Institution for Science, Carnegie Mellon University, the Chilean Participation Group, the French Participation Group, Harvard-Smithsonian Center for Astrophysics, Instituto de Astrofísica de Canarias, The Johns Hopkins University, Kavli Institute for the Physics and Mathematics of the Universe (IPMU) / University of Tokyo, Lawrence Berkeley National Laboratory, Leibniz Institut für Astrophysik Potsdam (AIP), Max-Planck-Institut für Astronomie (MPIA Heidelberg), Max-Planck-Institut für Astrophysik (MPA Garching), Max-Planck-Institut für Extraterrestrische Physik (MPE), National Astronomical Observatories of China, New Mexico State University, New York University, University of Notre Dame, Observatório Nacional / MCTI, The Ohio State University, Pennsylvania State University, Shanghai Astronomical Observatory, United Kingdom Participation Group, Universidad Nacional Autónoma de México, University of Arizona, University of Colorado Boulder, University of Oxford, University of Portsmouth, University of Utah, University of Virginia, University of Washington, University of Wisconsin, Vanderbilt University, and Yale University.

APPENDIX

A. MEASURING DYNAMICAL PARAMETERS

For the analysis in [subsection 4.2.1](#), we have measured the epicyclic frequency κ and the Oort constant A , from which we calculate the corresponding Q parameters, Q_κ and Q_A . According to the definition of κ ([Equation 3](#)) and $A \equiv 0.5(v/R - dv/dR)$, both parameters include the local velocity gradient dv/dR . We obtain dv/dR in two different ways. In the first method, for a given spaxel at coordinate (R, θ) where R is the galactic-centric distance and θ is the position angle measured from the major axis of the host galaxy, we obtain its rotation velocity from the line-of-sight H α velocity $v_{\text{H}\alpha, \text{LOS}}$ by $v = v_{\text{H}\alpha, \text{LOS}}/(\cos\theta \sin i)$, with i being the inclination angle of the galactic disk given by the r -band minor-to-major axis ratio (b/a). The local velocity gradient is then estimated by

$$\frac{dv}{dR} = \frac{v_{\text{out}} - v_{\text{in}}}{\Delta R}, \quad (\text{A1})$$

where v_{in} is the rotation velocity of the spaxel in consideration, and v_{out} is the rotation velocity of spaxels located at $(R + \Delta R, \theta)$. The radial interval ΔR is chosen appropriately, depending on the inclination angle, position angle, and the R_e -normalized spatial resolution of the host galaxy. Specifically, we create a set of mock line-of-sight velocity maps for galaxies with the same inclination angle, position angle, and R_e -normalized spatial resolution as the galaxies for which we will determine ΔR . We employ a search algorithm to identify the ΔR that can reconstruct $\frac{dv}{dR}$ with the lowest mean-square-error, and subsequently apply this ΔR to real galaxies. Next, we estimate κ and A based on their definitions, utilizing the rotation velocity and local velocity gradient of each individual spaxel.

In the second method, we derive a rotation curve for the host galaxies, $v(R)$, defined as the average rotation velocity as a function of the galactic-centric distance R . For a host galaxy, we obtain $v(R)$ by fitting a functional form to the rotation velocities of all the spaxels with $\text{SNR} > 3$ in the galaxy as function of their radial distances. Two rotation curve models used in [Stark et al. \(2018\)](#) are considered here: $v(R) = v_{\text{flat}} [1 - e^{-R/l_{\text{flat}}}]$ and $v(R) = v_{\text{flat}} \tanh(R/h_{\text{rot}})$. We use both models to fit the data for a given galaxy and the one with a lower chi-square is adopted. Some examples of the rotation curve fits are shown in [Figure A16](#). From the best-fit rotation curves we then calculate κ and A for each spaxel in our sample, following the definition of the two parameters. In [Figure A17](#) we compare the two methods of deriving κ (left panel) and A (right panel), which are in good agreement. For the analysis in [subsection 4.2.1](#) we use the measurements from the first method, i.e. based on the local velocity gradients.

We then measure the modified [Toomre \(1964\)](#) Q parameter, Q_κ following the definition by [Wang & Silk \(1994\)](#), also see [Equation 1](#) and [Equation 2](#). For the characteristic sound speed c_s needed for calculating Q_{gas} , we adopt a fixed value of 15 km s^{-1} , which is the average velocity dispersion of ionized gas in the simulation of [Martig et al. \(2009\)](#). We note that a similar value of 13 km s^{-1} was adopted in [Stark et al. \(2018\)](#). We follow [Stark et al. \(2018\)](#), see their Eqn.6) to indirectly estimate the radial stellar velocity dispersion, $\sigma_{r,*}$, which is needed for calculating Q_* . The surface stellar mass densities (Σ_*) are measured from the MaNGA data, as described in [section 2](#). The surface gas mass densities (Σ_{gas}) are estimated using the method described below.

B. ESTIMATING GAS SURFACE DENSITIES

For the lack of spatial resolved CO and HI observations for our sample, we indirectly estimate the molecular and atomic gas surface densities, Σ_{H_2} and Σ_{HI} , and thus obtain the total gas density by $\Sigma_{\text{gas}} = \Sigma_{\text{H}_2} + \Sigma_{\text{HI}}$.

To estimate Σ_{H_2} , we have developed an estimator for $f_{\text{H}_2} \equiv \Sigma_{\text{H}_2}/(\Sigma_* + \Sigma_{\text{H}_2})$, based on four parameters that we have measured from the MaNGA data for our sample. These include the [NII]-to-H α flux ratio ($\text{N}2\text{H}\alpha$), the nebular dust attenuation $E(B-V)$, the surface stellar mass density Σ_* , and the equivalent width of the H α emission line $\text{EW}(\text{H}\alpha)$. We obtain and test the best-fit model of the estimator using data from the EDGE-CALIFA Survey ([Sánchez et al. 2012](#); [Walcher et al. 2014](#); [Sánchez et al. 2016](#); [Colombo et al. 2018](#)), which provides both MaNGA-like IFU data and resolved CO observations. We select a sample of spaxels following the selection of our MaNGA sample, and for each spaxel we perform spectral fitting in the same way as done for the MaNGA spectra (see [subsection 2.2](#)). Additionally, we require Σ_{H_2} to fall in the sensitive range of the EDGE survey, $4 - 110 \times 10^6 \text{ M}_\odot/\text{kpc}^2$ ([Barrera-Ballesteros et al. 2020](#)). The molecular gas mass is converted from the CO surface brightness, assuming a constant conversion factor $\alpha_{\text{CO}} = 4.4 \text{ M}_\odot (\text{K km s}^{-1} \text{ pc}^2)^{-1}$ ([Barrera-Ballesteros et al. 2020](#)). To obtain an estimator as accurate as possible, we take $\log(\text{N}2\text{H}\alpha)$, $E(B-V)$, $\log \Sigma_*$, and $\log \text{EW}(\text{H}\alpha)$, as well as their pairwise quadratic combinations as independent variables. Considering the different numerical ranges and dimensions, all the variables are standardized before fitting. We then fit the measurements of f_{H_2} from the EDGE-CALIFA sample by a linear combination of all the independent variables. We remove the variables with the best-fit coefficient less than 0.1 and perform the fitting again using the remaining variables. The best-fit coefficients as obtained from

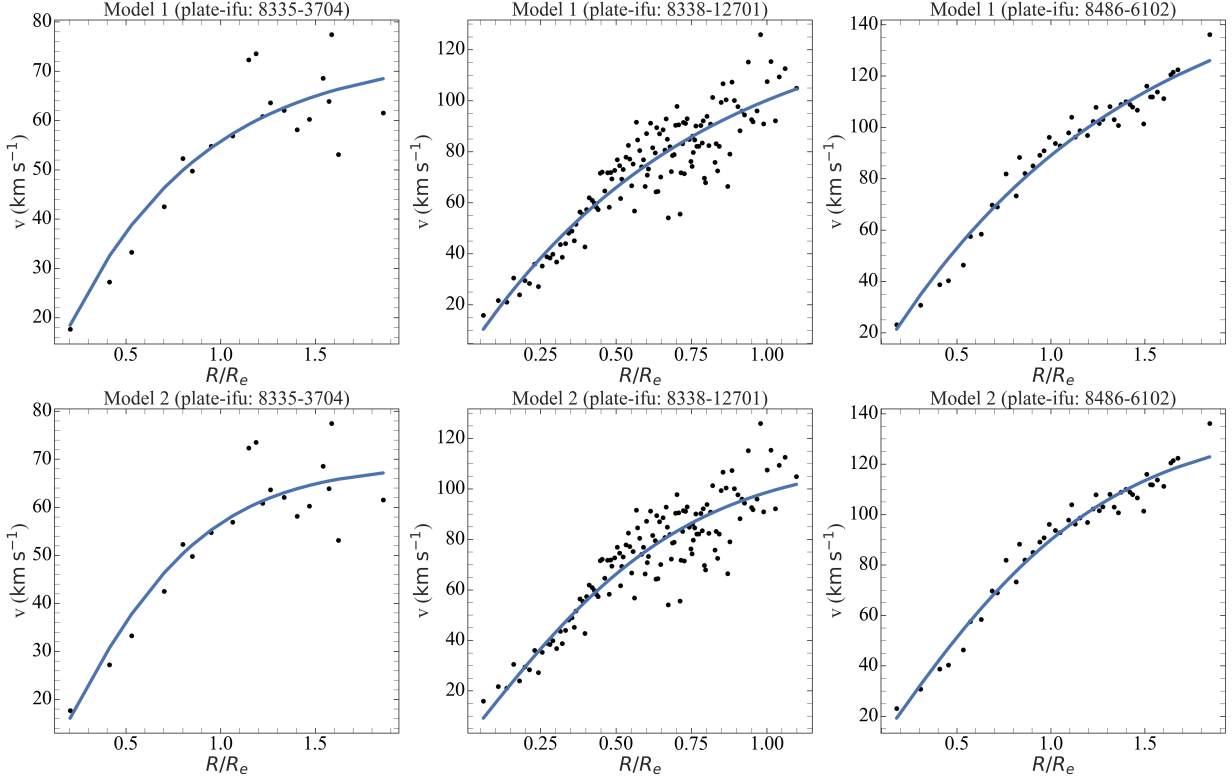


Figure A16. The examples of rotation curve fitting. Different columns represent randomly selected galaxies from our starting sample. The first row showcases the model $v(R) = v_{\text{flat}} [1 - e^{-R/l_{\text{flat}}}]$, while the second row presents the model $v(R) = v_{\text{flat}} \tanh(R/h_{\text{rot}})$. The black points in each panel denote every valid spaxel in the galaxy, with the blue curve representing the best-fitting result.

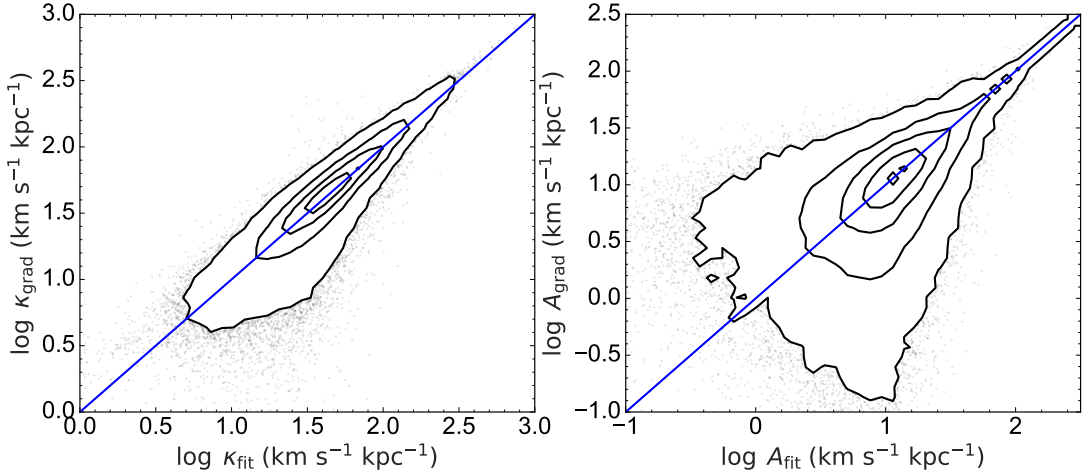


Figure A17. Consistency of κ and A obtained by rotation curve fitting and local gradient. The meanings of contours and black dots are same as Figure 1. The blue diagonal line in each panel shows 1:1 correlation.

the standardized variables are listed in Table 1, for the two fitting runs. We use the best-fit relation from the second run as our estimator, for which the coefficients for the original variables are also listed in Table 1. Figure B18 shows the residual of the predicted f_{H_2} by our estimator relative to the measurement from the EDGE-

CALIFA survey. The different panels compare the results for subsamples divided by different properties as indicated. As can be seen, in all cases the residual distributions are centered at zero with a scatter of about 0.26 dex, independent on the properties considered. This independence ensures our estimator will not lead to ar-

Table 1. The molecular gas mass surface density fraction fitting results

Variable	First Fit Coefficient	Second Fit Coefficient	Coefficient Converted Back to Original Variable
(1)	(2)	(3)	(4)
const	-0.8697	-0.8697	7.52670997
log EW(H α)	-0.4576	-0.4841	-1.23631778
log Σ_*	-0.6681	-0.6885	-1.44821091
E(B - V)	-0.1276	-0.0905	-0.28691643
log N2H α	0.1271	0.103	0.69222
[log EW(H α)] ²	0.0118	-	-
log EW(H α) · log Σ_*	0.5035	0.5448	0.18309026
log EW(H α) · E(B - V)	0.0121	-	-
log EW(H α) · log N2H α	0.0021	-	-
(log Σ_*) ²	0.3278	0.3509	0.04597756
log Σ_* · E(B - V)	0.1493	0.1029	0.03949803
log Σ_* · log N2H α	-0.1086	-0.0817	-0.07043908
[E(B - V)] ²	-0.0182	-	-
E(B - V) · log N2H α	0.0025	-	-
[log N2H α] ²	-0.0017	-	-

tificial results at least in first order. This estimator is applied to the MaNGA data to estimate Σ_{H_2} for each of the spaxels in our sample.

To estimate Σ_{HI} , we consider three different methods. Firstly, we estimate a radial profile of HI surface mass for each galaxy in our sample, using the HI size-mass relation and average HI surface mass profiles provided by Wang et al. (2016, 2020). For this we use the total HI mass of our galaxies available from the HI-MaNGA data release 2 (Masters & Stark 2019). Secondly, we estimate the HI mass density using the average Σ_* - Σ_{HI} relation found by Morselli et al. (2020). Thirdly, for all the spaxels we simply assume a constant value of

$\Sigma_{\text{HI}} = 6 \times 10^6 \text{ M}_\odot \text{ kpc}^{-2}$ (Barrera-Ballesteros et al. 2020). We have tried with all the three methods, finding no significant differences in the estimated total gas mass density Σ_{gas} measurement. This finding is shown in Figure B19. We notice that some spaxels substantially deviate from the 1 : 1 relation, and we find the majority of these spaxels are hosted by low mass galaxies with $M_* < 10^{10} \text{ M}_\odot$. This is not an important issue for our work. As shown in Figure 4, the quenched regions in our sample are mostly hosted by high mass galaxies with $M_* \gtrsim 10^{10} \text{ M}_\odot$. Therefore, for simplicity we set Σ_{HI} as a constant of $6 \times 10^6 \text{ M}_\odot \text{ kpc}^{-2}$ throughout this work.

REFERENCES

- Abadi, M. G., Moore, B., & Bower, R. G. 1999, MNRAS, 308, 947, doi: [10.1046/j.1365-8711.1999.02715.x](https://doi.org/10.1046/j.1365-8711.1999.02715.x)
- Abdurro'uf, Accetta, K., Aerts, C., et al. 2022, ApJS, 259, 35, doi: [10.3847/1538-4365/ac4414](https://doi.org/10.3847/1538-4365/ac4414)
- Bacon, R., Copin, Y., Monnet, G., et al. 2001, MNRAS, 326, 23, doi: [10.1046/j.1365-8711.2001.04612.x](https://doi.org/10.1046/j.1365-8711.2001.04612.x)
- Baker, W. M., Maiolino, R., Bluck, A. F. L., et al. 2022, MNRAS, 510, 3622, doi: [10.1093/mnras/stab3672](https://doi.org/10.1093/mnras/stab3672)
- Baldwin, J. A., Phillips, M. M., & Terlevich, R. 1981, PASP, 93, 5, doi: [10.1086/130766](https://doi.org/10.1086/130766)
- Ballesteros-Paredes, J., André, P., Hennebelle, P., et al. 2020, SSRv, 216, 76, doi: [10.1007/s11214-020-00698-3](https://doi.org/10.1007/s11214-020-00698-3)
- Balogh, M. L., Morris, S. L., Yee, H. K. C., Carlberg, R. G., & Ellingson, E. 1999, ApJ, 527, 54, doi: [10.1086/308056](https://doi.org/10.1086/308056)
- Balogh, M. L., Navarro, J. F., & Morris, S. L. 2000, ApJ, 540, 113, doi: [10.1086/309323](https://doi.org/10.1086/309323)
- Bamford, S. P., Nichol, R. C., Baldry, I. K., et al. 2009, MNRAS, 393, 1324, doi: [10.1111/j.1365-2966.2008.14252.x](https://doi.org/10.1111/j.1365-2966.2008.14252.x)
- Barnes, J. E., & Hernquist, L. E. 1991, ApJL, 370, L65, doi: [10.1086/185978](https://doi.org/10.1086/185978)

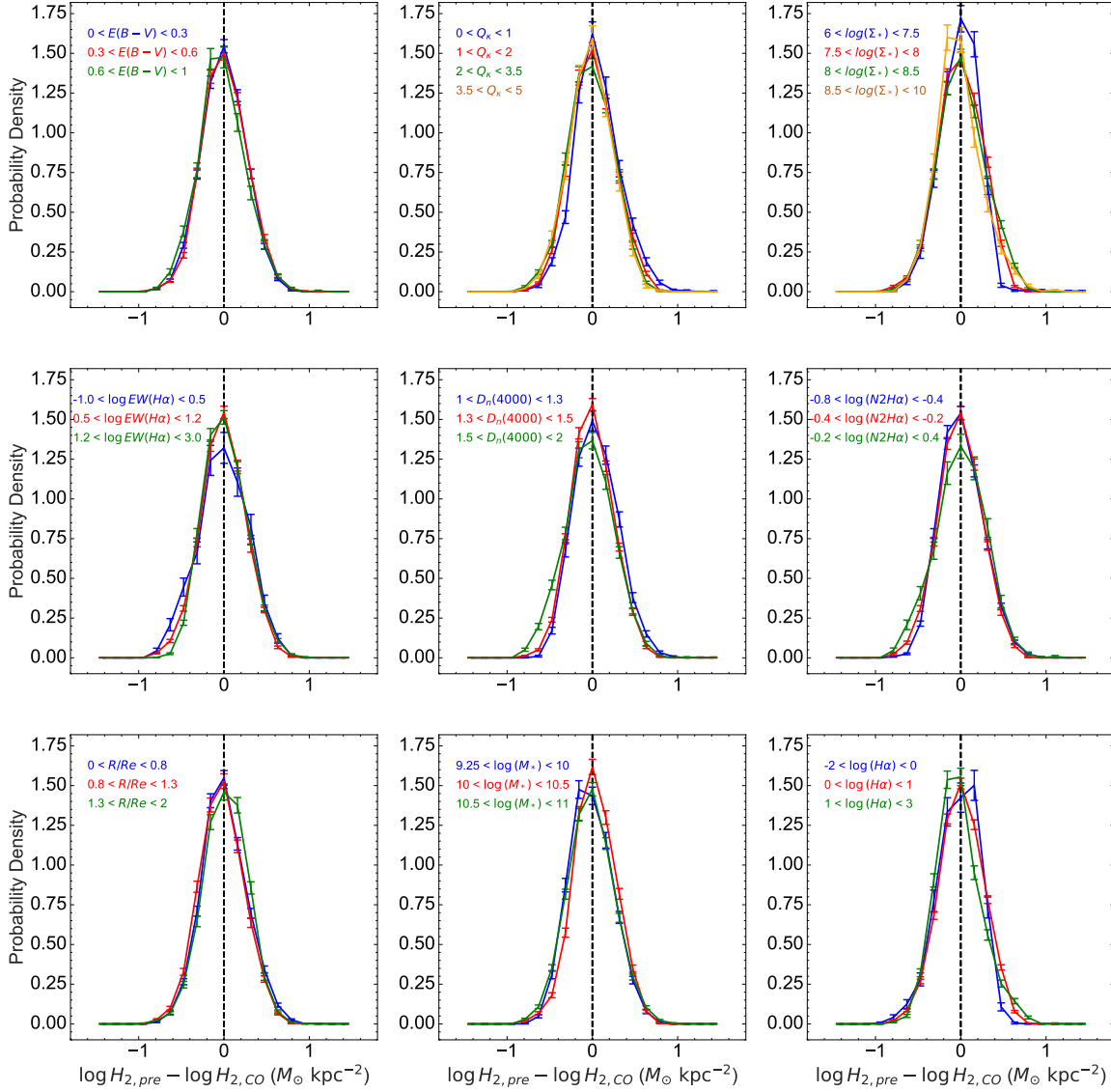


Figure B18. No bias of molecular gas estimator on parameters used in analysis. Different panels show the probability density distribution of residual ($\log \Sigma_{H2,pre} - \log \Sigma_{H2,CO}$) in different bins (represented by different colors) of different parameters. The parameters shown in first row are $E(B-V)$, Q_κ and Σ_* . The parameters in second row are $EW(H\alpha)$, $D_n(4000)$ and $N2H\alpha$. The parameters in third row are radius, galaxy mass and corrected $H\alpha$ flux. The vertical line in each panel locates at zero residual as a reference. The error bar shows 1σ uncertainty. The $\sigma_{\tau,*}$ used to calculate Q_κ is approximated by line-of-sight σ_* in this figure. All the test data used here are obtained from EDGE-CALIFA sample.

Barrera-Ballesteros, J. K., Heckman, T. M., Zhu, G. B., et al. 2016, MNRAS, 463, 2513, doi: [10.1093/mnras/stw1984](https://doi.org/10.1093/mnras/stw1984)

Barrera-Ballesteros, J. K., Utomo, D., Bolatto, A. D., et al. 2020, MNRAS, 492, 2651, doi: [10.1093/mnras/stz3553](https://doi.org/10.1093/mnras/stz3553)

Barrera-Ballesteros, J. K., Heckman, T., Sánchez, S. F., et al. 2021, ApJ, 909, 131, doi: [10.3847/1538-4357/abd855](https://doi.org/10.3847/1538-4357/abd855)

Barro, G., Faber, S. M., Koo, D. C., et al. 2017, ApJ, 840, 47, doi: [10.3847/1538-4357/aa6b05](https://doi.org/10.3847/1538-4357/aa6b05)

Bekki, K. 2014, MNRAS, 438, 444, doi: [10.1093/mnras/stt2216](https://doi.org/10.1093/mnras/stt2216)

Belfiore, F., Maiolino, R., Maraston, C., et al. 2016, MNRAS, 461, 3111, doi: [10.1093/mnras/stw1234](https://doi.org/10.1093/mnras/stw1234)

—. 2017, MNRAS, 466, 2570, doi: [10.1093/mnras/stw3211](https://doi.org/10.1093/mnras/stw3211)

Belfiore, F., Westfall, K. B., Schaefer, A., et al. 2019, AJ, 158, 160, doi: [10.3847/1538-3881/ab3e4e](https://doi.org/10.3847/1538-3881/ab3e4e)

Bell, E. F. 2008, ApJ, 682, 355, doi: [10.1086/589551](https://doi.org/10.1086/589551)

Bell, E. F., McIntosh, D. H., Barden, M., et al. 2004, ApJL, 600, L11, doi: [10.1086/381388](https://doi.org/10.1086/381388)

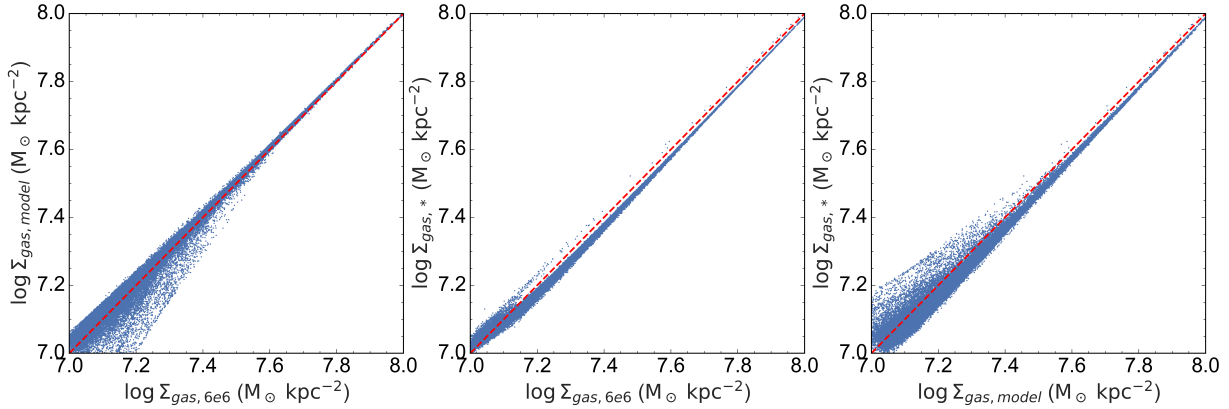


Figure B19. Consistency of total gas mass surface density in our sample by using different HI estimators. The three panels from left to right show the pairwise comparison of the following three estimators: the fixed value at $6 \times 10^6 M_{\odot}/\text{kpc}^2$ ($\Sigma_{\text{gas},6e6}$), Wang et al. (2016)’s model ($\Sigma_{\text{gas},\text{model}}$) and stellar mass surface density-HI mass surface density relationship found by Morselli et al. (2020) ($\Sigma_{\text{gas},\text{stellar}}$). The blue dots in three panels are spaxels on which we use different HI estimators to obtain their total gas mass surface density. The diagonal red dash lines in these panels show 1:1 correlation.

Bershady, M. A., Verheijen, M. A. W., Swaters, R. A., et al.

2010, *ApJ*, 716, 198, doi: [10.1088/0004-637X/716/1/198](https://doi.org/10.1088/0004-637X/716/1/198)

Bertoldi, F., & Draine, B. T. 1996, *ApJ*, 458, 222,

doi: [10.1086/176805](https://doi.org/10.1086/176805)

Bigieli, F., Leroy, A., Walter, F., et al. 2008, *AJ*, 136, 2846,

doi: [10.1088/0004-6256/136/6/2846](https://doi.org/10.1088/0004-6256/136/6/2846)

Binette, L., Magris, C. G., Stasińska, G., & Bruzual, A. G.

1994, *A&A*, 292, 13

Birnboim, Y., & Dekel, A. 2003, *MNRAS*, 345, 349,

doi: [10.1046/j.1365-8711.2003.06955.x](https://doi.org/10.1046/j.1365-8711.2003.06955.x)

Birnboim, Y., Dekel, A., & Neistein, E. 2007, *MNRAS*, 380,

339, doi: [10.1111/j.1365-2966.2007.12074.x](https://doi.org/10.1111/j.1365-2966.2007.12074.x)

Blanc, G. A., Weinzirl, T., Song, M., et al. 2013, *AJ*, 145,

138, doi: [10.1088/0004-6256/145/5/138](https://doi.org/10.1088/0004-6256/145/5/138)

Blanton, M. R., Kazin, E., Muna, D., Weaver, B. A., &

Price-Whelan, A. 2011, *AJ*, 142, 31,

doi: [10.1088/0004-6256/142/1/31](https://doi.org/10.1088/0004-6256/142/1/31)

Blanton, M. R., Bershady, M. A., Abolfathi, B., et al. 2017,

AJ, 154, 28, doi: [10.3847/1538-3881/aa7567](https://doi.org/10.3847/1538-3881/aa7567)

Blitz, L., & Rosolowsky, E. 2004, *ApJL*, 612, L29,

doi: [10.1086/424661](https://doi.org/10.1086/424661)

—. 2006, *ApJ*, 650, 933, doi: [10.1086/505417](https://doi.org/10.1086/505417)

Bluck, A. F. L., Maiolino, R., Sánchez, S. F., et al. 2020a,

MNRAS, 492, 96, doi: [10.1093/mnras/stz3264](https://doi.org/10.1093/mnras/stz3264)

Bluck, A. F. L., Mendel, J. T., Ellison, S. L., et al. 2014,

MNRAS, 441, 599, doi: [10.1093/mnras/stu594](https://doi.org/10.1093/mnras/stu594)

Bluck, A. F. L., Maiolino, R., Piotrowska, J. M., et al.

2020b, *MNRAS*, 499, 230, doi: [10.1093/mnras/staa2806](https://doi.org/10.1093/mnras/staa2806)

Blumenthal, G. R., Faber, S. M., Primack, J. R., & Rees,

M. J. 1984, *Nature*, 311, 517, doi: [10.1038/311517a0](https://doi.org/10.1038/311517a0)

Bolatto, A. D., Wong, T., Utomo, D., et al. 2017, *ApJ*, 846,

159, doi: [10.3847/1538-4357/aa86aa](https://doi.org/10.3847/1538-4357/aa86aa)

Bower, R. G., Benson, A. J., Malbon, R., et al. 2006,

MNRAS, 370, 645, doi: [10.1111/j.1365-2966.2006.10519.x](https://doi.org/10.1111/j.1365-2966.2006.10519.x)

Bower, R. G., McCarthy, I. G., & Benson, A. J. 2008,

MNRAS, 390, 1399,

doi: [10.1111/j.1365-2966.2008.13869.x](https://doi.org/10.1111/j.1365-2966.2008.13869.x)

Brinchmann, J., Charlot, S., White, S. D. M., et al. 2004,

MNRAS, 351, 1151,

doi: [10.1111/j.1365-2966.2004.07881.x](https://doi.org/10.1111/j.1365-2966.2004.07881.x)

Brodie, J. P., Romanowsky, A. J., Strader, J., et al. 2014,

ApJ, 796, 52, doi: [10.1088/0004-637X/796/1/52](https://doi.org/10.1088/0004-637X/796/1/52)

Bryant, J. J., Owers, M. S., Robotham, A. S. G., et al.

2015, *MNRAS*, 447, 2857, doi: [10.1093/mnras/stu2635](https://doi.org/10.1093/mnras/stu2635)

Bundy, K., Ellis, R. S., Conselice, C. J., et al. 2006, *ApJ*,

651, 120, doi: [10.1086/507456](https://doi.org/10.1086/507456)

Bundy, K., Scarlata, C., Carollo, C. M., et al. 2010, *ApJ*,

719, 1969, doi: [10.1088/0004-637X/719/2/1969](https://doi.org/10.1088/0004-637X/719/2/1969)

Bundy, K., Bershady, M. A., Law, D. R., et al. 2015, *ApJ*,

798, 7, doi: [10.1088/0004-637X/798/1/7](https://doi.org/10.1088/0004-637X/798/1/7)

Cappellari, M., Emsellem, E., Krajnović, D., et al. 2011,

MNRAS, 416, 1680,

doi: [10.1111/j.1365-2966.2011.18600.x](https://doi.org/10.1111/j.1365-2966.2011.18600.x)

Cattaneo, A., Dekel, A., Devriendt, J., Guiderdoni, B., &

Blaizot, J. 2006, *MNRAS*, 370, 1651,

doi: [10.1111/j.1365-2966.2006.10608.x](https://doi.org/10.1111/j.1365-2966.2006.10608.x)

Cattaneo, A., Dekel, A., Faber, S. M., & Guiderdoni, B.

2008, *MNRAS*, 389, 567,

doi: [10.1111/j.1365-2966.2008.13562.x](https://doi.org/10.1111/j.1365-2966.2008.13562.x)

Ceverino, D., & Klypin, A. 2009, *ApJ*, 695, 292,

doi: [10.1088/0004-637X/695/1/292](https://doi.org/10.1088/0004-637X/695/1/292)

Chabrier, G. 2003, *PASP*, 115, 763, doi: [10.1086/376392](https://doi.org/10.1086/376392)

Chen, Y.-M., Shi, Y., Wild, V., et al. 2019, *MNRAS*, 489,

5709, doi: [10.1093/mnras/stz2494](https://doi.org/10.1093/mnras/stz2494)

- Cheung, E., Faber, S. M., Koo, D. C., et al. 2012, *ApJ*, 760, 131, doi: [10.1088/0004-637X/760/2/131](https://doi.org/10.1088/0004-637X/760/2/131)
- Chung, A., van Gorkom, J. H., Kenney, J. D. P., Crowl, H., & Vollmer, B. 2009, *AJ*, 138, 1741, doi: [10.1088/0004-6256/138/6/1741](https://doi.org/10.1088/0004-6256/138/6/1741)
- Cid Fernandes, R., Stasińska, G., Mateus, A., & Vale Asari, N. 2011, *MNRAS*, 413, 1687, doi: [10.1111/j.1365-2966.2011.18244.x](https://doi.org/10.1111/j.1365-2966.2011.18244.x)
- Cid Fernandes, R., Stasińska, G., Schlickmann, M. S., et al. 2010, *MNRAS*, 403, 1036, doi: [10.1111/j.1365-2966.2009.16185.x](https://doi.org/10.1111/j.1365-2966.2009.16185.x)
- Colombo, D., Kalinova, V., Utomo, D., et al. 2018, *MNRAS*, 475, 1791, doi: [10.1093/mnras/stx3233](https://doi.org/10.1093/mnras/stx3233)
- Colombo, D., Sanchez, S. F., Bolatto, A. D., et al. 2020, *A&A*, 644, A97, doi: [10.1051/0004-6361/202039005](https://doi.org/10.1051/0004-6361/202039005)
- Conroy, C., van Dokkum, P. G., & Kravtsov, A. 2015, *ApJ*, 803, 77, doi: [10.1088/0004-637X/803/2/77](https://doi.org/10.1088/0004-637X/803/2/77)
- Cox, D. P., & Smith, B. W. 1974, *ApJL*, 189, L105, doi: [10.1086/181476](https://doi.org/10.1086/181476)
- Croom, S. M., Lawrence, J. S., Bland-Hawthorn, J., et al. 2012, *MNRAS*, 421, 872, doi: [10.1111/j.1365-2966.2011.20365.x](https://doi.org/10.1111/j.1365-2966.2011.20365.x)
- Croton, D. J., Springel, V., White, S. D. M., et al. 2006, *MNRAS*, 365, 11, doi: [10.1111/j.1365-2966.2005.09675.x](https://doi.org/10.1111/j.1365-2966.2005.09675.x)
- Cui, J., Gu, Q., & Shi, Y. 2024, *MNRAS*, doi: [10.1093/mnras/stae156](https://doi.org/10.1093/mnras/stae156)
- Dalgarno, A., & Williams, D. A. 1962, *ApJ*, 136, 690, doi: [10.1086/147428](https://doi.org/10.1086/147428)
- Davies, L. J. M., Robotham, A. S. G., Lagos, C. d. P., et al. 2019, *MNRAS*, 483, 5444, doi: [10.1093/mnras/sty3393](https://doi.org/10.1093/mnras/sty3393)
- Davis, T. A., Rowlands, K., Allison, J. R., et al. 2015, *MNRAS*, 449, 3503, doi: [10.1093/mnras/stv597](https://doi.org/10.1093/mnras/stv597)
- de Jong, T., Boland, W., & Dalgarno, A. 1980, *A&A*, 91, 68
- de Zeeuw, P. T., Bureau, M., Emsellem, E., et al. 2002, *MNRAS*, 329, 513, doi: [10.1046/j.1365-8711.2002.05059.x](https://doi.org/10.1046/j.1365-8711.2002.05059.x)
- Dekel, A., & Birnboim, Y. 2006, *MNRAS*, 368, 2, doi: [10.1111/j.1365-2966.2006.10145.x](https://doi.org/10.1111/j.1365-2966.2006.10145.x)
- Dekel, A., & Burkert, A. 2014, *MNRAS*, 438, 1870, doi: [10.1093/mnras/stt2331](https://doi.org/10.1093/mnras/stt2331)
- Dekel, A., & Silk, J. 1986, *ApJ*, 303, 39, doi: [10.1086/164050](https://doi.org/10.1086/164050)
- Di Matteo, T., Springel, V., & Hernquist, L. 2005, *Nature*, 433, 604, doi: [10.1038/nature03335](https://doi.org/10.1038/nature03335)
- Domínguez Sánchez, H., Huertas-Company, M., Bernardi, M., Tuccillo, D., & Fischer, J. L. 2018, *MNRAS*, 476, 3661, doi: [10.1093/mnras/sty338](https://doi.org/10.1093/mnras/sty338)
- Draine, B. T., & Bertoldi, F. 1996, *ApJ*, 468, 269, doi: [10.1086/177689](https://doi.org/10.1086/177689)
- Drory, N., MacDonald, N., Bershady, M. A., et al. 2015, *AJ*, 149, 77, doi: [10.1088/0004-6256/149/2/77](https://doi.org/10.1088/0004-6256/149/2/77)
- Du, C., Li, N., & Li, C. 2019, *Research in Astronomy and Astrophysics*, 19, 171, doi: [10.1088/1674-4527/19/12/171](https://doi.org/10.1088/1674-4527/19/12/171)
- Ellison, S. L., Lin, L., Thorp, M. D., et al. 2021a, *MNRAS*, 502, L6, doi: [10.1093/mnras/slaa199](https://doi.org/10.1093/mnras/slaa199)
- . 2021b, *MNRAS*, 501, 4777, doi: [10.1093/mnras/staa3822](https://doi.org/10.1093/mnras/staa3822)
- Ellison, S. L., Thorp, M. D., Lin, L., et al. 2020, *MNRAS*, 493, L39, doi: [10.1093/mnras/slz179](https://doi.org/10.1093/mnras/slz179)
- Ellison, S. L., Pan, H.-A., Bluck, A. F. L., et al. 2024, *MNRAS*, 527, 10201, doi: [10.1093/mnras/stad3778](https://doi.org/10.1093/mnras/stad3778)
- Elmegreen, B. G. 1983, *MNRAS*, 203, 1011, doi: [10.1093/mnras/203.4.1011](https://doi.org/10.1093/mnras/203.4.1011)
- . 1989, *ApJ*, 338, 178, doi: [10.1086/167192](https://doi.org/10.1086/167192)
- . 2002, *ApJ*, 577, 206, doi: [10.1086/342177](https://doi.org/10.1086/342177)
- . 2011, *ApJ*, 737, 10, doi: [10.1088/0004-637X/737/1/10](https://doi.org/10.1088/0004-637X/737/1/10)
- Elmegreen, B. G., & Parravano, A. 1994, *ApJL*, 435, L121, doi: [10.1086/187609](https://doi.org/10.1086/187609)
- Faber, S. M., Willmer, C. N. A., Wolf, C., et al. 2007, *ApJ*, 665, 265, doi: [10.1086/519294](https://doi.org/10.1086/519294)
- Fabian, A. C. 2012, *ARA&A*, 50, 455, doi: [10.1146/annurev-astro-081811-125521](https://doi.org/10.1146/annurev-astro-081811-125521)
- Fang, J. J., Faber, S. M., Koo, D. C., & Dekel, A. 2013, *ApJ*, 776, 63, doi: [10.1088/0004-637X/776/1/63](https://doi.org/10.1088/0004-637X/776/1/63)
- Faucher-Giguère, C.-A., Quataert, E., & Hopkins, P. F. 2013, *MNRAS*, 433, 1970, doi: [10.1093/mnras/stt866](https://doi.org/10.1093/mnras/stt866)
- Federman, S. R., Glassgold, A. E., & Kwan, J. 1979, *ApJ*, 227, 466, doi: [10.1086/156753](https://doi.org/10.1086/156753)
- Franco, J., & Cox, D. P. 1986, *PASP*, 98, 1076, doi: [10.1086/131876](https://doi.org/10.1086/131876)
- Geha, M., Blanton, M. R., Yan, R., & Tinker, J. L. 2012, *ApJ*, 757, 85, doi: [10.1088/0004-637X/757/1/85](https://doi.org/10.1088/0004-637X/757/1/85)
- Glassgold, A. E., Huggins, P. J., & Langer, W. D. 1985, *ApJ*, 290, 615, doi: [10.1086/163019](https://doi.org/10.1086/163019)
- Goldreich, P., & Lynden-Bell, D. 1965, *MNRAS*, 130, 125, doi: [10.1093/mnras/130.2.125](https://doi.org/10.1093/mnras/130.2.125)
- Gomes, J. M., Papaderos, P., Kehrig, C., et al. 2016, *A&A*, 588, A68, doi: [10.1051/0004-6361/201525976](https://doi.org/10.1051/0004-6361/201525976)
- Gunn, J. E., & Gott, J. Richard, I. 1972, *ApJ*, 176, 1, doi: [10.1086/151605](https://doi.org/10.1086/151605)
- Gunn, J. E., Siegmund, W. A., Mannery, E. J., et al. 2006, *AJ*, 131, 2332, doi: [10.1086/500975](https://doi.org/10.1086/500975)
- Guo, R., Hao, C.-N., Xia, X., et al. 2020, *ApJ*, 897, 162, doi: [10.3847/1538-4357/ab9b75](https://doi.org/10.3847/1538-4357/ab9b75)
- Hao, C.-N., Shi, Y., Chen, Y., et al. 2019, *ApJL*, 883, L36, doi: [10.3847/2041-8213/ab42e5](https://doi.org/10.3847/2041-8213/ab42e5)
- Herpich, F., Stasińska, G., Mateus, A., Vale Asari, N., & Cid Fernandes, R. 2018, *MNRAS*, 481, 1774, doi: [10.1093/mnras/sty2391](https://doi.org/10.1093/mnras/sty2391)
- Hinshaw, G., Larson, D., Komatsu, E., et al. 2013, *ApJS*, 208, 19, doi: [10.1088/0067-0049/208/2/19](https://doi.org/10.1088/0067-0049/208/2/19)

- Hopkins, P. F., Cox, T. J., Younger, J. D., & Hernquist, L. 2009, *ApJ*, 691, 1168, doi: [10.1088/0004-637X/691/2/1168](https://doi.org/10.1088/0004-637X/691/2/1168)
- Hopkins, P. F., Hernquist, L., Cox, T. J., et al. 2006, *ApJS*, 163, 1, doi: [10.1086/499298](https://doi.org/10.1086/499298)
- Hopkins, P. F., Wetzel, A., Kereš, D., et al. 2018a, *MNRAS*, 477, 1578, doi: [10.1093/mnras/sty674](https://doi.org/10.1093/mnras/sty674)
- . 2018b, *MNRAS*, 480, 800, doi: [10.1093/mnras/sty1690](https://doi.org/10.1093/mnras/sty1690)
- Hunter, D. A., Elmegreen, B. G., & Baker, A. L. 1998, *ApJ*, 493, 595, doi: [10.1086/305158](https://doi.org/10.1086/305158)
- Jog, C. J., & Solomon, P. M. 1984, *ApJ*, 276, 127, doi: [10.1086/161598](https://doi.org/10.1086/161598)
- Kalinova, V., Colombo, D., Sánchez, S. F., et al. 2022, *A&A*, 665, A90, doi: [10.1051/0004-6361/202243541](https://doi.org/10.1051/0004-6361/202243541)
- Kauffmann, G., Heckman, T. M., Tremonti, C., et al. 2003, *MNRAS*, 346, 1055, doi: [10.1111/j.1365-2966.2003.07154.x](https://doi.org/10.1111/j.1365-2966.2003.07154.x)
- Kennicutt, Robert C., J. 1989, *ApJ*, 344, 685, doi: [10.1086/167834](https://doi.org/10.1086/167834)
- . 1998a, *ARA&A*, 36, 189, doi: [10.1146/annurev.astro.36.1.189](https://doi.org/10.1146/annurev.astro.36.1.189)
- . 1998b, *ApJ*, 498, 541, doi: [10.1086/305588](https://doi.org/10.1086/305588)
- Kereš, D., Katz, N., Weinberg, D. H., & Davé, R. 2005, *MNRAS*, 363, 2, doi: [10.1111/j.1365-2966.2005.09451.x](https://doi.org/10.1111/j.1365-2966.2005.09451.x)
- Kewley, L. J., Dopita, M. A., Sutherland, R. S., Heisler, C. A., & Trevena, J. 2001, *ApJ*, 556, 121, doi: [10.1086/321545](https://doi.org/10.1086/321545)
- Kim, C.-G., Kim, W.-T., & Ostriker, E. C. 2011, *ApJ*, 743, 25, doi: [10.1088/0004-637X/743/1/25](https://doi.org/10.1088/0004-637X/743/1/25)
- Krumholz, M. R. 2012, *ApJ*, 759, 9, doi: [10.1088/0004-637X/759/1/9](https://doi.org/10.1088/0004-637X/759/1/9)
- Krumholz, M. R., McKee, C. F., & Tumlinson, J. 2009, *ApJ*, 693, 216, doi: [10.1088/0004-637X/693/1/216](https://doi.org/10.1088/0004-637X/693/1/216)
- Law, D. R., Cherinka, B., Yan, R., et al. 2016, *AJ*, 152, 83, doi: [10.3847/0004-6256/152/4/83](https://doi.org/10.3847/0004-6256/152/4/83)
- Law, D. R., Ji, X., Belfiore, F., et al. 2021, *ApJ*, 915, 35, doi: [10.3847/1538-4357/abfe0a](https://doi.org/10.3847/1538-4357/abfe0a)
- Lemonias, J. J., Schiminovich, D., Catinella, B., Heckman, T. M., & Moran, S. M. 2014, *ApJ*, 790, 27, doi: [10.1088/0004-637X/790/1/27](https://doi.org/10.1088/0004-637X/790/1/27)
- Leroy, A. K., Walter, F., Sandstrom, K., et al. 2013, *AJ*, 146, 19, doi: [10.1088/0004-6256/146/2/19](https://doi.org/10.1088/0004-6256/146/2/19)
- Li, C., Kauffmann, G., Fu, J., et al. 2012, *MNRAS*, 424, 1471, doi: [10.1111/j.1365-2966.2012.21337.x](https://doi.org/10.1111/j.1365-2966.2012.21337.x)
- Li, C., Wang, E., Lin, L., et al. 2015, *ApJ*, 804, 125, doi: [10.1088/0004-637X/804/2/125](https://doi.org/10.1088/0004-637X/804/2/125)
- Li, M., Li, Y., Bryan, G. L., Ostriker, E. C., & Quataert, E. 2020a, *ApJ*, 898, 23, doi: [10.3847/1538-4357/ab9c22](https://doi.org/10.3847/1538-4357/ab9c22)
- Li, N., & Li, C. 2023, *Chinese Physics B*, 32, 039801, doi: [10.1088/1674-1056/acb0ba](https://doi.org/10.1088/1674-1056/acb0ba)
- Li, N., Li, C., Mo, H., et al. 2020b, *ApJ*, 896, 38, doi: [10.3847/1538-4357/ab92a1](https://doi.org/10.3847/1538-4357/ab92a1)
- . 2021, *ApJ*, 917, 72, doi: [10.3847/1538-4357/ac0973](https://doi.org/10.3847/1538-4357/ac0973)
- Li, X., Li, C., Mo, H. J., et al. 2023, arXiv e-prints, arXiv:2312.03601, doi: [10.48550/arXiv.2312.03601](https://doi.org/10.48550/arXiv.2312.03601)
- Lin, L., Pan, H.-A., Ellison, S. L., et al. 2019a, *ApJL*, 884, L33, doi: [10.3847/2041-8213/ab4815](https://doi.org/10.3847/2041-8213/ab4815)
- Lin, L., Hsieh, B.-C., Pan, H.-A., et al. 2019b, *ApJ*, 872, 50, doi: [10.3847/1538-4357/aafa84](https://doi.org/10.3847/1538-4357/aafa84)
- Lin, L., Ellison, S. L., Pan, H.-A., et al. 2022, *ApJ*, 926, 175, doi: [10.3847/1538-4357/ac4ccc](https://doi.org/10.3847/1538-4357/ac4ccc)
- Lutz, K. A., Kilborn, V. A., Koribalski, B. S., et al. 2018, *MNRAS*, 476, 3744, doi: [10.1093/mnras/sty387](https://doi.org/10.1093/mnras/sty387)
- Ma, C.-P., Greene, J. E., McConnell, N., et al. 2014, *ApJ*, 795, 158, doi: [10.1088/0004-637X/795/2/158](https://doi.org/10.1088/0004-637X/795/2/158)
- Maillard, V., Bron, E., & Le Petit, F. 2021, *A&A*, 656, A65, doi: [10.1051/0004-6361/202140865](https://doi.org/10.1051/0004-6361/202140865)
- Marino, R. A., Rosales-Ortega, F. F., Sánchez, S. F., et al. 2013, *A&A*, 559, A114, doi: [10.1051/0004-6361/201321956](https://doi.org/10.1051/0004-6361/201321956)
- Martig, M., Bournaud, F., Teyssier, R., & Dekel, A. 2009, *ApJ*, 707, 250, doi: [10.1088/0004-637X/707/1/250](https://doi.org/10.1088/0004-637X/707/1/250)
- Masters, K., & Stark, D. V. 2019, in *American Astronomical Society Meeting Abstracts*, Vol. 233, American Astronomical Society Meeting Abstracts #233, 363.23
- Masters, K. L., Mosleh, M., Romer, A. K., et al. 2010, *MNRAS*, 405, 783, doi: [10.1111/j.1365-2966.2010.16503.x](https://doi.org/10.1111/j.1365-2966.2010.16503.x)
- McCray, R., & Snow, T. P., J. 1979, *ARA&A*, 17, 213, doi: [10.1146/annurev.aa.17.090179.001241](https://doi.org/10.1146/annurev.aa.17.090179.001241)
- McKee, C. F., & Ostriker, E. C. 2007, *ARA&A*, 45, 565, doi: [10.1146/annurev.astro.45.051806.110602](https://doi.org/10.1146/annurev.astro.45.051806.110602)
- McKee, C. F., & Ostriker, J. P. 1977, *ApJ*, 218, 148, doi: [10.1086/155667](https://doi.org/10.1086/155667)
- Meert, A., Vikram, V., & Bernardi, M. 2016, *MNRAS*, 455, 2440, doi: [10.1093/mnras/stv2475](https://doi.org/10.1093/mnras/stv2475)
- Merluzzi, P., Busarello, G., Dopita, M. A., et al. 2013, *MNRAS*, 429, 1747, doi: [10.1093/mnras/sts466](https://doi.org/10.1093/mnras/sts466)
- Mihos, J. C., & Hernquist, L. 1996, *ApJ*, 464, 641, doi: [10.1086/177353](https://doi.org/10.1086/177353)
- Moore, B., Katz, N., Lake, G., Dressler, A., & Oemler, A. 1996, *Nature*, 379, 613, doi: [10.1038/379613a0](https://doi.org/10.1038/379613a0)
- Morisset, C., Delgado-Inglada, G., Sánchez, S. F., et al. 2016, *A&A*, 594, A37, doi: [10.1051/0004-6361/201628559](https://doi.org/10.1051/0004-6361/201628559)
- Morselli, L., Rodighiero, G., Enia, A., et al. 2020, *MNRAS*, 496, 4606, doi: [10.1093/mnras/staa1811](https://doi.org/10.1093/mnras/staa1811)
- Muratov, A. L., Kereš, D., Faucher-Giguère, C.-A., et al. 2015, *MNRAS*, 454, 2691, doi: [10.1093/mnras/stv2126](https://doi.org/10.1093/mnras/stv2126)
- Obreschkow, D., Glazebrook, K., Kilborn, V., & Lutz, K. 2016, *ApJL*, 824, L26, doi: [10.3847/2041-8205/824/2/L26](https://doi.org/10.3847/2041-8205/824/2/L26)

- Ocvirk, P., Pichon, C., & Teyssier, R. 2008, *MNRAS*, 390, 1326, doi: [10.1111/j.1365-2966.2008.13763.x](https://doi.org/10.1111/j.1365-2966.2008.13763.x)
- Ostriker, E. C., & Kim, C.-G. 2022, *ApJ*, 936, 137, doi: [10.3847/1538-4357/ac7de2](https://doi.org/10.3847/1538-4357/ac7de2)
- Ostriker, E. C., McKee, C. F., & Leroy, A. K. 2010, *ApJ*, 721, 975, doi: [10.1088/0004-637X/721/2/975](https://doi.org/10.1088/0004-637X/721/2/975)
- Ostriker, E. C., & Shetty, R. 2011, *ApJ*, 731, 41, doi: [10.1088/0004-637X/731/1/41](https://doi.org/10.1088/0004-637X/731/1/41)
- Pan, H.-A., Lin, L., Hsieh, B.-C., et al. 2018, *ApJ*, 868, 132, doi: [10.3847/1538-4357/aaeb92](https://doi.org/10.3847/1538-4357/aaeb92)
- Papaderos, P., Gomes, J. M., Vílchez, J. M., et al. 2013, *A&A*, 555, L1, doi: [10.1051/0004-6361/201321681](https://doi.org/10.1051/0004-6361/201321681)
- Parkash, V., Brown, M. J. I., Jarrett, T. H., Fraser-McKelvie, A., & Cluver, M. E. 2019, *MNRAS*, 485, 3169, doi: [10.1093/mnras/stz593](https://doi.org/10.1093/mnras/stz593)
- Pedregosa, F., Varoquaux, G., Gramfort, A., et al. 2011, *Journal of Machine Learning Research*, 12, 2825
- Peng, Y., Maiolino, R., & Cochrane, R. 2015, *Nature*, 521, 192, doi: [10.1038/nature14439](https://doi.org/10.1038/nature14439)
- Peng, Y.-j., & Renzini, A. 2020, *MNRAS*, 491, L51, doi: [10.1093/mnrasl/slz163](https://doi.org/10.1093/mnrasl/slz163)
- Pessa, I., Schinnerer, E., Belfiore, F., et al. 2021, *A&A*, 650, A134, doi: [10.1051/0004-6361/202140733](https://doi.org/10.1051/0004-6361/202140733)
- Pessa, I., Schinnerer, E., Leroy, A. K., et al. 2022, *A&A*, 663, A61, doi: [10.1051/0004-6361/202142832](https://doi.org/10.1051/0004-6361/202142832)
- Pettini, M., & Pagel, B. E. J. 2004, *MNRAS*, 348, L59, doi: [10.1111/j.1365-2966.2004.07591.x](https://doi.org/10.1111/j.1365-2966.2004.07591.x)
- Poggianti, B. M., Moretti, A., Gullieuszik, M., et al. 2017, *ApJ*, 844, 48, doi: [10.3847/1538-4357/aa78ed](https://doi.org/10.3847/1538-4357/aa78ed)
- Rafikov, R. R. 2001, *MNRAS*, 323, 445, doi: [10.1046/j.1365-8711.2001.04201.x](https://doi.org/10.1046/j.1365-8711.2001.04201.x)
- Raskutti, S., Ostriker, E. C., & Skinner, M. A. 2016, *ApJ*, 829, 130, doi: [10.3847/0004-637X/829/2/130](https://doi.org/10.3847/0004-637X/829/2/130)
- Rees, M. J., & Ostriker, J. P. 1977, *MNRAS*, 179, 541, doi: [10.1093/mnras/179.4.541](https://doi.org/10.1093/mnras/179.4.541)
- Rembold, S. B., Shimoia, J. S., Storchi-Bergmann, T., et al. 2017, *MNRAS*, 472, 4382, doi: [10.1093/mnras/stx2264](https://doi.org/10.1093/mnras/stx2264)
- Romeo, A. B. 1992, *MNRAS*, 256, 307, doi: [10.1093/mnras/256.2.307](https://doi.org/10.1093/mnras/256.2.307)
- Rosales-Ortega, F. F., Sánchez, S. F., Iglesias-Páramo, J., et al. 2012, *ApJL*, 756, L31, doi: [10.1088/2041-8205/756/2/L31](https://doi.org/10.1088/2041-8205/756/2/L31)
- Safronov, V. S. 1960, *Annales d'Astrophysique*, 23, 979
- Saintonge, A., & Catinella, B. 2022, *ARA&A*, 60, 319, doi: [10.1146/annurev-astro-021022-043545](https://doi.org/10.1146/annurev-astro-021022-043545)
- Salim, S., Boquien, M., & Lee, J. C. 2018, *ApJ*, 859, 11, doi: [10.3847/1538-4357/aabf3c](https://doi.org/10.3847/1538-4357/aabf3c)
- Salim, S., Lee, J. C., Janowiecki, S., et al. 2016, *ApJS*, 227, 2, doi: [10.3847/0067-0049/227/1/2](https://doi.org/10.3847/0067-0049/227/1/2)
- Sánchez, S. F. 2020, *ARA&A*, 58, 99, doi: [10.1146/annurev-astro-012120-013326](https://doi.org/10.1146/annurev-astro-012120-013326)
- Sánchez, S. F., Galbany, L., Walcher, C. J., García-Benito, R., & Barrera-Ballesteros, J. K. 2023a, *MNRAS*, 526, 5555, doi: [10.1093/mnras/stad3119](https://doi.org/10.1093/mnras/stad3119)
- Sánchez, S. F., Gómez Medina, D. C., Barrera-Ballesteros, J. K., et al. 2023b, in *Resolving the Rise and Fall of Star Formation in Galaxies*, ed. T. Wong & W.-T. Kim, Vol. 373, 3–10, doi: [10.1017/S1743921322003830](https://doi.org/10.1017/S1743921322003830)
- Sánchez, S. F., Lugo-Aranda, A. Z., Sánchez Almeida, J., et al. 2024, *A&A*, 682, A71, doi: [10.1051/0004-6361/202347711](https://doi.org/10.1051/0004-6361/202347711)
- Sánchez, S. F., Walcher, C. J., Lopez-Cobá, C., et al. 2021a, *RMxAA*, 57, 3, doi: [10.22201/ia.01851101p.2021.57.01.01](https://doi.org/10.22201/ia.01851101p.2021.57.01.01)
- Sánchez, S. F., Kennicutt, R. C., Gil de Paz, A., et al. 2012, *A&A*, 538, A8, doi: [10.1051/0004-6361/201117353](https://doi.org/10.1051/0004-6361/201117353)
- Sánchez, S. F., Rosales-Ortega, F. F., Jungwiert, B., et al. 2013, *A&A*, 554, A58, doi: [10.1051/0004-6361/201220669](https://doi.org/10.1051/0004-6361/201220669)
- Sánchez, S. F., Rosales-Ortega, F. F., Iglesias-Páramo, J., et al. 2014, *A&A*, 563, A49, doi: [10.1051/0004-6361/201322343](https://doi.org/10.1051/0004-6361/201322343)
- Sánchez, S. F., García-Benito, R., Zibetti, S., et al. 2016, *A&A*, 594, A36, doi: [10.1051/0004-6361/201628661](https://doi.org/10.1051/0004-6361/201628661)
- Sánchez, S. F., Avila-Reese, V., Hernandez-Toledo, H., et al. 2018, *RMxAA*, 54, 217, doi: [10.48550/arXiv.1709.05438](https://doi.org/10.48550/arXiv.1709.05438)
- Sánchez, S. F., Barrera-Ballesteros, J. K., Colombo, D., et al. 2021b, *MNRAS*, 503, 1615, doi: [10.1093/mnras/stab442](https://doi.org/10.1093/mnras/stab442)
- Sánchez, S. F., Barrera-Ballesteros, J. K., Lacerda, E., et al. 2022, *ApJS*, 262, 36, doi: [10.3847/1538-4365/ac7b8f](https://doi.org/10.3847/1538-4365/ac7b8f)
- Sarzi, M., Shields, J. C., Schawinski, K., et al. 2010, *MNRAS*, 402, 2187, doi: [10.1111/j.1365-2966.2009.16039.x](https://doi.org/10.1111/j.1365-2966.2009.16039.x)
- Sazonova, E., Alatalo, K., Rowlands, K., et al. 2021, *ApJ*, 919, 134, doi: [10.3847/1538-4357/ac0f7f](https://doi.org/10.3847/1538-4357/ac0f7f)
- Schaye, J. 2004, *ApJ*, 609, 667, doi: [10.1086/421232](https://doi.org/10.1086/421232)
- Schmidt, M. 1959, *ApJ*, 129, 243, doi: [10.1086/146614](https://doi.org/10.1086/146614)
- . 1963, *ApJ*, 137, 758, doi: [10.1086/147553](https://doi.org/10.1086/147553)
- Schruba, A., Leroy, A. K., Walter, F., et al. 2011, *AJ*, 142, 37, doi: [10.1088/0004-6256/142/2/37](https://doi.org/10.1088/0004-6256/142/2/37)
- Serra, P., Oosterloo, T., Morganti, R., et al. 2012, *MNRAS*, 422, 1835, doi: [10.1111/j.1365-2966.2012.20219.x](https://doi.org/10.1111/j.1365-2966.2012.20219.x)
- Sharma, A., Masters, K. L., Stark, D. V., et al. 2023, *MNRAS*, 526, 1573, doi: [10.1093/mnras/stad2695](https://doi.org/10.1093/mnras/stad2695)
- Shi, Y., Helou, G., Yan, L., et al. 2011, *ApJ*, 733, 87, doi: [10.1088/0004-637X/733/2/87](https://doi.org/10.1088/0004-637X/733/2/87)
- Shi, Y., Yan, L., Armus, L., et al. 2018, *ApJ*, 853, 149, doi: [10.3847/1538-4357/aaa3e6](https://doi.org/10.3847/1538-4357/aaa3e6)
- Silk, J. 1977, *ApJ*, 211, 638, doi: [10.1086/154972](https://doi.org/10.1086/154972)

- Singh, R., van de Ven, G., Jahnke, K., et al. 2013, *A&A*, 558, A43, doi: [10.1051/0004-6361/201322062](https://doi.org/10.1051/0004-6361/201322062)
- Smee, S. A., Gunn, J. E., Uomoto, A., et al. 2013, *AJ*, 146, 32, doi: [10.1088/0004-6256/146/2/32](https://doi.org/10.1088/0004-6256/146/2/32)
- Springel, V., Di Matteo, T., & Hernquist, L. 2005, *ApJL*, 620, L79, doi: [10.1086/428772](https://doi.org/10.1086/428772)
- Stark, D. V., Bundy, K. A., Orr, M. E., et al. 2018, *MNRAS*, 474, 2323, doi: [10.1093/mnras/stx2903](https://doi.org/10.1093/mnras/stx2903)
- Stasińska, G., Vale Asari, N., Cid Fernandes, R., et al. 2008, *MNRAS*, 391, L29, doi: [10.1111/j.1745-3933.2008.00550.x](https://doi.org/10.1111/j.1745-3933.2008.00550.x)
- Stecher, T. P., & Williams, D. A. 1967, *ApJL*, 149, L29, doi: [10.1086/180047](https://doi.org/10.1086/180047)
- Sternberg, A., Gurman, A., & Bialy, S. 2021, *ApJ*, 920, 83, doi: [10.3847/1538-4357/ac167b](https://doi.org/10.3847/1538-4357/ac167b)
- Sternberg, A., Le Petit, F., Roueff, E., & Le Bourlot, J. 2014, *ApJ*, 790, 10, doi: [10.1088/0004-637X/790/1/10](https://doi.org/10.1088/0004-637X/790/1/10)
- Su, K.-Y., Hopkins, P. F., Hayward, C. C., et al. 2019, *MNRAS*, 487, 4393, doi: [10.1093/mnras/stz1494](https://doi.org/10.1093/mnras/stz1494)
- Tan, J. C. 2000, *ApJ*, 536, 173, doi: [10.1086/308905](https://doi.org/10.1086/308905)
- Thompson, T. A., Quataert, E., & Murray, N. 2005, *ApJ*, 630, 167, doi: [10.1086/431923](https://doi.org/10.1086/431923)
- Toomre, A. 1964, *ApJ*, 139, 1217, doi: [10.1086/147861](https://doi.org/10.1086/147861)
- Toomre, A., & Toomre, J. 1972, *ApJ*, 178, 623, doi: [10.1086/151823](https://doi.org/10.1086/151823)
- Tremonti, C. A., Heckman, T. M., Kauffmann, G., et al. 2004, *ApJ*, 613, 898, doi: [10.1086/423264](https://doi.org/10.1086/423264)
- Vázquez-Semadeni, E. 2010, in *Astronomical Society of the Pacific Conference Series*, Vol. 438, *The Dynamic Interstellar Medium: A Celebration of the Canadian Galactic Plane Survey*, ed. R. Kothes, T. L. Landecker, & A. G. Willis, 83, doi: [10.48550/arXiv.1009.3962](https://doi.org/10.48550/arXiv.1009.3962)
- Vogt, N. P., Haynes, M. P., Giovanelli, R., & Herter, T. 2004, *AJ*, 127, 3300, doi: [10.1086/420702](https://doi.org/10.1086/420702)
- Wake, D. A., Bundy, K., Diamond-Stanic, A. M., et al. 2017, *AJ*, 154, 86, doi: [10.3847/1538-3881/aa7ecc](https://doi.org/10.3847/1538-3881/aa7ecc)
- Walcher, C. J., Wisotzki, L., Bekeraité, S., et al. 2014, *A&A*, 569, A1, doi: [10.1051/0004-6361/201424198](https://doi.org/10.1051/0004-6361/201424198)
- Wang, B., & Silk, J. 1994, *ApJ*, 427, 759, doi: [10.1086/174182](https://doi.org/10.1086/174182)
- Wang, E., Li, C., Xiao, T., et al. 2018, *ApJ*, 856, 137, doi: [10.3847/1538-4357/aab263](https://doi.org/10.3847/1538-4357/aab263)
- Wang, J., Catinella, B., Saintonge, A., et al. 2020, *ApJ*, 890, 63, doi: [10.3847/1538-4357/ab68dd](https://doi.org/10.3847/1538-4357/ab68dd)
- Wang, J., Koribalski, B. S., Serra, P., et al. 2016, *MNRAS*, 460, 2143, doi: [10.1093/mnras/stw1099](https://doi.org/10.1093/mnras/stw1099)
- Wang, L., Zheng, Z., Hao, C.-N., et al. 2022, *MNRAS*, 516, 2337, doi: [10.1093/mnras/stac2292](https://doi.org/10.1093/mnras/stac2292)
- Weinmann, S. M., Kauffmann, G., van den Bosch, F. C., et al. 2009, *MNRAS*, 394, 1213, doi: [10.1111/j.1365-2966.2009.14412.x](https://doi.org/10.1111/j.1365-2966.2009.14412.x)
- Westfall, K. B., Cappellari, M., Bershady, M. A., et al. 2019, *AJ*, 158, 231, doi: [10.3847/1538-3881/ab44a2](https://doi.org/10.3847/1538-3881/ab44a2)
- Whitworth, A. 1979, *MNRAS*, 186, 59, doi: [10.1093/mnras/186.1.59](https://doi.org/10.1093/mnras/186.1.59)
- Wolf, C., Gray, M. E., & Meisenheimer, K. 2005, *A&A*, 443, 435, doi: [10.1051/0004-6361:20053585](https://doi.org/10.1051/0004-6361:20053585)
- Wolf, C., Aragón-Salamanca, A., Balogh, M., et al. 2009, *MNRAS*, 393, 1302, doi: [10.1111/j.1365-2966.2008.14204.x](https://doi.org/10.1111/j.1365-2966.2008.14204.x)
- Wong, T., & Blitz, L. 2002, *ApJ*, 569, 157, doi: [10.1086/339287](https://doi.org/10.1086/339287)
- Yan, R., & Blanton, M. R. 2012, *ApJ*, 747, 61, doi: [10.1088/0004-637X/747/1/61](https://doi.org/10.1088/0004-637X/747/1/61)
- Yan, R., Bundy, K., Law, D. R., et al. 2016a, *AJ*, 152, 197, doi: [10.3847/0004-6256/152/6/197](https://doi.org/10.3847/0004-6256/152/6/197)
- Yan, R., Tremonti, C., Bershady, M. A., et al. 2016b, *AJ*, 151, 8, doi: [10.3847/0004-6256/151/1/8](https://doi.org/10.3847/0004-6256/151/1/8)
- Yao, Y., Chen, G., Liu, H., et al. 2022, *A&A*, 661, A112, doi: [10.1051/0004-6361/202243104](https://doi.org/10.1051/0004-6361/202243104)
- York, D. G., Adelman, J., Anderson, John E., J., et al. 2000, *AJ*, 120, 1579, doi: [10.1086/301513](https://doi.org/10.1086/301513)
- Zhang, C.-P., Li, G.-X., Pillai, T., et al. 2020, *A&A*, 638, A105, doi: [10.1051/0004-6361/201936118](https://doi.org/10.1051/0004-6361/201936118)
- Zhang, K., Yan, R., Bundy, K., et al. 2017, *MNRAS*, 466, 3217, doi: [10.1093/mnras/stw3308](https://doi.org/10.1093/mnras/stw3308)
- Zhang, W., Li, C., Kauffmann, G., & Xiao, T. 2013, *MNRAS*, 429, 2191, doi: [10.1093/mnras/sts490](https://doi.org/10.1093/mnras/sts490)
- Zhou, S., Li, C., Hao, C.-N., et al. 2021, *ApJ*, 916, 38, doi: [10.3847/1538-4357/ac06cc](https://doi.org/10.3847/1538-4357/ac06cc)
- Zolotov, A., Dekel, A., Mandelker, N., et al. 2015, *MNRAS*, 450, 2327, doi: [10.1093/mnras/stv740](https://doi.org/10.1093/mnras/stv740)